Geometric and spatial heterogeneity in natural fracture systems formed during 3D strain

Guo, Jiulin

Geometric and spatial heterogeneity in natural fracture systems formed during 3D strain

Jiulin Guo

Department of Earth Sciences

University of Durham

A thesis submitted for the degree of

Doctor of Philosophy

April 16, 2009

Declaration

The material contained within this thesis has not previously been submitted for a degree at the University of Durham or any other universities. The research reported within this thesis has been conducted by the author unless indicated otherwise.

To mum, Ailan

Acknowledgements

The research present in this book is funded by the ORSAS Scholarship and Sir. Kingsley Studentship. I would like to thank all those who have helped in many ways in the preparation of the thesis.

In particular, I would like to express my gratitude to my supervisors Bob Holdsworth and Ken McCaffrey for their insightful advice, guidance, patience, encouragement, and experience sharing throughout the research; to Bones (Richard Jones) for his critical suggestions and valuable hints on the orientation data analysis and Matlab® code. I must thank Nigel Woodcock and Jonathan Imber for their insightful reviews.

Thanks to Steve Smith for his useful suggestions and general discussions on the project; to Peter Craig and Camila Caiado for the discussions on spherical data analysis, geostatistics and bootstrapping methods; to Robert Wilson for the field trip guidance and discussion on the fracture orientation pattern.

Thanks to Nicola De Paola for the suggestions on the Cullercoats case study and discussions on the problem of spatial variations and strain partitioning, and also thanks to Dave Healy for the guidance to Laide fieldwork and help for the understanding of faulting during 3D strain. I am deeply thankful to Xiaoying Zhuang for the assistance of collecting field data in Cullercoats and discussions on fracture patterns and fractured pebbles.

Special thanks to Dave Sales who has made very good thin sections of the rock samples from Appleby and Laide, Victoria Martin and Pim van't Hof for introducing the LaTex.

I must thank Professor Yaoling Niu for sharing the stories of his early career. His encouragement has been priceless.

My heartfelt gratitude goes to the administrative staff Janis Oakes, Karen Atkinson, and technician Gary Wilkinson, whose patience and efficient work has helped me be able to concentrate on the research.

Finally, I would like to show my respect to my buddy — Fabio Domingos. It was a relaxed experience to talk with him about a wide range of issues and share his Brazilian philosophy.

Abstract

The geometric and spatial heterogeneity in fracture systems of natural fault zones reflect complex strain patterns and exert substantial influences on host rock properties. It has been recognized that general 3D strains will produce diffuse fracture orientation patterns and characteristic kinematics, which are proposed to vary towards the fault core. The bootstrapping methods and spatial correlation analysis [(semi-) variograms] were adopted to investigate the geometric and spatial heterogeneity in fracture orientations collected systematically with reference to their spatial locations from three distinct fault zones. This relatively rigorous approach revealed that fracture orientation patterns display systematic spatial variations and high spatial correlations traversing fault zones. Factors related to the presence of pre-existing structures and lithologies can modify strains, creating complex fracture patterns and kinematics at different scales and spatial locations. The results suggest that spatially heterogenous fracture networks in subsurface can be highly connected as channels or barriers and will, in anyways, affect the fluid flow path in aquifers.

Contents

List of Figures

List of Tables

Chapter 1

Introduction

The geometry and spatial attributes of fracture networks in fault zones provide valuable clues to understanding the evolution and growth of fault systems (e.g. Aydin, 1978; Reches, 1978; Aydin and Reches, 1982; Knott, 1994; Knott et al., 1996; Schulz and Evans, 1998; Shipton and Cowie, 2001; Wilson et al., 2003; Healy et al., 2006a; Putz-Perrier and Sanderson, 2008). In recent years, various geometric properties of fracture sets have been investigated in a spatial context in some detail, such as the variations in the fault zone thickness, secondary fault displacements, density and orientations in the direction perpendicular or parallel to the main fault trend (Knott et al., 1996; Hesthammer et al., 2000; Johansen and Fossen, 2008; Putz-Perrier and Sanderson, 2008). An investigation of the scaling properties of the fault systems has been central to many of these studies; in most cases, this has been restricted to a 1- or 2-dimensional analysis, although all authors recognize that ultimately a 3-dimensional approach is desirable (Gillespie et al., 1993; Ouillon et al., 1996; Yielding et al., 1996; Bonnet et al., 2001). The present thesis focuses on the geometric properties and spatial heterogeneity of fracture orientations developed under general 3D strains, an attribute that has in recent years received rather less attention.

It is well known that fracture orientation contributes significantly to the connectivity anisotropy of a fracture network connectivity and therefore exerts an enormous impact on the migration and flow of geofluids subsurface rock reservoirs (Adams and Dart, 1998; Caine and Forster, 1999; Aydin, 2000; Tran, 2007). Moreover, together with attributes such as displacement, thickness and density, fracture orientation is one of the most critical fault zone properties that reflects the nature of the strain and host lithology (Gross, 1995; De Paola et al., 2005a; Faulkner et al., 2006; Healy et al., 2006a; Johansen and Fossen, 2008). Thanks to studies of natural examples

(e.g. Aydin 1978; Gillespie et al. 1993; Gross 1995; Knott et al. 1996), laboratory deformation experiments (e.g. Reches 1983; Tron and Brun 1991; Schopfer et al. 2006) and computer modelling (e.g. Maillot et al. 1998; Matthai et al. 1998; Caine and Forster 1999) geoscientists have begun to be able to build more realistic models of natural fracture networks. However, the spatial heterogeneity of fracture orientations in natural fault zones is still very poorly documented. This is a fundamental issue and yet has not raised much attention within the geological community. Much of the existing treatments of spatial variations in orientation data have focussed on folded terrains, especially polyphase deformation zones (e.g. Ramsay and Huber 1987). It seems therefore that many researchers simply plot fault and fracture orientation data from field localities on stereonets and make objective or subjective comparisons without further analyzing the significance of the spatial variations in the datasets (e.g. Hesthammer et al. 2000; Wilson et al. 2003; Johansen and Fossen 2008). With the widespread recognition of narrow, highly deformed fault cores surrounded by wider damage zones in rocks (e.g. Caine and Forster 1999), it is often known or supposed that fracture orientation patterns become more complex towards the centre of the main fault (e.g. Chester et al. 1993; Shipton and Cowie 2001), but many more natural examples clearly need to be studied in detail. Current models of the faulting mechanism suggest that damage zones can form due to rupture events in which microfractures and fine-scale faults propagate, interlink and accumulate to form larger faults (Shipton and Cowie, 2001; Vermilye and Scholz, 1998), fault tip propagation initiating fractures in the fault tip area (Aydin and Johnson, 1983), or flexure of the rock in the volume around a major fault to accommodate offset (c.f. Shipton and Cowie 2001). These possible mechanisms of the damage zone evolution indicate that geometric and spatial properties of damage zone structures are strongly controlled by their location around the major fault, the stress system at certain stage of the faulting, and mechanical heterogeneity of the wall rocks (c.f. Aydin 1978; Knott et al. 1996; Kim et al. 2004).

In the present thesis, the spatial heterogeneity of secondary fault systems associated with known or inferred larger faults was investigated in three different geological settings. Statistical techniques were adopted and further developed to estimate the distribution patterns and quantify the spatial heterogeneity of the orientation data. The aim of the thesis is to derive a variation model for fractures in fault zones from the analysis of the spatial heterogeneity in fracture orientations. Three inter-related problems were addressed:

1. How does the scale of observation affect the results of such an analysis?

2. What are the typical variation patterns for secondary fault orientations in fault zones?

3. How does the mechanical heterogeneity affect the fracture orientation patterns?

Chapter 1 of the thesis introduces the nature and scope of the scientific problems to be addressed in the thesis. Chapter 2 presents a documentation and analysis of the orientation patterns of deformation bands (and deformation band clusters) in homogeneous Permian aeolian sandstones adjacent to an inferred and unexposed major, dip-slip normal fault in Appleby, N England. The study presents a comparison of the bulk fracture distribution patterns with fracture set geometries seen at smaller more local scales showing that the fracture orientation patterns may vary depending on both scale of observation and spatial location relative to the inferred fault core.

The focus of Chapter 3 is the spatial heterogeneity in fracture orientations from an obliquely reactivated normal fault cutting homogeneous aeolian sandstone in Cullercoats, NE England. The well exposed fault damage zone allows the methods developed in chapter 2 to be tested and an examination of the orientation and kinematics of the fractures due to strain partitioning in this transtensional fault zone.

Chapter 4 deals with the fault and fracture orientations from a conglomerate-sandstone sequence associated with a dip-slip normal fault zone exposed in Laide, NW Scotland. The lithology is extremely heterogeneous and can be divided into relatively homogeneous conglomerates and sandstone units at meter-scales and pebbles and matrix at centimetre-scales. A systematic comparison is presented of the orientation data of faults in the conglomerate-sandstone units and of fractures in the pebbles by their spatial locations, lithology and scale.

Chapter 5 discusses the results and draws conclusions and suggestions for further study. The statistical methods applied to delineate the spatial heterogeneity are demonstrated to be robust and the results confirm that the nature of the strains (magnitude, type and orientation) in fault zones typically varies in a direction more-or-less orthogonal to the trend of the main fault zone.

1.1 Key concepts and theory

1.1.1 Brittle deformation under 3D strain

A strain can be defined as how a body changes size and shape in response to an imposed system of forces or *stress*. The orientation, type and magnitude of a homogeneous strain can be described using the *strain ellipsoid* (e.g. Flinn 1962; Ramsay 1967; Twiss and Moores 2007). The axes of the strain ellipsoid have three mutually perpendicular orientations and are referred to as the principal strains which represent the maximum, intermediate and minimum longitudinal strain axis orientations, respectively(Fig.1.1).

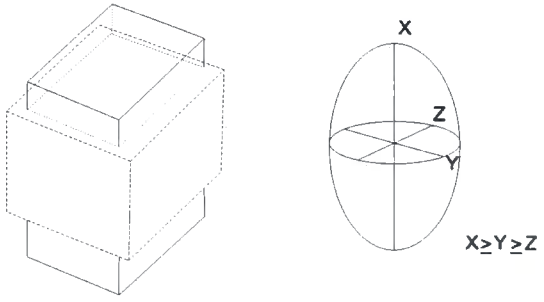

Figure 1.1: Strain ellipsoid for a homogeneously deformed body. Dashed lines shown on the left illustrate the undeformed state. Three orthogonal axes X, Y, Z indicate the direction in which the body experienced maximum, intermediate and minimum longitudinal deformation.

The classical Andersonian model of brittle faulting (Anderson, 1954), based on the Coulomb-Mohr failure criterion, explains the development of conjugate (i.e. bimodal) sets of normal, wrench or thrust faults, but in all cases the resulting bulk deformation is a two-dimensional (2-D) plane strain (e.g.Y=1; Fig. 1.2). However, since crustal deformation is ultimately the product of interactions between irregularly shaped lithospheric plates moving around a spherical Earth, then oblique shortening (*tranpression*) or oblique extension (*transtension*) should be dominant (Harland, 1971; Dewey et al., 1998). Such deformation is non-coaxial and non-plane strain, and cannot be approximated as a plane strain — pure shear or simple shear.

The most basic model for transpressional/transtensional deformation zones (Sanderson and Marchini, 1984) involves a combination of a strike-slip simple shear and a pure shear shortening/extension orthogonal to the deformation zone. There are many simplifying assumptions: the deformation is homogeneous, constant volume,

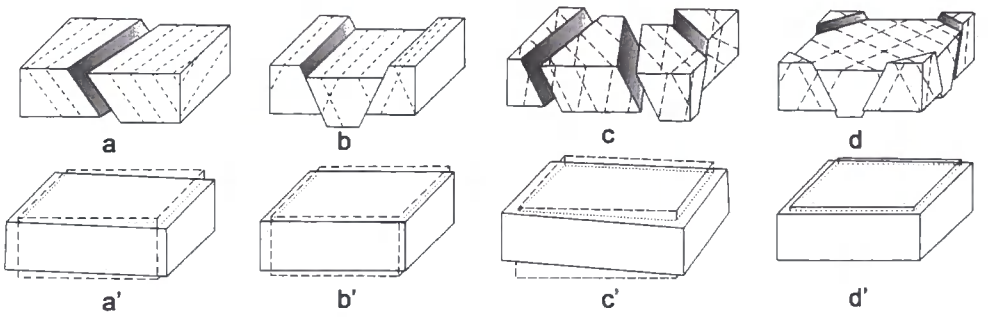

Figure 1.2: Theoretical prediction of fault patterns formed under different strain states. (a) One set of the faults that accommodates non-coaxial plane strain with constant volume shown on a'. (b) Conjugate faults accommodating coaxial plane strain shown on b'. (c) Three sets of faults initiated simultaneously to accommodate a 3D non-coaxial strain (c'). (d) Four sets of faults initiated simultaneously to accommodate a 3D co-axial strain (d'). Dashed lines shown on a-d are possible fault planes, and on a'-d' represent undeformed state (after Reches 1978).

laterally and basally confined, and occurs in a sub-vertical deformation zone between parallel zone boundaries (Fig. 1.3 a). Various boundary conditions inherent in the original model have since been changed in order to investigate the effects of strain partitioning, heterogeneous variation in strain intensity, volume change, basal and lateral stretch, non-vertical deformation boundaries and vertical displacements of one bounding block relative to the other (e.g. see Jones et al. 2004 and reference therein). Strain partitioning across a range of scales into domains of wrench- and pure shear-dominated deformation domains (Fig. 1.3b) seems to be particularly common in both transpression and transtension zones (e.g. Jones et al. 2004; De Paola et al. 2005a,b). From a brittle deformation perspective, it has been demonstrated from theoretical, laboratory and field-based studies that rock masses accommodate such 3D strains by developing multiple or *polymodal* sets of faults (Fig. 1.2 c,d; e.g. Aydin 1978; Reches 1978, 1983; De Paola et al. 2005a; Healy et al. 2006b).

In all transpression/transtension zones, the relative displacement direction across the deformation zone, infinitesimal strain (or stress) and finite strain axes are all oblique to one another. However, predictable geometric relationships exist between the orientations of the deformation zone boundaries, the axes of infinitesimal strain (stress) and the relative displacement direction across the deformation zone. We can apply an analysis using infinitesimal strain, which is equivalent to the more conventional, widely-used stress-inversion techniques (e.g. Angelier 1979, 1984; Michael

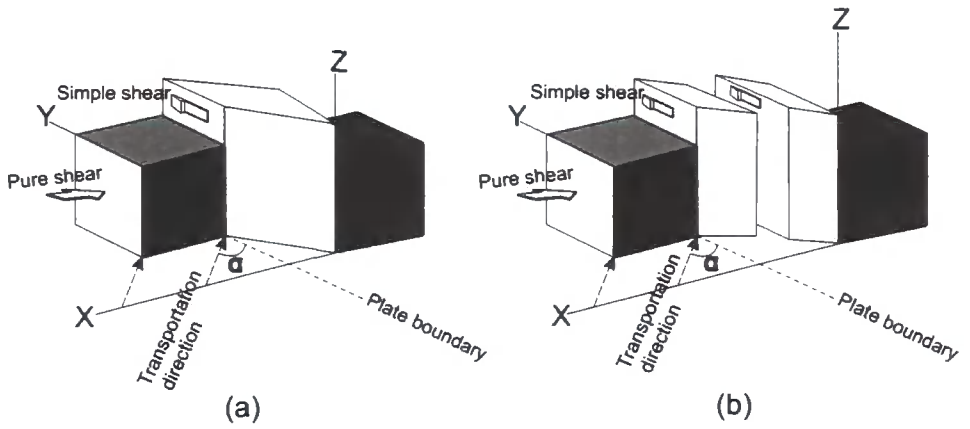

Figure 1.3: (a) Homogeneous transpression/transtension model (c.f. Sanderson and Marchini 1984) in which both components of pure shear and simple shear are uniformly distributed across the deformation zone region. (b) Heterogeneous transpression/transtension modal (c.f. Tikoff and Teyssier 1994) describes pure shear and simple shear component distribute heterogeneously, leading to the bulk strain being partitioned into distinct fault sets of different kinematics (after Tikoff and Teyssier 1994).

1984) provided the bulk finite strains are reasonably low, so that the misorientation between finite and infinitesimal strain axes is limited (De Paola et al., 2005a).

The relative importance of pure shear shortening/extension and wrench simple shear components of the 3D strain is controlled primarily by:

- the acute angle α between the far field transport direction and the deformation zone boundary (McCoss, 1986; Withjack and Jamison, 1986; Smith and Durney, 1992; Tikoff and Teyssier, 1994).
- the lithology (or, more specifically, the Poisson's Ratio; De Paola et al. 2005a).

For ideal incompressible materials, the simple shear component dominates the bulk strain to form 'wrench-dominated regime' when α is less than the critical angle 20^o (Fig. 1.4). If α is larger than 20^o, the pure shear shortening/extensional component dominates the bulk strain to form the 'pure shear (extension/shortening)-dominated regime' (McCoss, 1986). For most natural rock materials, where Poisson's ratio is <0.5, the critical angle is larger than 20^o, but the exact value depends on the Poisson's ratio of the material (De Paola et al., 2005a,b), (Fig. 1.5). Nevertheless, it will be broadly extension-dominated when α is approximately larger than 45^o (Tron and Brun, 1991; Smith and Durney, 1992). The transition from wrench- to pure

shear-dominated strains is typically marked by 'switches' in the orientations of the infinitesimal strain axes. For example, during wrench- and extension-dominated transtension, the maximum and minimum infinitesimal strain axes (X, Z axes) lie respectively in the horizontal and vertical planes, (Fig. 1.5). Since transpressional

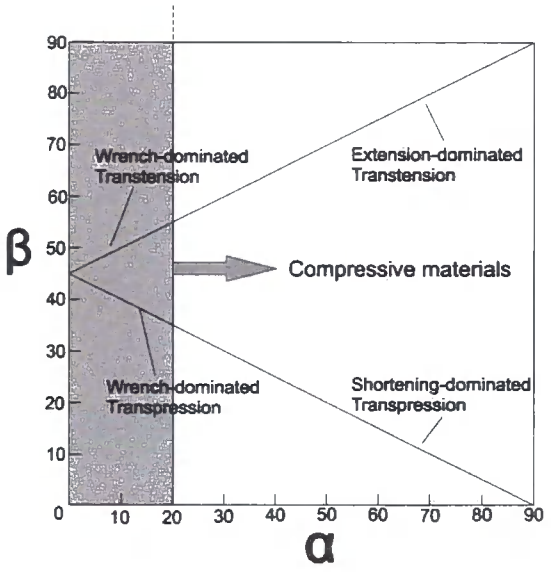

Figure 1.4: The relationship between the transportation direction α and β (the angle between the maximum horizontal extension axis and plate boundary). It shows that compressive materials will require larger α to be transformed from wrench-dominated to extensional dominated (or shortening-dominated) regime (after De Paola et al. 2005a).

and transtensional strains are non-coaxial, the axes of the finite strain ellipsoid are generally not coincident with those of the infinitesimal strain ellipsoid (Fig. 1.6). The build-up of deformation is a progressive process during which the finite strain ellipsoid gradually rotates and changes shape as the total amount of strain increases (Fig. 1.6). Numerical modelling and laboratory-based deformation experiments suggest that the initial faulting patterns will be controlled by the incremental strain and that these are likely to be preferentially reactivated in the later stages (Tikoff and Teyssier, 1994; Withjack and Jamison, 1986). These structures formed at an early stage of the deformation, however, could be incapable of accommodating all the finite strains, so that structures of different orientations and kinematics may be developed (Tikoff and Teyssier, 1994). Therefore, complex fault patterns and kinematic relationships recording polymodal faulting and reactivation of pre-existing structures and their interactions with changing strain states are likely to be widespread

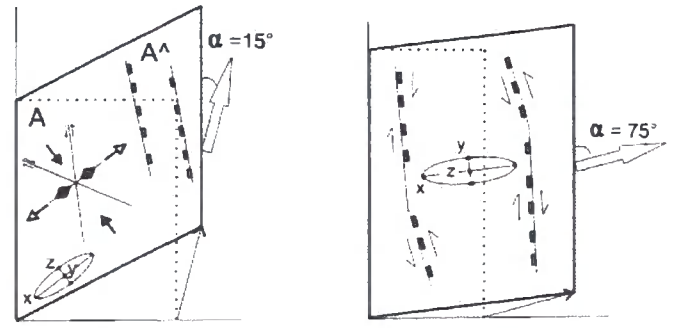

Figure 1.5: Two types of deformation regimes under transtensional deformation. (a) wrench-dominated regime in which simple shear takes a large part of the bulk strain when the transport direction α is less than 20^o for incompressive materials. The principle strains X, Z are in the horizontal plane (X≥Y≥Z). (b) Extension-dominated regime: where pure shear takes a large part of the bulk strain when the transport direction is larger than 20^o for incompressive materials. The principle strains X, Z are in the vertical plane (after De Paola et al. 2005b).

in transpressional/transtensional deformation zones.

1.1.2 Orientation analysis

1.1.2.1 Introduction and geological concepts

The measurement and analysis of geological planes and lines lies at the heart of orientation analysis in geology. Geological planes - measured using strike and dip - include features such as bedding, cleavage, faults, joints etc, whilst geological lines — measured using plunge and azimuth — include features such as fold hinges, mineral and intersection lineations, slickenlines etc. During field-based studies, such orientation data are collected at a large number of localities and are then plotted, manipulated and analysed using stereographic projection techniques (e.g. Lisle and Leyshon 2004). In general, stereonets are used in three main ways:

- In the compilation of structural data
- In the calculation of geometric properties/distributions/relationships
- In the comparison and correlation of datasets from different locations

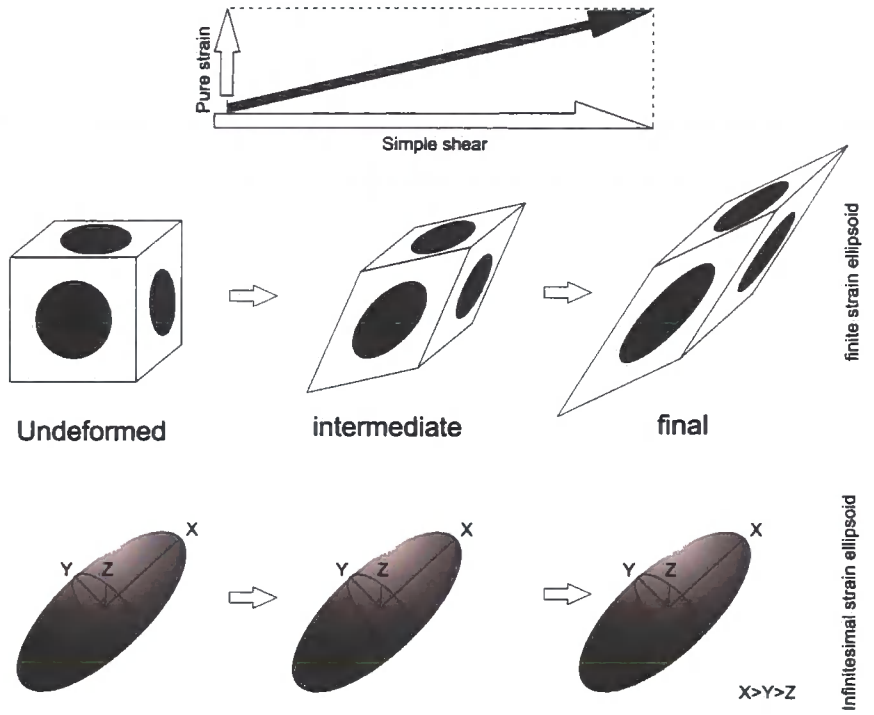

Figure 1.6: During the steady homogeneous 3D non-coaxial strain, the finite strain ellipsoid will rotate and change shape whereas the infinitesimal strain ellipsoid remains stable.

As a rule, to avoid clutter, *planar structural data are represented as poles normal to the planes.*

The use of stereographic projection techniques has been an essential component in the recognition and interpretation of *preferred orientations* in geological data. Most real datasets display preferred orientations and there are 3 main types for both linear and planar structural data (Fig. 1.7):

(a) Point maximum:

1. lines = *planar preferred orientation*
2. poles to planes = *planar preferred orientation*

(b) Girdle distribution:

1. lines = *planar preferred orientation* (all lines lie in common plane)
2. poles to planes = *linear preferred orientation*(all planes contain a common line)

3. girdles may display one or more point maxima

(c) Small-circle girdle distribution:

1. both lines and poles to planes have a *preferred orientation at a fixed angle to a line (a conical distribution)*
2. may display one or more point maxima

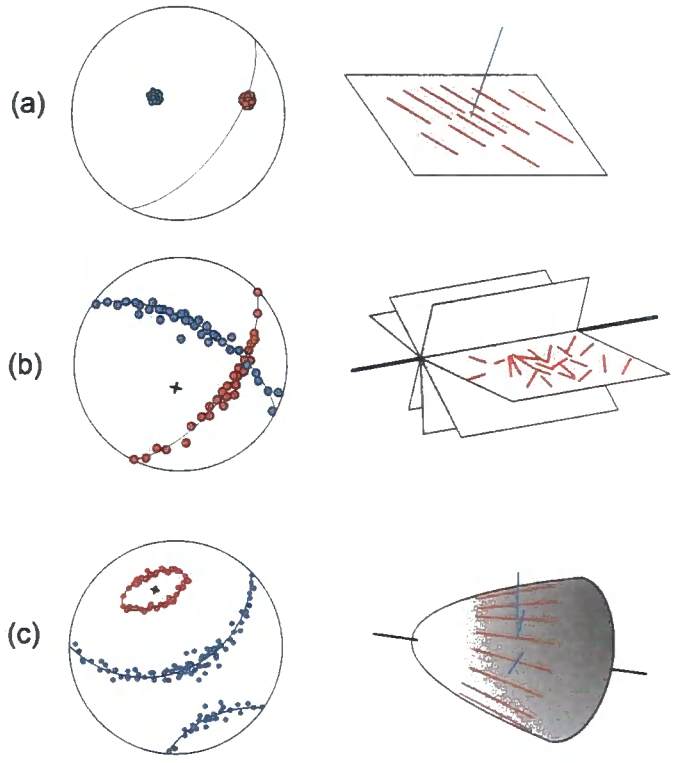

Figure 1.7: Three main types of distributions on the stereographic projection of the geological data. The linear and planar features are plotted in the lower hemisphere. The fault planes and lineations are colored in blue and red respectively. Detailed explanations please refer to the text therein.

It is generally believed that all natural orientation data show some spread (e.g. Hobbs et al. 1976). This variation in orientation data is typically attributed to factors such as inaccuracy of measurement, irregularity of structures, dispersion of data by later deformations, the development of curvilinear or curviplanar geometries etc. However, given the potential complexity of natural geological structures and the possible existence of scale-dependant spatial variations in that complexity, it is also possible that the spread of data is real and has geological significance. This is one of the concerns of the present study with reference to fracture systems in rocks.

1.1.2.2 Spherical statistics: data structure

Orientation data are typically expressed using spherical coordinates, projected onto the lower hemisphere, as dip and azimuth (θ, φ) of the pole normal to the fault plane, where $0 \leq \theta \leq 90^o$, and $0 \leq \varphi < 360^o$ (Fig. 1.8). The transformation from spherical coordinates to Cartesian coordinates is given by $(l_x, l_y, l_z) = (\cos(\theta)\sin(\varphi), \cos(\theta)\cos(\varphi), \sin(\theta))$, where $l_x^2 + l_y^2 + l_z^2 = 1$ (Fig. 1.8). Here the vector mean ori-

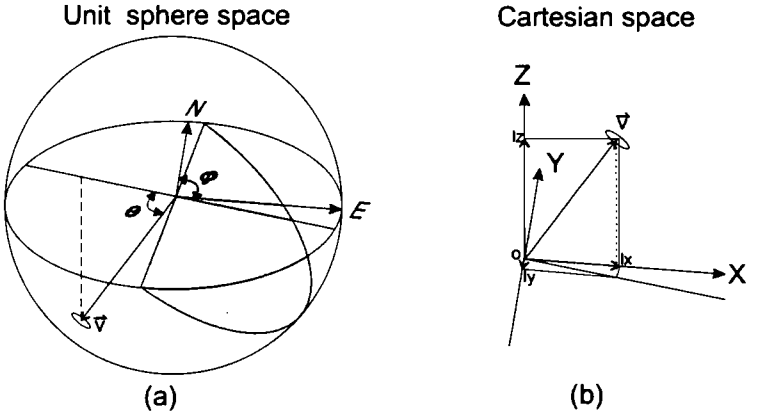

Figure 1.8: Fault orientation data expressed on a unit sphere space. Grey area schematically represents a fault plane intersecting the lower hemisphere. (θ, φ) defines the pole $\vec{V}$ normal to the fault plane. (b) The pole normal to the fault plane in the Cartesian space.

entation of the unit vectors (l_{x1}, l_{y1}, l_{z1}), (l_{x2}, l_{y2}, l_{z2}),..., (l_{xn}, l_{yn}, l_{zn}) expressed as follows:

$$(\bar{l_x}, \bar{l_y}, \bar{l_z}) = \frac{\left[\left(\frac{\sum_{i=1}^{n} l_{xi}}{n}\right), \left(\frac{\sum_{i=1}^{n} l_{yi}}{n}\right), \left(\frac{\sum_{i=1}^{n} l_{zi}}{n}\right) \right]}{\sqrt{\left(\frac{\sum_{i=1}^{n} l_{xi}}{n}\right)^2 + \left(\frac{\sum_{i=1}^{n} l_{yi}}{n}\right)^2 + \left(\frac{\sum_{i=1}^{n} l_{zi}}{n}\right)^2}} \tag{1.1}$$

1.1.2.3 Orientation tensor

The orientation data can be expressed using a 3x3 matrix referred to as the *orientation tensor*:

$$\mathbf{B} = \begin{bmatrix} \sum_{i=1}^{n} l_{xi}^2 & \sum_{i=1}^{n} l_{xi}l_{yi} & \sum_{i=1}^{n} l_{xi}l_{zi} \\ \sum_{i=1}^{n} l_{yi}l_{xi} & \sum_{i=1}^{n} l_{yi}^2 & \sum_{i=1}^{n} l_{yi}l_{zi} \\ \sum_{i=1}^{n} l_{zi}l_{xi} & \sum_{i=1}^{n} l_{yi}l_{zi} & \sum_{i=1}^{n} l_{zi}^2 \end{bmatrix} \tag{1.2}$$

This provides information concerning the arrangement of the vectors in space (Davis, 2002). For the purposes of the present study, it is necessary to calculate the *eigen-*

values and the corresponding *eigenvectors* which ultimately measure the degree of the data concentration around the principal axes of the orientation tensor ellipsoid (Fig. 1.9). We can assign the eigenvalues λ_1, λ_2, and λ_3 ($\lambda_1 \geq \lambda_2 \geq \lambda_3 \geq 0$) and corresponding eigenvectors $\vec{V}_1$, $\vec{V}_2$, and $\vec{V}_3$. In Cartesian space, the eigenvector of the maximum eigenvalue suggests that the orientation data (in the form of unit vectors) are optimally close to this principal axis and vice versa (Fig. 1.9). If we

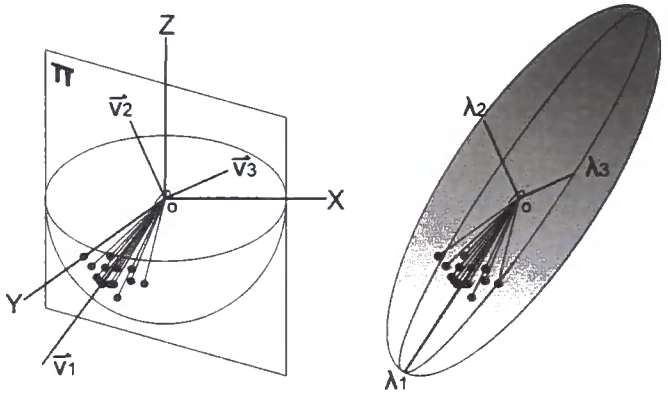

Figure 1.9: Geometric explanation of the three mutually orthogonal eigenvectors $\vec{V}_1$, $\vec{V}_2$, and $\vec{V}_3$ of the orientation tensor **B**. The eigenvector $\vec{V}_1$ of the maximum eigenvalue shows the orientation close to all the unit vectors as possible. Another two eigenvectors are in the plane Π perpendicular to $\vec{V}_1$. $\vec{V}_3$ is oriented in a direction that all the unit vectors are furthest from it as possible. Three mutually perpendicular eigenvalues λ_1, λ_2, and λ_3 are the half axial lengths of the orientation tensor ellipsoid.

project all the unit vectors onto the principal axis parallel to $\vec{V}_1$ and calculate the mean of the projected vector length, we will get the *resultant length* $\bar{R}$ which can be used as a measure of the strength of the preferred orientation. Mathematically, it is the mean of the inner product between the unit vector and a unit vector of the same orientation as $\vec{V}_1$ (c.f. Appendix A):

$$\bar{R} = \frac{\sum_{i=1}^{n} (lx_i, ly_i, lz_i) \star \frac{V_1}{\|V_1\|}}{n} \tag{1.3}$$

Hence, we have $\lambda_1 + \lambda_2 + \lambda_3 = \mathrm{n}$ and $0 \leq \bar{R} \leq 1$. Woodcock and Naylor (1983) used the *eigenvalues* and *resultant length* as a tool to classify the distribution model and degree of clustering of the orientation data. The method involves plotting the eigenvalue ratio $\ln(\lambda_1/\lambda_2)$ against $\ln(\lambda_2/\lambda_3)$, ($\mathrm{K} = \ln(\lambda_1/\lambda_2)/\ \ln(\lambda_2/\lambda_3)$) onto the

2D Cartesian coordinates. If the plotted point is close to the $\ln(\lambda_1/\lambda_2)$ axis, the orientation data have a clustered distribution; if it is close to the $\ln(\lambda_2/\lambda_3)$ axis, the data follow a girdle distribution. Additionally, the further the point is away from the origin, the stronger the distribution model is (refer to ratio $C = (\lambda_1/\lambda_3)$), (Fig. 1.10).

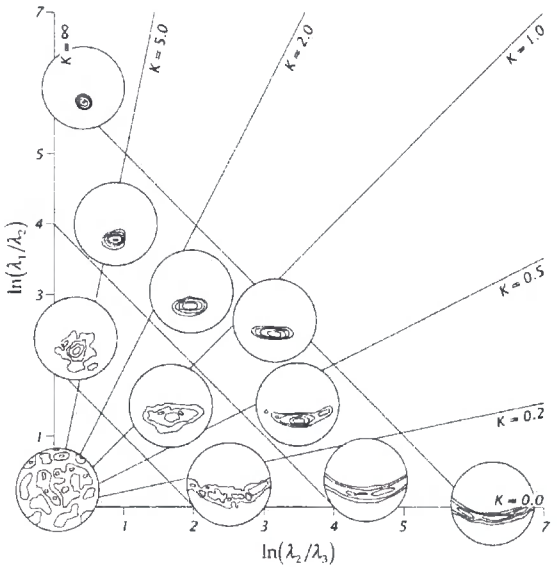

Figure 1.10: Woodcock diagram using the eigenvalue ratios — $\ln(\lambda_1/\lambda_2)$ & $\ln(\lambda_2/\lambda_3)$, ($\lambda_1 \geq \lambda_2 \geq \lambda_3$) to classify the distribution pattern for orientation data (after Woodcock and Naylor 1983).

1.1.2.4 Basic distribution models on the sphere

Uniform distribution: unit vectors in any orientations are equally likely, which spread uniformly over the surface of the sphere (Fisher et al., 1987), (Fig. 1.11). The uniform distribution is the unique distribution invariant under rotation and reflection (Mardia and Jupp, 2000). *Von Mises-Fisher distribution*: This distribution model is the analogy of the normal distribution but on the sphere surface. The majority of *unimodal distributions* fall into this category. It is rotationally symmetric about the vector mean orientation μ and has a concentration parameter κ ($\kappa > 0$), which describes the degree of clustering around μ. In particular, when $\kappa = 0$, it follows *uniform distribution* (Fig. 1.11a, a'). The clustering increases as κ increases. In the thesis $\bar{R}$ is used to estimate the concentration of a Von Mises-Fisher distributed dataset as it serves the same function as κ and is easy to calculate. Most

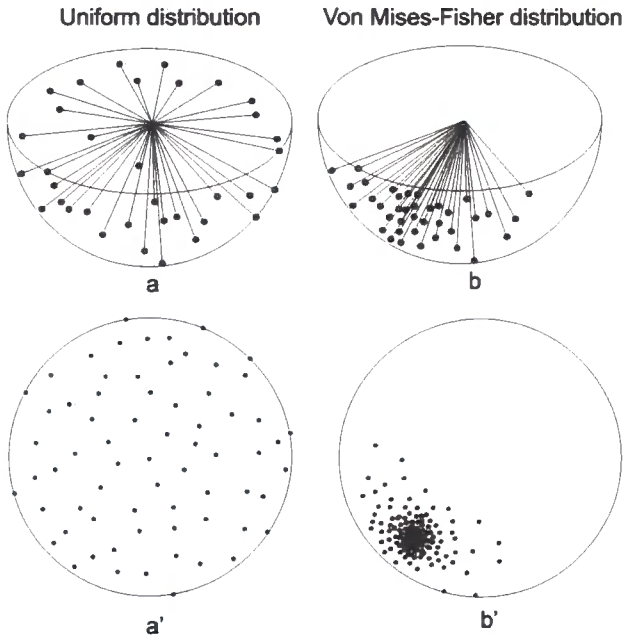

Figure 1.11: Basic distribution on the unit sphere space. (a) Uniform distribution on a lower hemisphere. The same distribution model shown on the stereoplots (a'). (b) Von Mises-Fisher distribution on the lower hemisphere. The same distribution model shown on the stereoplots (b').

unimodal distributed datasets can be approximated as following *Von Mises-Fisher distribution*, even though they were not rotationally symmetric. Bimodal distributed datasets can be simplified as the combination of two Von Mises-Fisher distributed clusters of different vector mean orientation μ and the same concentration parameter κ (Fig. 1.11b, b'). As real field data may be very noisy, relying too much on the model distributions will inevitably be misleading. To give a more reasonable estimation and statistical inference, one should not entirely depend on the available distribution models and a *nonparametric approach* should be adopted.

1.1.2.5 Multimodal distribution

Resolving multiple clusters in datasets remains a problem for many applications in that a standard definition of a cluster simply does not exist and each statistical method associated with a criterion does not always successfully describe the nature of the underlying data structure (Ye and Rabiller, 2000; Ortega et al., 2006). In terms of the fracture orientation, other factors such as fracture timing relationship and lithology in which fractures developed can effectively help to separate data for

specific purposes (Ortega et al., 2006). Many field evidence show that a diffuse elongated cluster or bimodal distribution pattern of the bulk orientation data is actually the superimposed multimodal fractures developed at finer scales (e.g. Aydin and Reches 1982; Underhill and Woodcock 1987; Shipton and Cowie 2001; Jones et al. 2005). This may also be the reason that many major faults are curved and are the amalgamation of small segments with more various orientations (c.f. Vermilye and Scholz 1998). In the thesis, the separation of clusters in fracture orientation data remains rather qualitative but constrained by the field evidence showing mutually cross-cutting submeter-scale fracture sets of multiple orientation.

1.1.2.6 Nonparametric approach

Nonparametric statistics are a family of inference methods used to investigate the data without primarily assuming a distribution model. These include resampling methods such as *bootstrap*. The 'distribution-free' feature allows one to robustly analyze data that may not follow a standard distribution model e.g. *Von Mises-Fisher distribution*. It thus can efficiently analyze scattered and noisy data. In practice both nonparametric and parametric approaches can be combined to give a most reasonable estimation of the data structure. Here, the *bootstrap method* is used to estimate the distribution of the original data. The *Bootstrap method* is a conceptually simple technique which accesses the variability of a statistic (e.g. mean, standard deviation) by resampling with replacement for a large number of times (nowadays the powerful computer can easily do $\geq$10000 times simulation) from the original dataset to generate simulated data (Efron, 1982; Mardia and Jupp, 2000), (Fig. 1.12). It has been recognized that the bootstrap is particularly useful in analyzing orientation data since the distributions of the statistics commonly used for inference on the spherical distributions are more complex than those arising in standard normal theory (Mardia and Jupp, 2000). A schematic example is illustrated in Figure 1.12, showing that the original data and their bootstrapped estimation.

1.1.3 Spatial correlation analysis

Many geological objects can be regarded as regionalized variables, which vary from locality to locality in a probabilistic manner and hence are considered to be spatially correlated over short distances (Davis, 2002), (Fig. 1.13a). The observations of the regionalized variables are called spatially distributed data and are correlated by *semivariogram* or simply, *variogram*, which describes the relationship between the separating distance h and the dissimilarity of the observations separated by h.

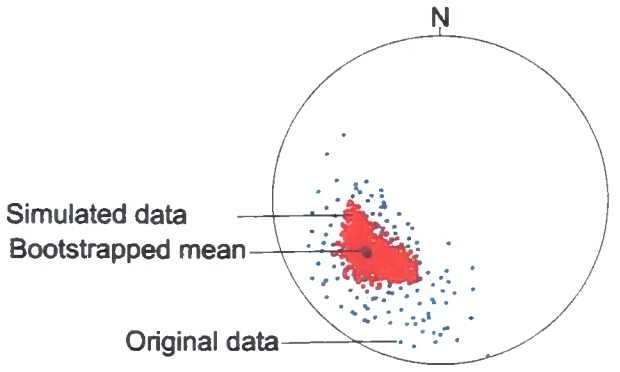

Figure 1.12: Schematic diagram showing that bootstrapped mean is used to estimate the distribution of the original data by an intensive simulation. The simulated data (red) are generated by randomly drawing samples from the original dataset (blue) with replacement and calculating the mean of the randomly sampled data. The bootstrapped mean (purple) of the original dataset is the mean of the simulated data.

This separating distance is called *lag*, and the dissimilarity of the observations at different localities is called *semivariance* or *variance* depending on how the equation is arranged mathematically. If we note x_i and x_j as the spatial location of the i^{th} and j^{th} observations, the *lag* h equals $\|x_i - x_j\|$, $\mathrm{Z}(x_i)$ and $\mathrm{Z}(x_j)$ are the observations at x_i and x_j, respectively. Then in general terms, the semivariance is:

$$\hat{\gamma(h)} = \frac{1}{2N(h)} \sum_{\|x_i - x_j\| \approx h} \|Z(x_i) - Z(y_i)\|^2 \tag{1.4}$$

The variance is simply twice the semivariance $\hat{\gamma}(h)$. For analysing orientation data, it is more geologically meaningful if equation (1.4) is modified to:

$$\hat{Y(h)} = \sqrt{\frac{1}{N(h)} \sum_{\|x_i - x_j\| \approx h} \|Z(x_i) - Z(y_i)\|^2} \tag{1.5}$$

where $\hat{Y(h)}$ is defined here as *variance* for convenience, although mathematically it should be called 'deviation', because equation (1.5) illustrates the quadratic mean of the angular difference of the orientations separated by a given *lag h*. The so called *variogram* is simply the curve generated by plotting *lag h* against *variance* $\hat{Y(h)}$. As *lag h* increases, the *variance* increases correspondingly until it reaches the *sill* — the 'plateau', where the variance will no longer increase its value as the increasing lag h, suggesting the a loss of spatial correlation (Fig. 1.13b). Hence, there is a critical

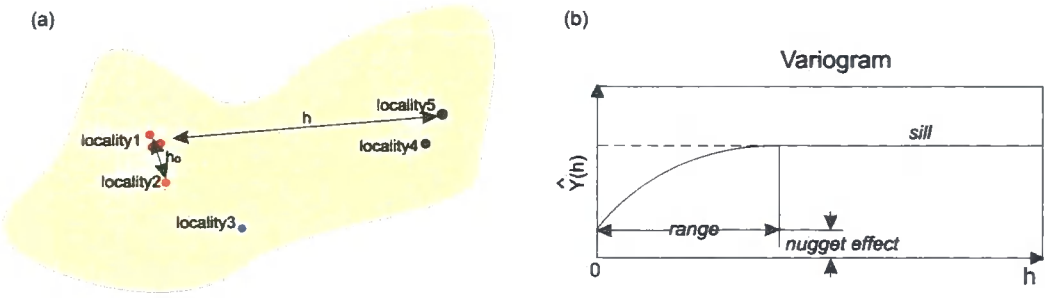

Figure 1.13: (a) Schematic diagram showing spatially distributed data: measurements separated further apart are less likely to be similar to each other. (b) Ideal variogram showing that the dissimilarity usually quantified as variance of any two spatially separated measurements is the function of the corresponding separating distance h (lag). Details of explanation please refer to the text.

value of the *lag* larger than which the variance is not correlated with h. This critical value of the lag is called the *range*. In theory, very closely spaced observations should have no difference (c.f. La Pointe 1993). In practice, this may not applicable in the real field data because of the local variability. Sampling errors or the lack of coherent sampling plan also introduce a certain degree of randomness to the sample locations (Isaaks and Srivastava, 1989). Therefore the *variance* normally has a nugget effect (non-zero value) when the *lag* h is very small (Fig. 1.13b).

The *variogram* is calculated for measurements made at scattered sampling stations and offers insights in interpreting the spatial heterogeneity in the spatially distributed datasets. The *range* reveals the maximum correlation distance in the area where the observations are made. The *sill* is a quadratic mean difference of observations that can be treated as homogeneously distributed over the *lag* h larger than the range. The *nugget effect* reflects both sampling errors and significant local change of the spatially distributed data. Multiple fracture sets, for example, will have obvious nugget effect because more than one fracture orientations can be observed at the same sampling station.

Wherever is possible, by knowing these three key parameters of the 'field-based' *variogram*, one is able to estimate the value at any unsampled locations by modelling the *variograms* (Isaaks and Srivastava, 1989). The estimation procedure is realized by using a linear regression method called 'kriging' which assumes that the observations are neither independent nor random (Davis, 2002).

1.1.4 Scaling problem

Fault length and throw are believed to have a general fractal geometry in nature, which means that any part of the object viewed at a particular scale looks similar to the object viewed at any other scales (Mandelbrot, 1982). This scale-invariant (or self-similar) characteristic of the natural fault system has been well studied by an increasing number of researchers since Mandelbrot (1982) introduced the concept of 'fractal geometry' and pointed out such non-Euclidian geometry is universal in a wide range of natural systems (e.g. Heffer and Bevan 1990; Gillespie et al. 1993; Castaing et al. 1996; Knott et al. 1996; Johnston and McCaffrey 1996; Ouillon et al. 1996; Bour and Davy 1997; Odling et al. 1999; Bonnet et al. 2001).

In 2D, 'fractal geometry' relates to fault size measured as fault 'length', 2D fault trace maps are commonly used to estimate the 'fractal dimension' (c.f. Mandelbrot 1982) using the box-counting method. The trace map is covered with regular grids and the number of boxes n intersected by the fault traces counted. Grids of successively smaller size r are used to generate a series of points on a plot showing linear relationship of $\log(1/r)$ vs. $\log(n)$ for a fractal geometry (c.f. Barton 1995), (Fig. 1.14).

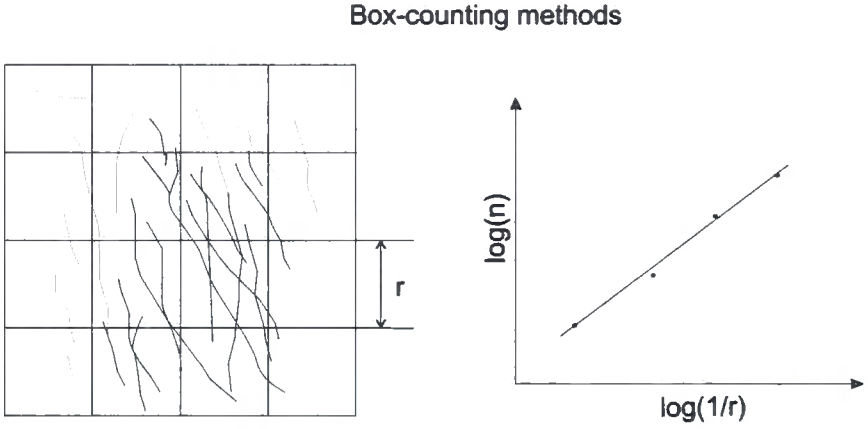

Figure 1.14: Box-counting methods used to estimate the fractal dimension of a fault trace map (after Barton 1995).

However, this definition seems not to be applicable to orientation data, which can be considered 'scale-isolated', i.e. the data has no direct relation to sample length. To investigate the relationship between fault orientation and scale of observation, the sample dimensions have to be incorporated. The original definition of scaling states:

> *Let X be a random variable, X is scaling under the transformation J(X), if the distribution of X and J(X) are identical except for scale.*
>
> — Mandelbrot(1982)

we will find that the distribution of fracture orientations from an outcrop is generally not the same as the fault orientations from the region (c.f. Jones et al. 2005). It has been recognized that at many geological settings local structures are much more heterogeneous than regional structures (e.g. Aydin 1978; Aydin and Reches 1982; Jones et al. 2005; Johansen and Fossen 2008). This suggests that the variogram range calculated for an orientation dataset may give insights in understanding the fracture orientations observed at different scales. As introduced in the last section, any observations separated by larger than the range have no spatial correlation and therefore a dataset made up of these observations are homogeneous (Fig. 1.15a, b). By contrast, if we extract observations separated by a *lag h* less than the *range*, the dataset will be heterogeneous (Fig. 1.15). The separating distance or *lag h* actually reflects the scale or degree of detail of observation that we are investigating in a spatially distributed object. Figure 1.15 schematically illustrates such a scaling property of the orientation dataset relating to its variogram. Based on the theory of variograms it is supposed that any datasets made up of observation collected at separations less than the *range* will have different distributions (Fig. 1.15c), whereas for 'sparsely sampled' datasets whose observation separation is larger than the *range* will have similar distribution, indicating a scale-invariant characteristic (Fig. 1.15d).

1.2 Methodology

In this study, the statistical methods for analysing orientation data and spatial analysis discussed above were applied to the orientation datasets collected by the author at the three sample sites. Computer simulation was carried out to achieve this statistical analysis. All the Matlab® code were written by the author, except the Schmidt stereoplot code (Middleton, 2000), (please refer to the attached CD).

1.2.1 Data acquisition

The orientation data of fractures or faults were collected systematically in 1D scanline or 2D scanplane with moving sampling stations of fixed size (Fig. 1.16. The relative spatial locations of the sampling stations were recorded for later spatial analysis. Data from the sampling stations were assigned the same spatial location

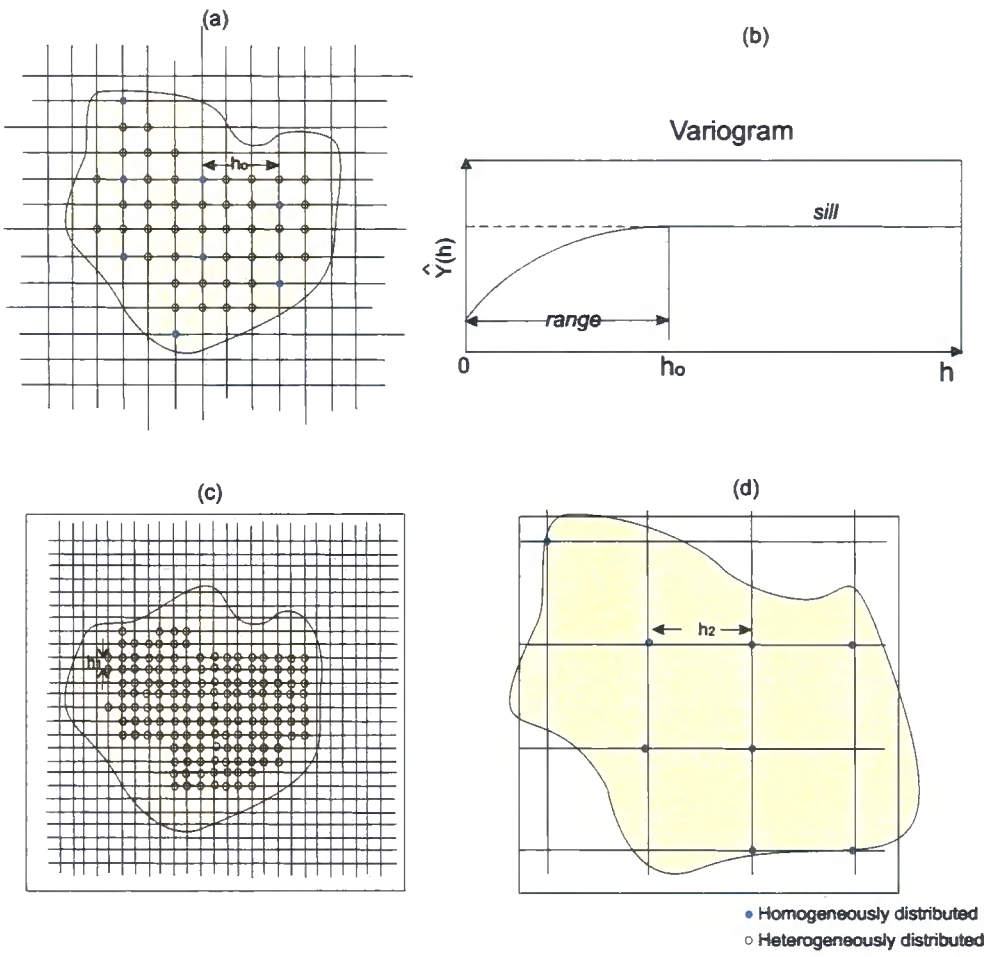

Figure 1.15: (a) Schematic diagram of spatially distributed data in an infinitely large area. (b) The corresponding variogram describes the spatial heterogeneity of the dataset shown on (a). (c) Open circles are the measurements separated by distance $h_1 < h_o$, and form heterogeneously distributed datasets. The scale or the degree of resolution is reflected by the separating distance h (lag). Datasets collected by sampling closely spaced data (h $< h_o$) will have different distribution pattern; whereas the distribution of sparsely spaced data ($h_2 > h_o$) will a similar modal that does not depend on the separating distance. (d) Blue dots are the measurements separated by distance $h_2 > h_o$, and should form homogeneously distributed datasets.

as the sampling station. The choice of 1D or 2D sampling strategy depends on the nature of the outcrop. The sandstone cliff in Appleby, N England was suitable for 1D scanline with 1 x 1 m size sampling station in which sufficient data were collected (Fig. 1.16a). At Cullercoats, 1D and 2D scanlines with 5 x 5 m size sampling stations were employed to enable collect of orientation and kinematic data as both cliff and pavement exposures are available. At Laide, 2D scanlines with 1 x 1 m sampling station were employed to collect data from faults and fractures exposed in the pavement conglomerate-sandstone sequence (Fig. 1.16b).

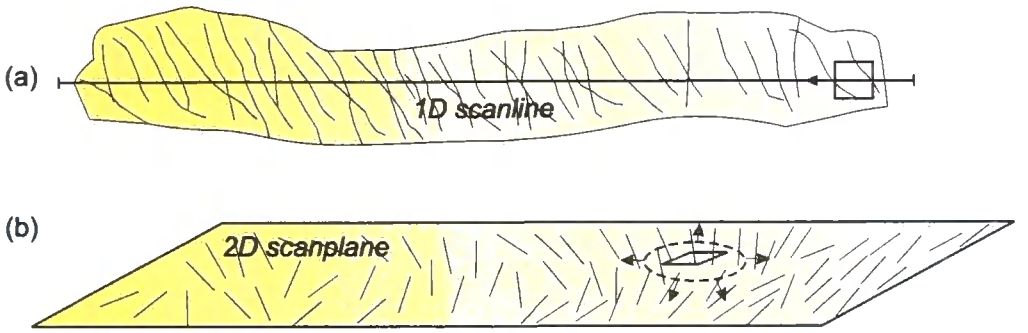

Figure 1.16: Schematic diagram of the sampling plans. (a) 1D scanline sampling is applied to sample the structures exposed in one dimension outcrop, e.g. a cliff cutting the faults with a high angle. (b) 2D scanplane sampling plan is applied to investigate structures exposed on the pavement outcrops. The sampling station can move in 2D rather than 1D, which is supposed to provide more spatial information than the 1D scanline sampling plan.

1.2.2 Data structure

Since the measurements were collected sequentially according to the spatial locality, the sequence of the data reflects the change in spatial location. Similarly, if we rearrange the measurements in the dataset by other properties that we are interested, the sequence of the measurements will reflect the variations relating to the change in this property. Measurements from Appleby and Cullercoats are predominantly fracture orientation data with a few kinematic data. The Laide property data structure is more complicated and includes fracture and fault orientation with a further attributes for spatial location and also the local heterogeneities where the data were collected.

1.2.3 Bootstrapping

Fracture orientations measured at different spatial locations were estimated by the bootstrapping method to investigate the spatial variation. In the Laide case study, it is also applied to delineate the relationship between the fracture orientation pattern and local lithological heterogeneities.

1.2.4 Variograms

The spatial correlation of the fracture orientation data was characterized by the variograms. The dissimilarity of the orientation measurements at different spatial locations is quantified by the average acute angular difference of any fracture planes separated by distance h. Therefore, equation 1.6 will be:

$$\hat{Y(h)} = \sqrt{\frac{1}{N(h)} \sum_{\|x_i - x_j\| \approx h} angular(Z(x_i), Z(x_j))^2} \tag{1.6}$$

where the angular $(Z(x_i), Z(x_j))$ is the acute angular difference between two fractures x_i and x_j which are separated by distance h.

Chapter 2

Granularity effects and spatial heterogeneity of fractures in deformed rocks

Our knowledge of the three dimensional (3D) characteristics of fracture networks is limited due to the inherent complexity that results from their initiation and mutual interaction, and constraints imposed by the incomplete sampling of rock volumes. Despite much work on fracture dimensions and geometries, little attention has been paid to the spatial heterogeneity in fracture orientations. At a well exposed section in N. England (George Gill, Appleby), we defined this 'granularity' by investigating the spatial heterogeneity in deformation band orientations in a high porosity sandstone using bootstrapping, variograms and hierarchical analysis. The analysis suggests that on a metre-scale the structures are multimodal with orthorhombic symmetry but at the 20 metre-scale they are bimodal. We suggest that this type of quantitative geospatial analysis can be used as a general tool to investigate spatial heterogeneity in structural systems.

2.1 Introduction

The prediction of rock properties such as permeability, strength, seismic velocity and anisotropy in the Earth's subsurface requires a quantitative understanding of the geometry and spatial attributes of fracture networks (e.g. Crampin et al. 1980; Barton and Zoback 1992; Laubach et al. 2004; Philip et al. 2005; Ortega et al. 2006). Current techniques for modelling fractured hydrocarbon reservoirs and aquifers require characterization of fracture geometries, sizes and spatial properties at a range

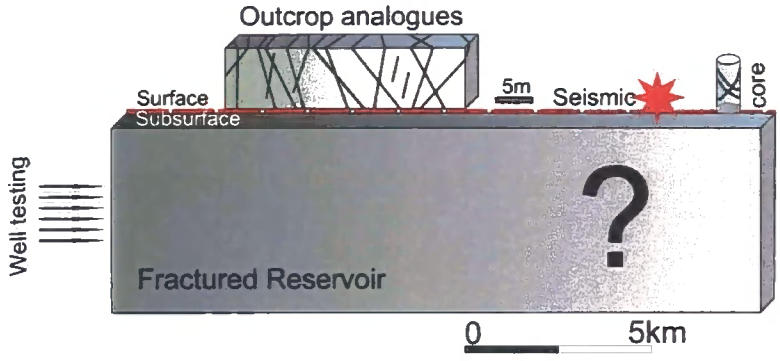

Figure 2.1: Schematic diagram illustrating some of the techniques used to study fracture networks at different scales. All this information is then required to predict the complete fracture network in three dimensions in the subsurface. This is relevant to studies of fluid reservoir properties and performance and also to natural seismicity at depth.

of scales (Fig. 2.1), from drill core (centimetres downwards) to seismic data (tens of metres upwards). The sampling method employed largely determines how well fracture networks can be characterised. Fracture system properties are usually derived using direct measurements from the subsurface in one dimensional (1D) drill samples and from two dimensional (2D) analogue sampling across outcrops (e.g. Gillespie et al. 1993). Establishing three dimensional (3D) fracture properties is particularly challenging (Gupta and Adler, 2006) and for modelling purposes it is generally assumed that the fractures are planar polygons or elliptical disks of varying size, and that they can be described by a maximum to minimum axial length ratio (Huseby et al., 1997; Gupta and Adler, 2006; Kemp et al., 2006). High-quality 3D seismic datasets aid description of fault populations in 3D yet are limited by the resolution (ca. 30 m), (e.g. Ellevset et al. 1998).

Fracture patterns viewed at different scales typically form a 'hierarchy' and the components visible at different resolutions reflect the 'granularity' of the system (Fig. 2.2). In sedimentology, granularity refers to the distribution of grain sizes within a sedimentary rock. Granularity in the more general sense is the relative size, scale, level of detail or depth of penetration that characterizes an object or activity (Zadeh, 1979). In this context, it can be thought of as the spatial heterogeneity of a fracture system at different scales of observations (Fig. 2.2).

We illustrate the importance of granularity in natural fracture systems using a case study from a sandstone outcrop that displays well developed deformation bands. The problem we encountered was that the first order hierarchy (the complete dataset

for the outcrop) seems relatively simple, i.e. two clusters which are NE-dipping and SW-dipping respectively. However, it is clear locally at metre-scale (lowest hierarchical level) that in most parts of the outcrop we can see more complexity, with 3 or more clusters developed. Importantly, when all the data were plotted using the stereoplot we were unable to delineate the multimodal character of the deformation bands observed locally. In this chapter, using a variety of statistical analyses, we demonstrate that this is due to significant variation in orientation on a local scale being masked by the overall spread of data on the scale of the outcrop as a whole. Our results show that spatial heterogeneity in fracture orientations can be delineated by analysing the fractures at different sampling sizes. Conversely, if the data are analysed at only one scale then important characteristics of the fracture system can remain hidden. This type of heterogeneity requires explicit understanding if more realistic prediction of natural fracture network geometries and their associated stress fields is to be successfully made in the subsurface.

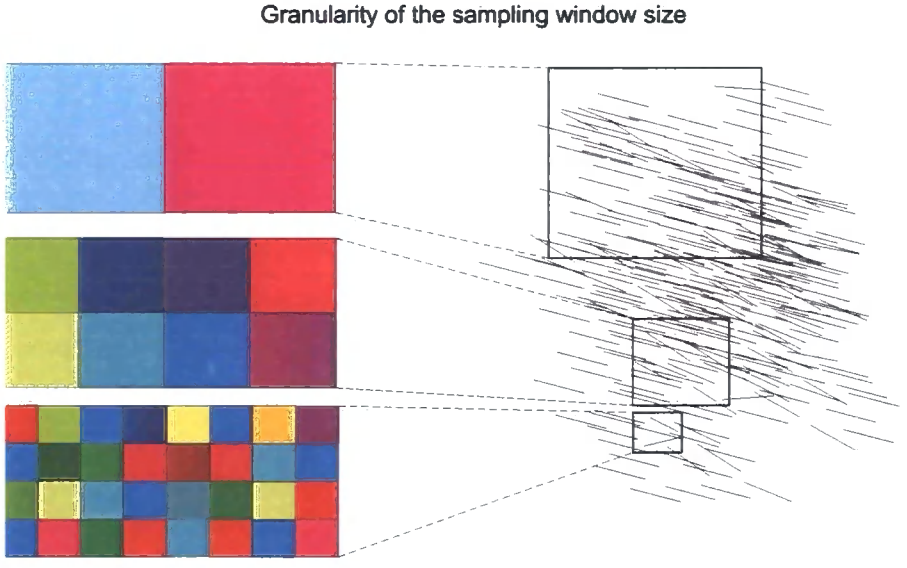

Figure 2.2: Schematic diagram illustrating the granularity of a sampling window system. The colour maps show a hierarchical relationship between measurements from different sampling window sizes: there are more variations shown as different colours at smaller scales than larger scales. Lines on the right are a schematic fracture network which is sampled at different window sizes shown as black boxes.

2.2 Geological background

An outcrop of fractured aeolian red sandstone occurs in the Permo-Trias Vale of Eden half graben at George Gill, Appleby, located to the east of the English Lake District and 20 km SE to Penrith (Fig. 2.3, NY716190). Fractures in the form of cataclastic deformation bands and deformation band clusters are well developed along both sides of a stream valley. These anastomosing structures are ubiquitous and are best displayed on a 40-metre long, south-facing cliff on the northern side of the valley (Figs. 2.3 2.4a). The host sandstone preserves widespread cross-bedding and is highly porous and poorly cemented, whereas the deformation bands (and deformation band clusters) are much finer grained, better cemented, and have lower porosity. The cross-bedding has a *subhorizontal to ca. 20° dipping angle towards NE* and there is no noticeable relative slip between the beds. This suggests that the cross-bedding – as a mechanical anisotropy, does not accommodate part of the bulk strain and the fracture pattern is not discernibly affected. Sigda et al. (1999) observed that low-porosity deformation bands can act as preferential groundwater flow paths through the vadose zone. The orientation, continuity and physical connectivity of deformation bands will determine their effectiveness as sealing or flow-reducing structures (Fossen et al., 2007).

The density of fracturing changes abruptly approximately 20-metres from the eastern end of the cliff. There are two major fracture types — single deformation bands and deformation band clusters, both of which have a diffuse bimodal distribution pattern on the stereonets (Fig. 2.4a b). In the zone of low fracture density towards the east, at least three (multimodal) sets of mutually cross-cutting fractures can be recognized in the field (Fig. 2.4b). They are similar to the arrays of faults in the Entrada and Navajo sandstones in southeastern Utah, where the faults form a network that usually has a rhombohedral pattern (Aydin and Reches, 1982). In the high density zone, the more closely spaced fractures almost obliterate the host rock entirely (Fig. 2.4c). Viewed as a whole, the deformation bands appear to be distributed into two broad clusters (bimodal) striking generally NW-SE and dipping moderately to steeply either SW or NE (Fig. 2.4). Offsets across deformation bands in the low density zone are typically 1~2cm at most, and around 5 cm in the high density zone. Isolated slickenlines are rarely preserved; examples discovered on a fracture plane beneath the cave shown in Figure 4 are dip-slip, plunging SW (Fig. 2.4d). At other localities along Hilton Beck near Red Brow (NY708201), 1 km NW from George Gill, slickenlines are more commonly developed on the polished fault surfaces, showing dip-slip normal faulting (Fig. 2.3). Faults that exhibit

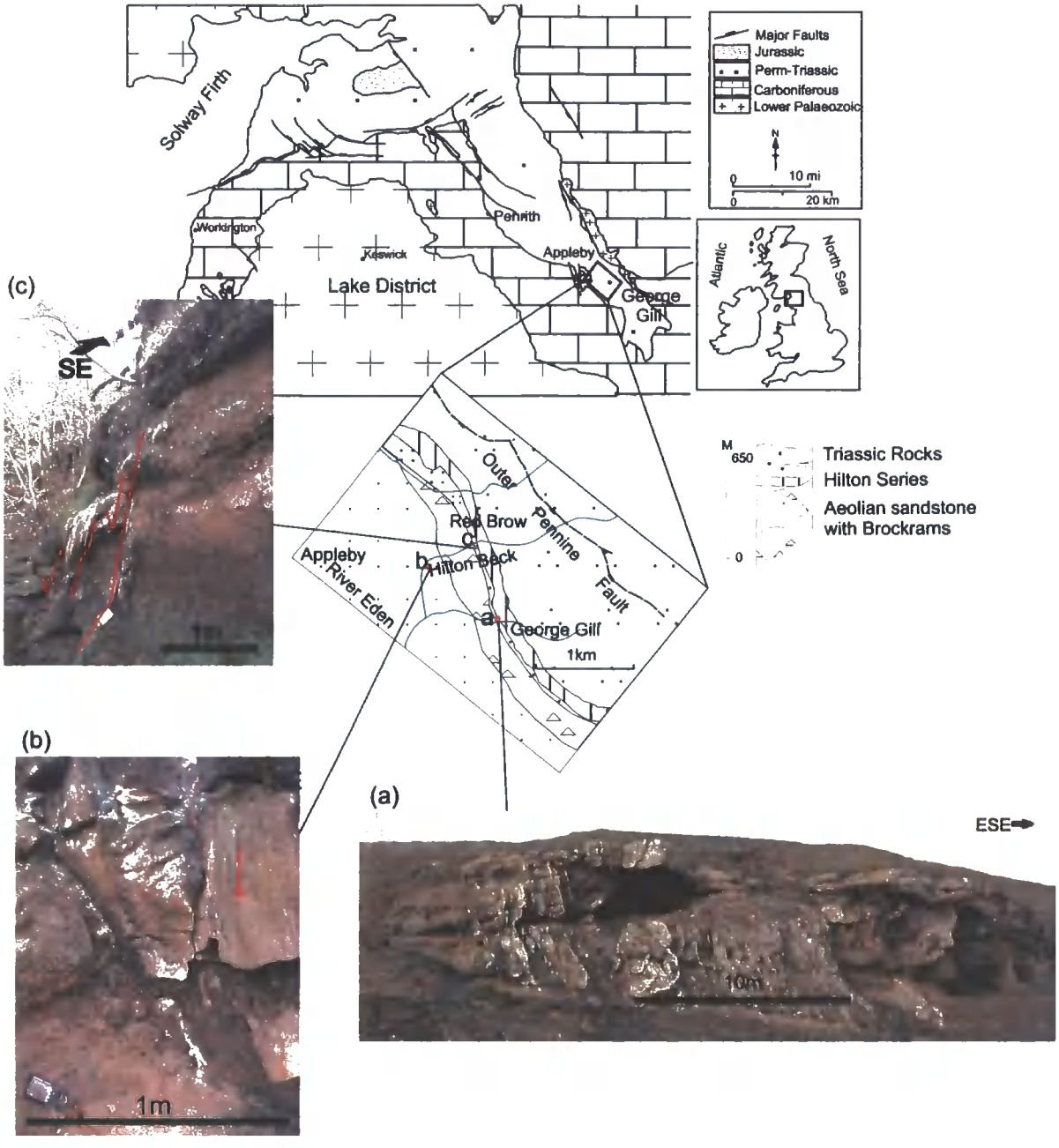

Figure 2.3: Regional geological map of the Penrith area showing the location of Appleby area which exposes Permian Aeolian sandstone with basil Brockrams breccias underlying thin-bedded muddy sand (Hilton Series) and Triassic rocks (detailed map), (after Versey 1938). (a) Locality a: a $\approx$ 40 m long cliff with anatomising deformation bands in the northern side of stream valley at George Gill. (b) and (c) Outcrop-scale normal faults trending NW-SE at locality b and c along Hilton Beck preserve well-defined dip-slip slickenlines on the exposed fracture surfaces of the deformation bands.

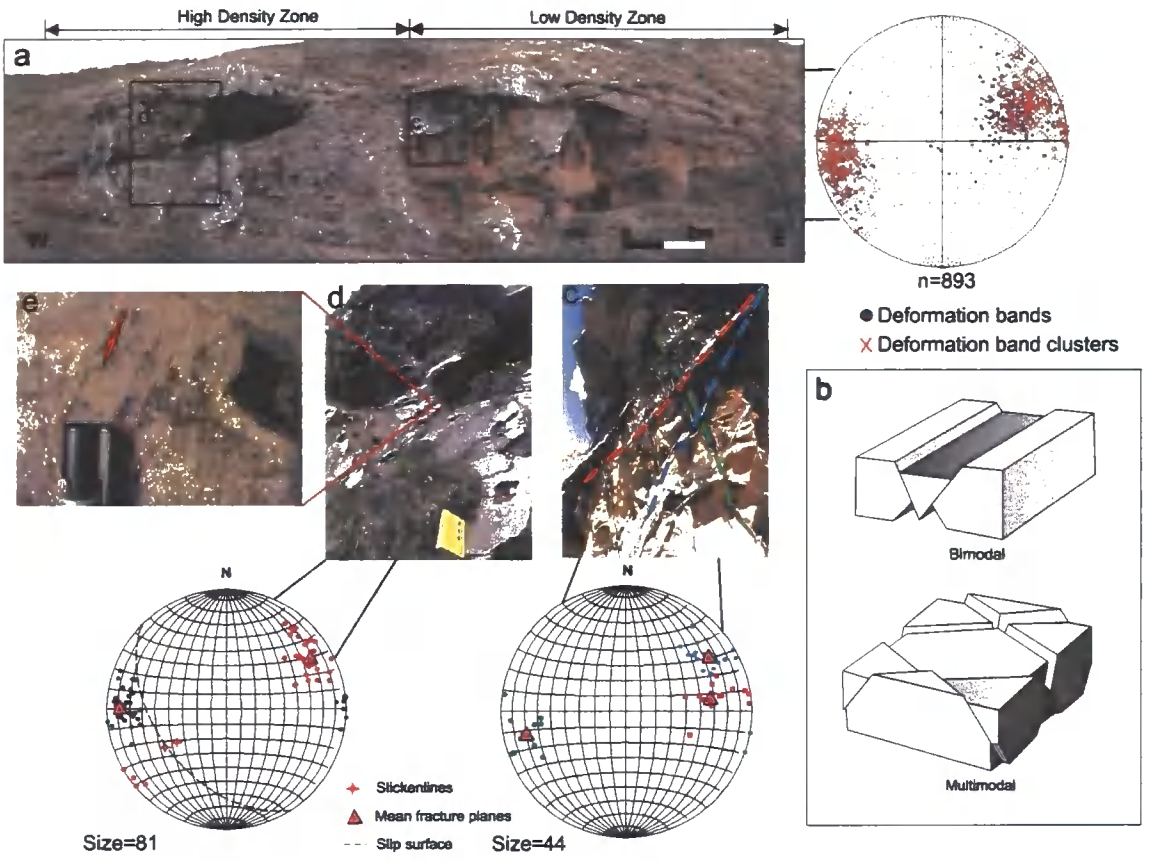

Figure 2.4: Fractures (deformation bands & clusters) on the south facing cliff at George Gill. (a) Overview of the cliff section showing how the fracture density changes in the middle of the outcrop (ca. 20 m from the east end of the cliff): in low density zone, fractures are mainly single deformation bands; in high density zone, they are mainly deformation band clusters with a few slip surfaces. Both single deformation bands and clusters display a diffuse bimodal distribution. (b) Block diagram illustrating the fracture patterns of bimodal and multimodal. (c) Locally developed multimodal deformation: three sets of cross-cutting fracture planes are obvious in the field. These different sets are correspondingly shown in blue, red and green dots on the stereonets below with point maxima presented in triangles. (d) A fracture plane with slickenlines (shown in (e)) indicating dip-slip displacement. Two fracture sets in different colours are shown on the attached stereonets. All the stereoplots follow Equal area projection, lower hemisphere.

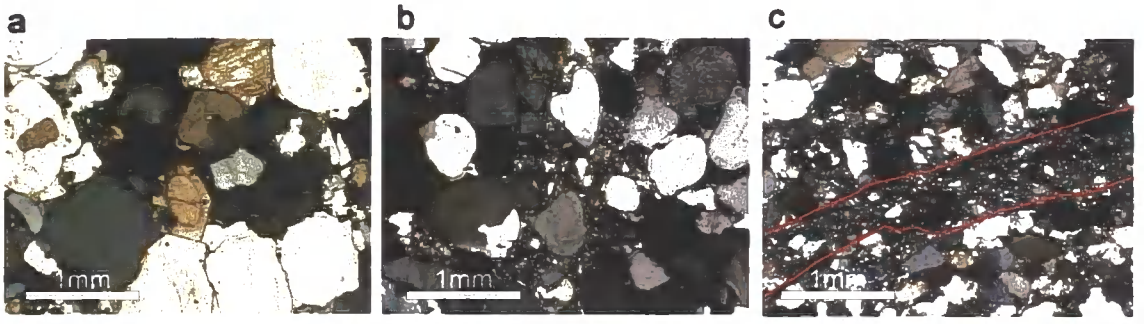

Figure 2.5: Thin sections from the undeformed host rock (a), outer zones (b) and inner zones (c), associated with undeformed parent sst., single deformation bands and deformation band clusters. Details of descriptions please refer to the text. CPL

slickenlines around Hilton Beck and George Gill generally trend NW-SE, suggesting a regional NE-SW extension. In this chapter, we focus on the fracture orientation data from the main outcrop at George Gill where we have investigated the spatial heterogeneity of the fracture networks in different sized sampling windows.

At microscopic scales, the undeformed host rock consists of ca. 80% quartz and ca. 10% feldspar grains, most of which are rounded and loosely packed. Cementation in the host rock is mainly due to pressure solution which occurs along the contacts between adjacent grains (Fig. 2.5a). In single (ca. 1 mm wide) deformation bands, grains were rotated, ruptured and more tightly packed than in the host rock (Fig. 2.5b). The offset is not obvious in a single deformation band as it does not represent a slip surface. Slip surfaces can, however, form within bands or, more commonly, along or within zones of multiple deformation bands, but this represents a more mature stage in the development of deformation band faults (Fossen et al., 2007). In deformation band clusters (ca. 5 cm width), where single deformation bands have coalesced, the original grains were intensively brecciated to form highly compacted cataclasites. Shearing is localized in narrow zones ($\approx$ 1 mm width), (Fig. 2.5c). The characteristics of the deformation bands from Appleby suggest that they closely resemble equivalent deformation bands described in a number of other regions (e.g. Underhill and Woodcock 1987; Antonellini and Aydin 1994; Fossen et al. 2007). Overall, in terms of deformation intensity, the zone of deformation bands agrees with the three-fold division of the fault evolution in high porous sandstones described by Aydin (1978).

2.3 Methodology and results

We use the term 'fracture' in this study to describe in a general sense of the discontinuous surfaces or zones (joints, faults and deformation bands etc.) generated by brittle deformation processes that particularly have an impact on the rock permeability. Firstly, we are primarily concerned with the spatial heterogeneity displayed by the system rather than the mechanics of deformation band formation and that secondly, we are using the outcrop to illustrate a general approach to the study of the spatial heterogeneity of structures.

To investigate the spatial variability and directional anisotropy in fracture datasets, each fracture orientation measurement should always be described by its position in a geographic or a Cartesian reference frame (Isaaks and Srivastava, 1989). Despite the large body of work concerning the statistics of directional (orientation) data (e.g. Mardia et al. 1979; Fisher et al. 1987), spatial heterogeneity in fracture datasets has not been considered in detail. This is rather surprising since it is generally agreed that systematic changes in fracture orientations could indicate rotations in palaeostress axes (e.g. Faulkner et al. 2006). More generally, the understanding of the variability of fracture orientations with respect to their spatial position in the rock is an important component in the description of the complete fracture network.

In this study, we investigated 3 distinct aspects of spatial heterogeneity in the fracture orientation dataset: (1) geometrical clustering; (2) spatial correlation; (3) spatial variation. In this study, geometrical clustering refers to the clusters in fracture orientations from location to location along the outcrop. Spatial correlation describes the similarity of any two orientation measurements separated by certain distances. Spatial variation describes the change in the fracture orientation with its spatial location. We use three corresponding techniques to study these three aspects: (1) bootstrapping; (2) semivariograms; and (3) hierarchical analysis.

2.3.1 Data Acquisition and manipulation

We collected approximately 950 fracture orientations in 1m sized windows along a 1D scanline across the outcrop. The location of each sampling window is defined by the distance from the east end of the cliff to the centre of the window (Fig. 2.6). Orientations were recorded directly onto digital photographs using a Tablet PC (Clegg et al., 2006), to locate the precise position of the measurement on the outcrop (this allows every measurement to be validated at a later date, if necessary). In the low density zone, any accessible fractures are measured in the sampling window so

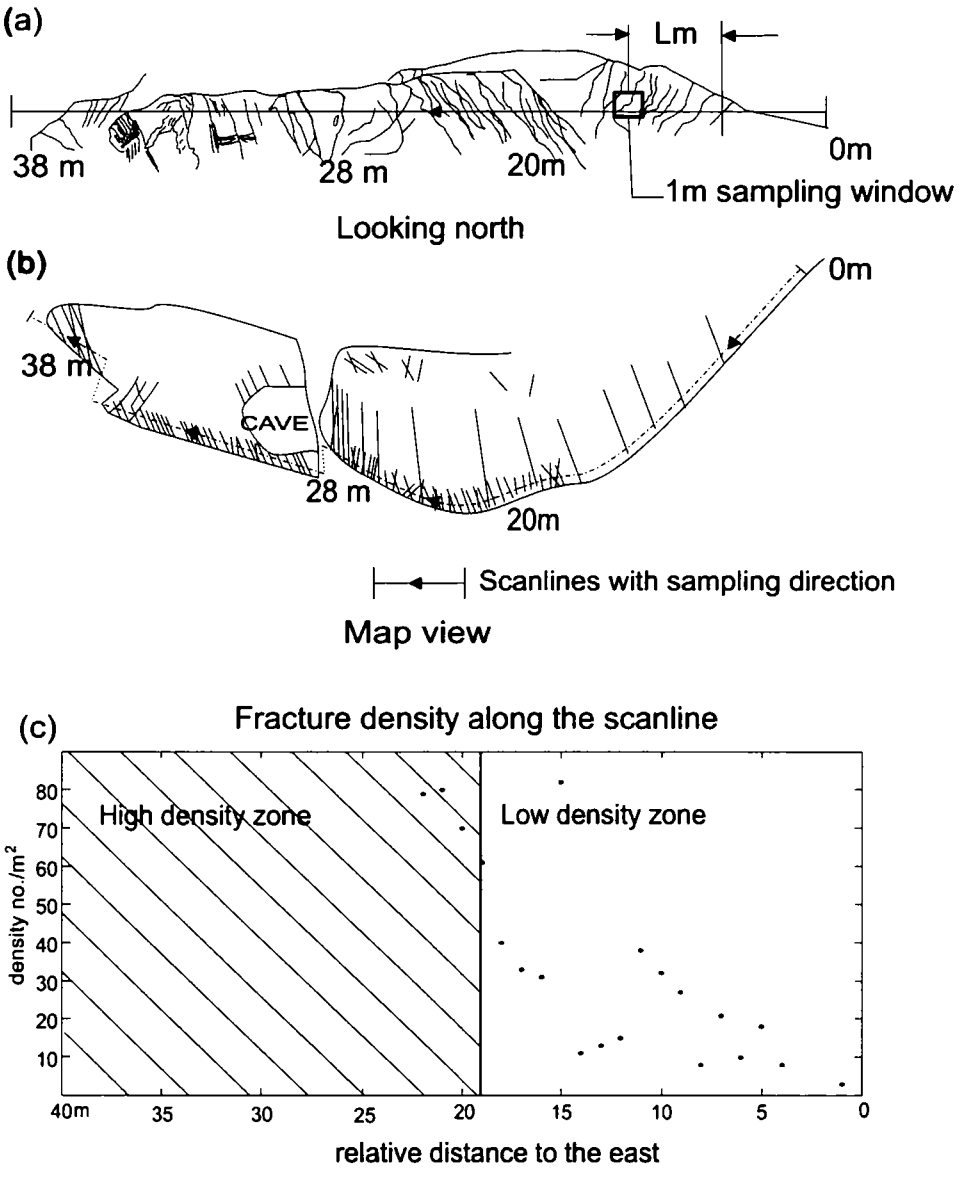

Figure 2.6: (a) Sketch section (looking N) of the cliff at George Gill showing a typical 1 m sampling window which was moved sequentially westwards relative to the sample line origin in the east (0 m). (b) Map view showing the scanline (dotted along the cliff base). (c) Plot of fracture density vs. distance from the east end of the cliff showing that there is an increase in the density as approaching high density zone (shaded area).

that the data size will reflect the fracture density (Fig. 2.6c). In the high density zone, sufficient sample size is obtained by randomly collecting data in the area covered by the sampling window. Additionally, for curvy fractures, more than one measurement are taken to record the substantial change of fracture orientations.

The mutually cross-cutting fractures in the relatively homogeneous sandstone exhibit a broadly conjugate pattern at the outcrop scale, with approximately two diffuse clusters plotted on the NE and SW quadrant of the stereonets (Fig. 2.4a). Therefore in this case study, we are confident to split the dataset into two major sets (NE- and SW-set) by the strike of the fracture plane. However, we are unable to resolve subclusters within each major fracture set purely based on orientations because natural variations occur in fracture orientation — often obscure more complex clustering patterns at different scales (c.f. Healy et al. 2006b). Instead, we focus on investigating the spatial heterogeneity in each major fracture set to delineate the underlying data structures.

2.3.2 Bootstrapping

Bootstrapping is a statistical method for estimating the sampling distribution of an estimator by sampling with replacement from the original sample (Efron, 1982). It is particularly useful in analysing orientation data since the distribution of the statistics commonly used for inference on the spherical distributions are more complex than those arising in standard normal theory (Mardia and Jupp, 2000). A simple diagram of the spatial location along scanline vs. stereoplots of fracture orientations may be valid in resolving variations in datasets of large spatial heterogeneity (e.g. Wilson et al. 2006). But often this heterogeneity remains hidden due to the diffuse distribution of the stereoplots (Fig. 2.4a). It is proposed that bootstrapping is robust to 'pull-out' such hidden information in the orientation datasets.

To investigate the geometric clustering in the orientation datasets, sequentially bootstrapped means are compared with randomly bootstrapped means. Here, the sample means are bootstrapped in sequence by selecting the measurements in a particular order according to their spatial locations: fractures spaced closest together are selected and the mean orientation is calculated from them. We sampled a chosen number of such spatially close measurements from the east end of the cliff and calculated the vector mean (e.g. Mardia et al. 1979). We then repeated the same operation on fracture measurements working progressively towards the west end of the cliff. This use of a 'moving window' with a large 'overlap' highlights the fracture planes of similar orientations in a spatially correlated context. Finally, we calculated

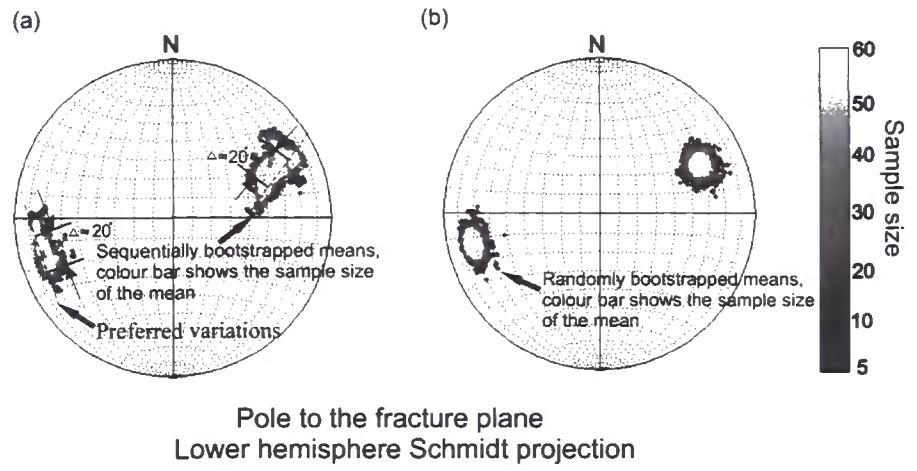

Figure 2.7: Results of bootstrapping. (a) Sequentially bootstrapped means in the NE and SW subset. Dashed lines are the preferred $\approx 20^o$ variations observed for each subset. Colours indicate the sample size of the mean. (b) Randomly bootstrapped means in the NE and SW subset: the two tight clusters show no preferred variations.

the mean orientations (c.f Mardia and Jupp 2000) of similar sized samples selected at random from the whole dataset (i.e. ignoring the spatial position of the measurements). This process was then repeated many times, for samples of different sizes. If there is spatial clustering in the datasets, the sequentially bootstrapped means should show different behaviour compared to randomly bootstrapped means. This difference can be shown by plotting the means on stereonets (Fig. 2.7). Furthermore, the relation between the spatial position and the orientation of the fractures was analyzed by the 'moving window bootstrapping': a simulation was launched in each 'moving window' to generate pooled mean orientations which were colour-coded from from a greyscale (the colour is determined by the spatial position of the 'moving window') to estimate the spatial variation (Fig. 2.8). This simulation is in some ways analogous to the moving sampling windows used in the field: fracture orientations are sampled in a window that moves across the datasets. However, unlike in the field, this approach defines the window size as the number of orientation data that immediately adjacent to each other to form a sub-dataset in which the random sampling is applied for a large number of repetitions. The window moves with a 99% overlap: each adjacent window will have only 1 different measurement, suggesting that sampling windows in the dataset close to each other will have similar bootstrap estimations.

Stereoplots illustrate that there are both substantial variations in the fracture

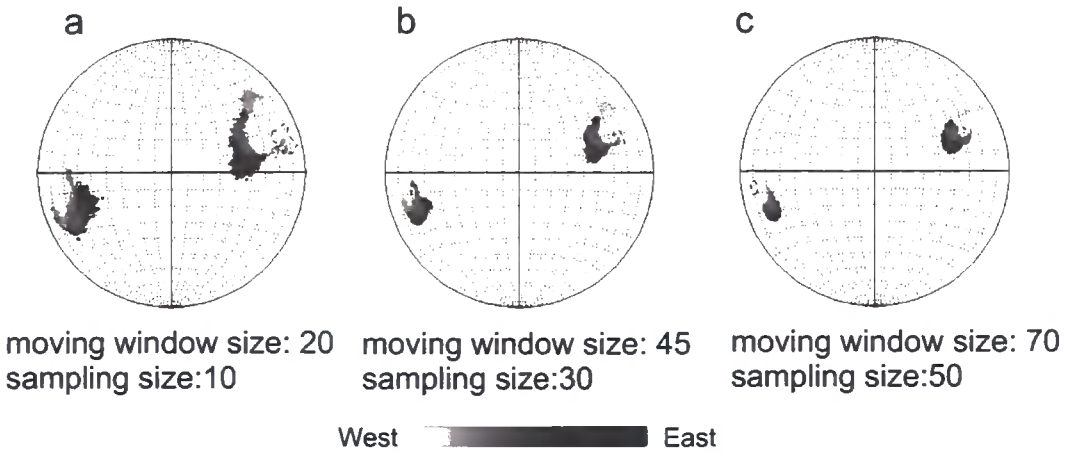

Figure 2.8: Spatial variation in fracture orientation shown by the 'moving window bootstrapping'. The colour bar represents the change of the spatial location from the east to the west of the cliff. A large number of bootstrapped orientations from a 'moving window' will be allocated the same colour when they are plotted on the stereonets. The moving window size is the size of a collection of closely spaced measurements in which repetitive sampling is taken with a chosen size (sampling size) to estimate the local distribution. (a)-(c) Results of the 'moving window bootstrapping': there are systematic and substantial variations in both major clusters as the spatial location changes from east to west of the cliff; changing the moving window size will not exert large impact on the spatial variation pattern.

orientation for the NE- and SW-dipping sets. The sequentially bootstrapped means vary in an approximately 20^o range in well-defined directions (Fig. 2.7a). The NE-dipping set varies substantially in the horizontal plane (i.e. there is more variation in strike than dip), whilst the SW-dipping set varies substantially in the vertical plane (i.e. dip varies more than strike), (Fig. 2.7a). Figure 2.8 shows that the fracture planes in both NE- and SW-dipping sets rotate systematically: as the location moves from east to the west end of the cliff, NE-dipping fractures vary clockwise (looking down) in a horizontal plane and SW-dipping fractures become steeper, both of which show a variation of approximately 20^o. By contrast, the results of the random bootstrapped means reveal two sets of tight clusters on the NE and SW quadrant of the stereonet respectively (Fig. 2.7b), which approximately follow Fisher distribution model (Fisher et al., 1987). The results from both Figures 2.7 and 2.8 are not sensitive to changing sampling size (Figs. 2.6a, 2.8), suggesting a fairly strong heterogeneity in the spatial variation of the dataset. Additionally, as most single deformation bands are in the low density zone towards the east of the

outcrop, and most deformation band clusters are in the high density zone towards the west of the outcrop, the bootstrapped results (Fig. 2.8) yield a substantial difference in the orientations of these two fracture types.

2.3.3 Semivariograms

The semivariance, $\hat{\gamma}(h)$ is used to quantify the spatial correlation for spatially distributed datasets (Isaaks and Srivastava, 1989), (c.f. 1.1.3), and is described by equation 1.4. For spatially heterogeneous datasets, closely spaced measurements are expected to have a higher correlation than measurements spaced further apart. In this study, it is important to define a suitable parameter to represent the difference between two geographically separated measurements, because the orientation data are bivariables and can be illustrated as vectors distributed on a unit sphere. Hence, the difference between two measurements cannot be adequately represented by simply subtracting one from another. Instead, we use the angular difference between the poles to the fracture planes to describe their dissimilarity (also see La Pointe 1993). Equation 1.4 was therefore modified for calculating the semivariance to reveal the spatial correlation in the orientation dataset thus:

$$\hat{\gamma}(h) = \sqrt{\frac{1}{2N(h)} \sum_{\|x_i - x_j\| \approx h} angular(Z(x_i), Z(x_j))^2} \qquad (2.1)$$

where angular (Z(x_i), Z(x_j)) is the acute angle between the poles to two fracture planes measured in the plane normal to their mutual intersection; $\|x_i - x_j\| \approx$ h represents any pairs of fractures separated by the geographical distance h; N(h) is the total number of pairs of fractures whose geographical distance is determined by $\|x_i - x_j\| \approx$ h. For convenience, we keep the terminology 'semivariance' and symbol $\hat{\gamma}(h)$ to describe the modified parameter on the left side of the equation 2.1. Important features of the semivariogram are: Range: as the separation distance between pairs of measurements increases, the corresponding semivariance will also generally increase. Eventually, an increase in the separation distance no longer causes a corresponding increase in the semivariance and the semivariogram reaches a plateau. The distance (lag h) at which the semivariogram reaches this plateau is called the 'range'; Sill: The plateau the semivariogram reaches at the range is called the 'sill'. When the semivariance reaches the sill, measurements separated by the corresponding distance are no longer spatially correlated; Nugget effect: Though the value of the semivariogram for h = 0 is strictly 0, several factors, such as sampling error and small-scale variability, may cause sample values separated by extremely small

distances to be very dissimilar. The jump from 0 at the origin of the semivariance at extremely small distances is called the nugget effect (Isaaks and Srivastava, 1989).

The semivariance calculated from the fracture orientation data (Fig. 2.9) shows that the nugget effect of the whole dataset (NE- and SW-dipping subsets combined) is around 17^o, suggesting that fracture orientations measured close to each other vary in the range of ca. 34^o (i.e. twice the semivariance). Similarly, the average angular difference between two closely separated fractures in the NE- and SW-dipping subsets is about 19^o and 23^o respectively, showing that there are still significant variations in each subset. Note that the nugget effect of the whole dataset is substantially larger than for each of the subsets (NE- and SW-dipping). As the fractures here are mutually cross-cutting, these results can be interpreted to be the result of locally developed multimodal brittle deformation (c.f. Healy et al. 2006b). The semi-

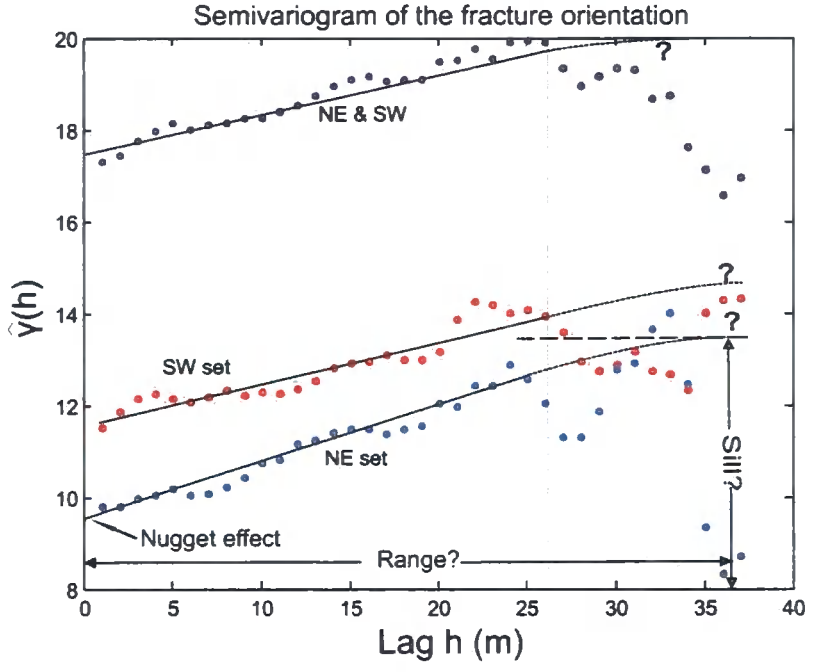

Figure 2.9: Semivariogram of the fracture orientation. The distance (lag h) separating any two measurements and semivariance show a strong positive correlation. In the whole dataset, the nugget effect is $\approx 17^o$. In the NE- and SW-dipping subsets, the nugget effect is $\approx 9.5^o$ and $\approx 11.5^o$. Shaded area indicates region where it is uncertain to determine the sill and range due to limited number of pairs of measurements.

variance linearly increases with the lag h before reaching the shaded area shown on Figure 2.9. High fluctuations in this shaded area are due to lack of enough pairs

of measurements separated by a large distance. Hence, there is high uncertainty regarding the accuracy of the sill and range shown, because the outcrop is not large enough to be sure that we have reached the true sill. Whilst the point at which the semivariance curves should level out and reach the sill are not well constrained, the semivariance and lag h are positively correlated at the smaller scales represented by the unshaded area (Fig. 2.9). It appears that the fractures have a strong spatial correlation up to at least the 25 m scale.

2.3.4 Hierarchical analysis

To investigate the granularity in fracture orientations, we increase the size of the sampling window by combining measurements from adjacent spatial positions. We can also model the granularity by subdividing our fracture datasets into different sampling window sizes to form a hierarchy of observations, from small (e.g. metre-scale) to relatively large (tens-of-metre) scales (cf. Fig. 2.2). This analysis gives a tool to gain insights in the spatial variation of the fracture orientations over the available scale-range. We chose 3-metre, 5-metre, 10-metre and 20-metre scales to investigate the patterns of spatial variation in the fractures from this 40-metre long cliff. Upscaling is realized by combining the original 1-meter sampling windows into progressively larger window sizes. Measurements at 3-metre scale, for example, are simply a combination of three adjacent 1-metre sampling windows. We can calculate the standard errors of the mean from different windows of the same size to assess significant spatial variations at that scale.

Our results show that the spatial variations in fracture orientations become less random from 3-metre to 20-meter scales in both subsets (Fig. 2.10). Numbers annotating the mean fracture orientations in Figure 2.10 represent the relative spatial positions on the cliff, with larger numbers indicating data located further to the west. For example at the 3-meter scale, in the SW-dipping set, data point no. 1 refers to measurements made 0-3 metres from the east end of the cliff; no. 2 to measurements made from 4-7 metres and so on (Table 2.3.4). Dashed lines on Figure 2.10 show variations which are similar in magnitude to the results of sequentially bootstrapped means. As the sampling window moves towards the west end of the outcrop, the spatial variations in orientation are relatively random at 3-meter scales. At larger scales (10-meter and 20-meter), however, there are systematic spatial variations in both subsets: in the NE-dipping set, the pole to the fracture plane rotates progressively clockwise, whilst in the SW-dipping set it rotates from a steeper to a shallower plunge (Fig. 2.10)

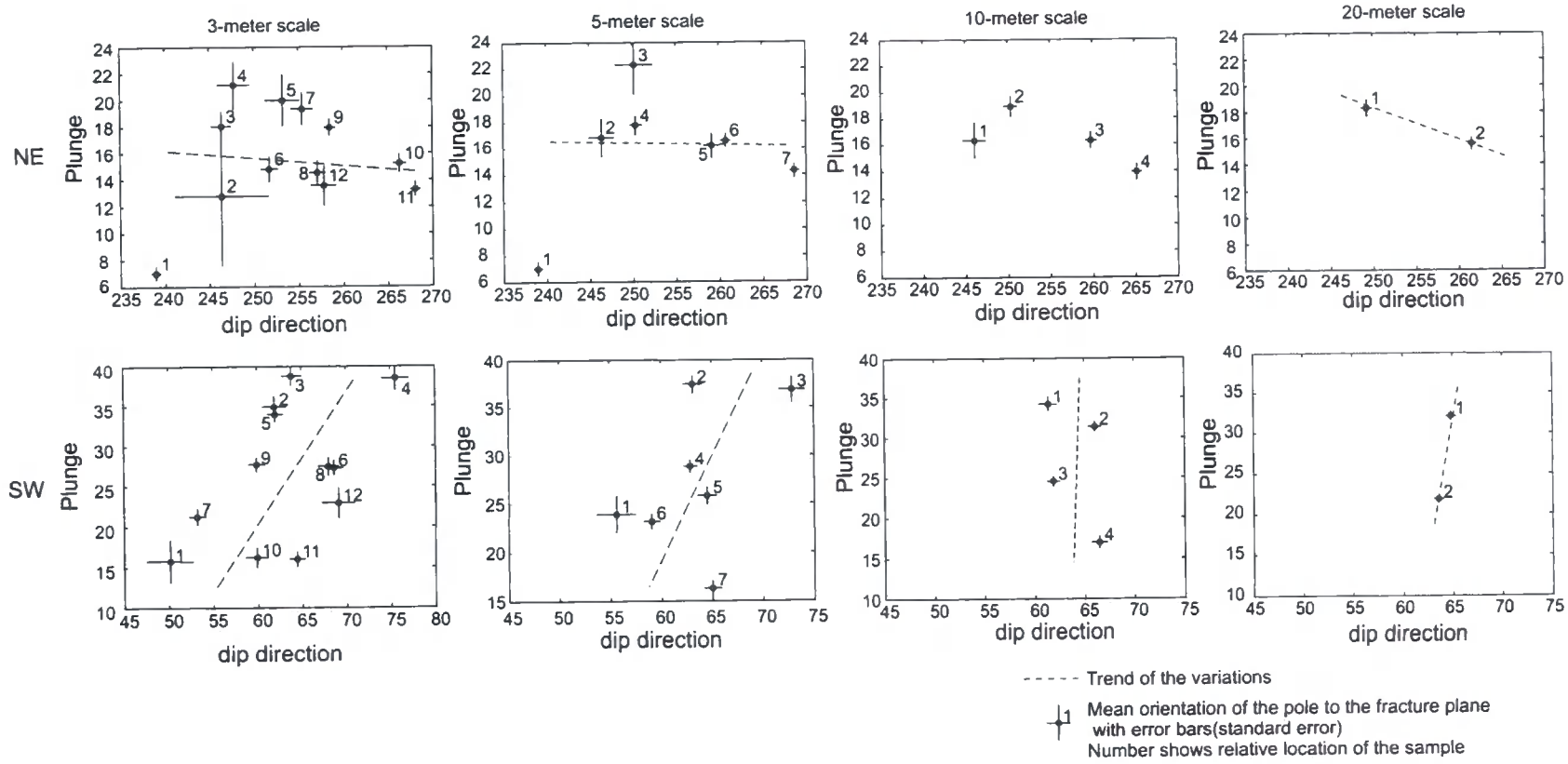

Figure 2.10: Results of the hierarchical sampling of the mean fracture orientation. Data points are the mean poles to the fracture planes for sample sizes of different areas mapped from lower hemisphere Schmidt projection to a 2D Cartesian coordinate frame. The number of each point indicates the relative location along the outcrop from east (lower number) to west (higher number). Dashed lines show the progressive change in orientation of the sequentially samples bootstrapped means. See text for further details.

Table 2.1: The relation of the sampling window size and the spatial location. Numbers in the first column are the relative location number as shown in the label to each point in Fig. 2.8. The last four columns show the corresponding real locations along the scanline where the measurements were taken, at four different sampling scales.

		Scale			
Hierarchical sampling	No.	3m	5m	10m	20m
	1	0-3m	0-5m	0-10m	0-19m
	2	4-7m	5-10m	10-20m	19-38m
	3	7-10m	10-15m	20-30m	x
	4	10-13m	15-20m	30-38m	x
	5	13-16m	20-25m	x	x
	6	16-19m	25-30m	x	x
	7	19-22m	30-35m	x	x
	8	22-25m	x	x	x
	9	25-28m	x	x	x
	10	28-31m	x	x	x
	11	31-34m	x	x	x
	12	34-37m	x	x	x

2.4 Discussion

2.4.1 Spatial heterogeneity

The bootstrapping method applied here seems to be the fastest and most robust way to explore the dataset to reveal the clusters in fracture orientations. As the real field data can be very noisy, simply comparing the orientation data from different groups (e.g. spatial location, lithology) without using some statistical methods is of dubious value unless there is a 'big' difference in some case. The sampling size is measured in terms of number of fractures whose locations may or may not be the same. However, as they are spatially close to each other, the 'moving window' with large overlap will eventually delineate the preferred variations in both subsets (Fig. 2.7a). The moving window bootstrapping will further reveal the substantial spatial variation in the fracture orientation by estimating the local distribution pattern in each moving window (Fig. 2.8).

In the semivariogram analysis, the sampling size is defined as the number of pairs of two fracture orientations which are separated by a given distance. It ap-

pears that the fracture orientation data has a strong spatial correlation for any two measurements up to at least 25 m spacing (Fig. 2.9). This may suggest that in this scale range, the variations observed from different sampling window sizes could be substantially different. Hierarchical sampling correspondingly shows, from meter to tens of meter scales, the significant difference in the fracture orientations. This sampling strategy does not change the preferred variations in both subsets (Figs. 2.7 2.10), and the results of the fracture orientation at 10- and 20-meter scale of figure 10 are consistent with the spatial variations shown in figure 2.8.

The spatial heterogeneity at sub-meter scales yields that there is a spread of variations in each subset (19^o in the NE-dipping set and 23^o in the SW-dipping set). The stereoplot for the bulk fracture population shows two diffuse clusters on the NE and SW sides of the plot (Fig. 2.4a). Traditionally, the mean orientation of these two clusters would be used to infer an Andersonian conjugate set of bimodal shear fractures as a best approximation. Such conjugate fault sets can only accommodate 2D plane strain deformations (Reches and Dieterich, 1983; Reches, 1983). The field observations suggest that the cross-cutting deformation bands exhibit an orthorhombic symmetry at sub-meter to meter scales. Such patterns are more consistent with 3D non-plane strains which are likely to be the main type deformation that occurs in the lithosphere (e.g. Dewey et al. 1998; Jones et al. 2005). Recent numerical modelling has suggested that this orthorhombic symmetry is a predictable consequence of the 3D interaction of mode I microcracks during the initial stages of shear fracture nucleation and growth in various types of rock masses (e.g. Reches 1978; Aydin and Reches 1982; Reches 1983; Healy et al. 2006a).

The data from the George Gill cliff section also reveal a systematic, east to west change in fracture orientations along the cliff. These characteristics of the fracture network have been demonstrated by the moving window bootstrapping and hierarchical sampling techniques. The density of the fractures increases sharply within a few meters at about 20 m westwards from the east end of the cliff section we studied (Fig. 2.6c). These changes appear spatially related to the steeply dipping NW-SE trending normal faults developed in the aeolian sandstone along the Hilton beck to the NW of George Gill (Fig. 2.3). However, the exact location and mechanisms of the major fault that controls the geometric and spatial heterogeneity of the fractures in George Gill still remain a open question. We propose, that the spatial heterogeneity observed in the cliff section is due to the presence of a NW-SE trending normal fault which dips to the SW (or NE), (Fig. 2.11). Equivalent changes in fracture orientations are observed in many natural systems as one passes from the wall rocks into the damage zones of larger faults (e.g. Shipton and Cowie 2001; Faulkner et al.

2006; Johansen and Fossen 2008) and lend support to the hypothesis that a larger fault lies close to the west end of the outcrop in George Gill. Another speculative

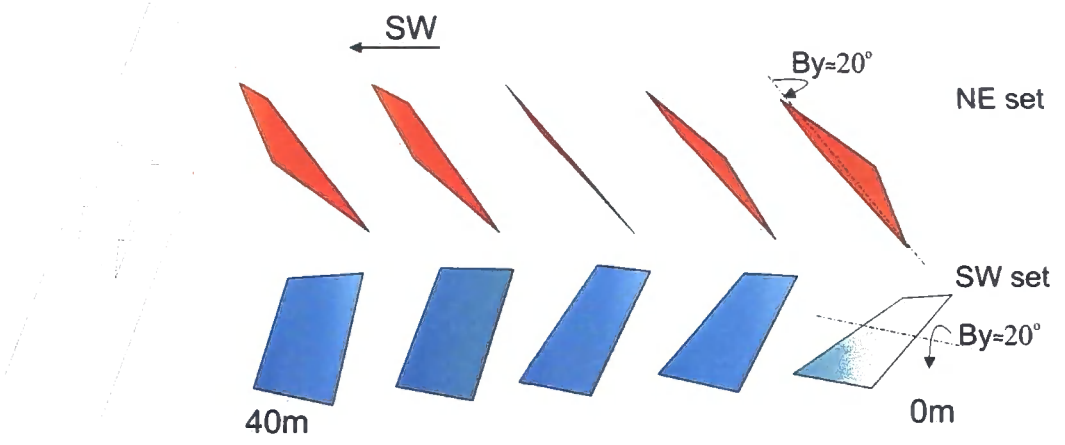

Figure 2.11: Schematic diagram showing the observed systematic spatial variations in the orientations of the bulk NE- and SW-dipping fracture planes along the cliff section. Postulated normal fault at west end of section is also shown.

model is that the fracture distribution might be controlled by the major fault tip that propagating from beneath or laterally. However, the ongoing slip surfaces and interlinked high density fractures (deformation bands and clusters) present in the west part of the cliff section suggest that the fault tip model may not produce such a high fracture density zone (c.f. Shipton and Cowie 2001). Alternatively, the sharp increase in the fracture density in the center of the cliff section suggest that a major fault may cut through the center of the cliff section, producing the high fracture density zone (west part) and low fracture density zone (east part). In general, these fractures exposed in the section can be controlled by more than one major slip surfaces, indicating that the spatial heterogeneity in fracture sets investigated in this study may simply be the bulk effect of these major faults.

2.4.2 Scaling issues

The scaling of fracture properties can in principle be determined quantitatively by comparing natural datasets with known, idealised distribution models, such as fractal, log-normal, exponential, etc. (Bonnet et al., 2001). However, previous workers have ignored that these properties are all 'scale-integrated' features: parameters such as fracture length, aperture and throw are measured in terms of length, i.e. scale is directly reflected by the size of the properties themselves. In a given sampling

area, the distribution model is principally determined by the cumulative probability of the parameter itself and this is enough to describe the scale at which these fractures are measured. Power-law and fractal geometries provide a widely applicable descriptive tool for fracture system characterization (Bonnet et al., 2001). Fracture orientation, on the other hand, has no direct intrinsic correlation to length. This leads to a problem in sampling this property in the field: How can an appropriate link between orientation and scale be created? Fractures form in a specific orientation with respect to the principal stress directions, however it is known that the orientation of the principal stress directions one infers depends upon the scale of observation (Tikoff and Wojtal, 1999). Here, we suggest it is appropriate to use the term 'granularity' to describe the hierarchical variation at different scales rather than the term 'scaling', because measurements of orientation are 'scale-isolated' and therefore have no direct relation to the length. Hence, to understand the distributions of fracture orientations at different scales, we have to define the sampling window size independently from the type of measurements being taken (e.g. strike, dip, dip direction). Therefore, methods for characterizing the scaling of fracture sizes cannot be routinely applied to fracture orientation data. Our approach here has been to change the size of the sampling window as an indirect way of representing the change of scale. Future work should attempt to define general statements that correlate the relationship between fracture orientations and fracture sizes at different scales. Qualitative field observations often suggest that, at outcrop scales, there is little or no obvious relation between the orientations and fracture lengths. At a regional scale, however, this relationship may become more obvious as major faults often appear to control the bulk orientation of nearby fracture zones. Such granularity in sampling the fracture orientations relating to the distribution of the fracture size is an interesting issue which requires further study. It is not easy, however, to analyse the orientation datasets relative to their spatial positions, especially for datasets from outcrops of limited size (such as the case study presented here). Where possible, it would be useful to quantify fracture orientations from outcrop to regional scales, because this could allow an interpolation technique to be developed which can estimate fracture orientation values based on limited observations. This applies not only to the fracture networks on the surface, but also to those found in the subsurface. Flat pavements covering a large area, or long straight cliffs with simple fracture distribution patterns should represent ideal field areas to carry out such further studies.

2.5 Conclusions

Quantifying spatial variation in fracture orientation is key to understanding the geometry and connectivity of 3D fracture networks. The fractures (deformation bands and deformation band clusters) on the cliff at George Gill, Appleby, N. England show significant spatial heterogeneity in their orientations. This heterogeneity is likely to be controlled by the development of a NW-SE trending, SW-dipping normal fault adjacent to the cliff section studied. Multimodal fracture sets are developed locally at sub-meter to meter scales and explain why the spatial variations change from systematic to random when downscaling from tens of meter to meter scales. The present study represents one of the first systematic accounts of the spatial heterogeneity of natural fracture orientations and illustrates that a great deal more work remains to be done if we are to be able to describe and accurately predict the complete fracture system in three dimensions.

Chapter 3

Structural controls on fracture orientations in homogeneous host rocks

Field-based studies indicate that the orientations and slickenline patterns of fracture systems developed during single obliquely convergent or divergent deformation events are often markedly heterogeneous in wall rocks adjacent to major faults even in situations where the host lithologies are very homogeneous. To quantify this heterogeneity more rigorously, a spatial analysis of fracture orientations and associated slickenline lineations was carried out in a homogeneous sequence of Permian aeolian sandstones deformed in the hangingwall of the 90-Fathom Fault, a dextral-oblique normal fault exposed at Cullercoats Bay, NE England. Two sampling directions were adopted, oriented orthogonal and parallel to the trace of the major fault. The results show that in traverse directions orthogonal to, and moving towards, the 90-Fathom Fault, fracture orientation patterns change markedly allowing the definition of a well-defined, ca. 100 m wide damage zone of fracturing adjacent to the fault core. In the outer portion of the damage zone, at the transition with the less deformed protolith, fractures form simple bimodal conjugate arrays of oblique-slip normal faults. Nearby the fault core, the fracture pattern becomes polymodal, with at least 4 main orientation clusters recognised. They are arranged into mutually cross-cutting arrays of dextral strike-slip and dip-slip normal faults, each with distinct orientations. Fracture orientations measured adjacent to the fault core in a direction parallel to the main fault trace, show consistent polymodal distribution patterns with no substantial spatial variations along strike. It is interpreted that reactivation of the pre-existing Carboniferous, basin-bounding structure has controlled

the spatial heterogeneity of fracturing and the partitioning of strain into contemporaneous arrays of strike-slip and dip-slip faults in the damage zone in the hanging wall of the fault. Our findings illustrate that fracture orientations and kinematics within damage zones adjacent to major faults cutting sedimentary basin infills are likely to be complex and substantially influenced by the reactivation of pre-existing faults in the immediately underlying basement. This is particularly relevant where reactivated faults lie significantly oblique to regional extension vectors.

3.1 Introduction

The fault core and around damage zones of fault zones provide valuable information on understanding the fluid flow, mineralization and deformation mechanisms (Chester et al., 1993; Caine et al., 1996; Sibson, 2000; Shipton and Cowie, 2003). Many features of the secondary structures are believed to vary substantially across fault zones such as the damage zone width (Knott et al., 1996; Shipton and Cowie, 2003), fault offsets (Shipton and Cowie, 2001), deformation density (Shipton and Cowie, 2003; Johansen and Fossen, 2008), and orientation modal (Shipton and Cowie, 2001), etc. The contrast of the permeability between damage zones and fault cores is able to invoke cyclical fluid overpressure to complicate fracture patterns (Chester et al., 1993; Faulkner et al., 2006). It is well known that the localization of damage zones around fault core may be strongly influenced by the presence of pre-existing structures such as layering, foliation, faults and shear zones (Dewey et al., 1986; Holdsworth et al., 1997). In many cases, these pre-existing structures lie significantly oblique to the renewed regional transport direction and if reactivation occurs they will commonly control the spatial attributes of the newly formed structures (e.g. Fossen and Tikoff 1993; Tikoff and Teyssier 1994; Jones et al. 1997; Lin et al. 1998; Beacom et al. 2001). 3D transtensional and transpressional strains have been investigated and modelled to highlight the physical process based on analytical and experimental models (e.g. Sanderson and Marchini 1984; Withjack and Jamison 1986; Tron and Brun 1991; Fossen and Tikoff 1993; Jones et al. 2004, to name but a few) It has also been recognized that kinematic partitioning of 3D non-coaxial and coaxial strains appears to be a characteristic feature of many such oblique deformation zones (e.g. Dewey et al. 1998; Lin et al. 1998; Dewey 2002; Holdsworth et al. 2002). There are likely to be many factors that control such partitioning behaviour operating across a broad range of scales. These include the presence of pre-existing structures (e.g. De Paola et al. 2005a,b), but also other factors such as variations

in host rock lithology (e.g. Jones and Tanner 1995), contrasts in the rheological behaviour of materials experiencing (strike-slip) simple shear vs (dip-slip) pure shear (e.g. Lin et al. 1998) and controls exerted by regional scale boundary conditions (e.g. Molnar 1992; Tikoff and Teyssier 1994). It is clear, however, that there remains a lack of detailed field studies of the spatial attributes and inter-relationships of structures that developed in transpressional/transtensional strain regimes, especially those in the brittle deformation field (e.g. Dewey 2002; Taylor et al. 2008).

Fracture orientation, together with size (length, thickness/width) and density distribution, is one of the key spatial properties of a discrete fracture system. An improved understanding of all such spatial characteristics will ultimately allow us to better predict the mechanical behaviour, (e.g. Faulkner et al. 2008), directional permeability (e.g. Sigda et al. 1999, and network connectivity of rocks in subsurface environments (e.g. Dershowitz and Herda 1991). There are a large number of studies that have examined the scaling and spatial distribution of fault and fracture systems, but almost all have focussed on attributes such as size and density (e.g. Knott et al. 1996; Ouillon et al. 1996; Bonnet et al. 2001; Putz-Perrier and Sanderson 2008; Johansen and Fossen 2008). It is therefore somewhat surprising that the spatial variation of fracture orientations has received much less attention all the more so when well known geometric diversity and complexity of natural fracture systems is taken into account (e.g. Healy et al. 2006b,a; Twiss and Moores 2007; Tran 2007).

In this chapter, the spatial heterogeneity in the orientation and kinematics of secondary faults and fractures developed in Permian aeolian Yellow Sandstone is investigated in the damage zone of the hangingwall of the 90-Fathom Fault exposed at Cullercoats Bay, NE England. Statistical analytical techniques were applied to estimate the spatial variation and spatial correlation (spatial heterogeneity) of the fracture networks. The results reveal a systematic variation in complexity and kinematics apparently linked to the spatial location of fracture sets relative to the fault core. By contrast, no substantial spatial heterogeneity is recognised in directions oriented parallel to the fault strike. The study suggests that significant spatial heterogeneities in both fault orientation and kinematics are likely to occur adjacent to reactivated faults in transpressional/transtensional deformation zones. This has important implications in the prediction of secondary (sub-seismic scale) fault patterns in sub-surface reservoir rocks in oblique tectonic settings.

3.2 Geological background

3.2.1 Regional geological setting

The 90-Fathom Fault originally formed part of the southern margin of the Carboniferous Northumberland Basin (Fig. 3.1). Northern England at this time was characterized by the development of a system of fault-bounded deep basins and shallow marine shelves overlying structural highs, many of which were cored by relatively buoyant Caledonian granites (e.g. Guion et al. 2000, references therein). The ENE-WSW-trending Northumberland Basin had an asymmetric half-graben geometry and was bounded to the north by the Cheviot High and to the south by the generally ENE-WSW trending en echelon Stublick-90-Fathom Fault system (Collier, 1989; Kimbell et al., 1989), (Fig. 3.1). Thickness changes in the early Carboniferous strata are recorded across the fault system, with more than 4.2 km of Dinantian sedimentary rocks present in the hangingwall, compared to a few hundred metres overlying the Alston block, the structural high in the footwall (Kimbell et al., 1989). This is taken as evidence of syn-depositional fault activity (Kimbell et al., 1989). The early Carboniferous rifting is thought to have involved N-S-oriented extension that is believed to have ended during the Namurian and was followed by a thermal subsidence sag phase during the Westphalian, with thickening of the basin fill towards the basin centre (Kimbell et al., 1989). Both the Stublick and 90-Fathom faults offset Upper Carboniferous (Coal Measures) and overlying Permian strata suggesting that a period of faulting occurred in Permian to Mesozoic times and was likely associated with the early stages of rifting in the North Sea basin (Collier, 1989). Cross sections constructed from British Coal mine plans and borehole data suggest that Coal Measure strata are offset by 260 m, while the base of the Permian is estimated to exhibit 90 m of dip-slip normal displacement. The general lack of exposure and absence of high-quality sub-surface data means that the overall geometry of the major faults at depth is uncertain, especially in those segments reactivated during the post-Carboniferous (e.g. Kimbell et al. 1989; Leeder et al. 1989; Collier 1989).

3.2.2 Fracture deformation patterns

At Cullercoats the 90-Fathom Fault is an E-W striking normal fault, dipping to the north and juxtaposing a hanging-wall sequence of Permian aeolian sandstones and younger marine dolostones against a footwall of Carboniferous Coal Measures

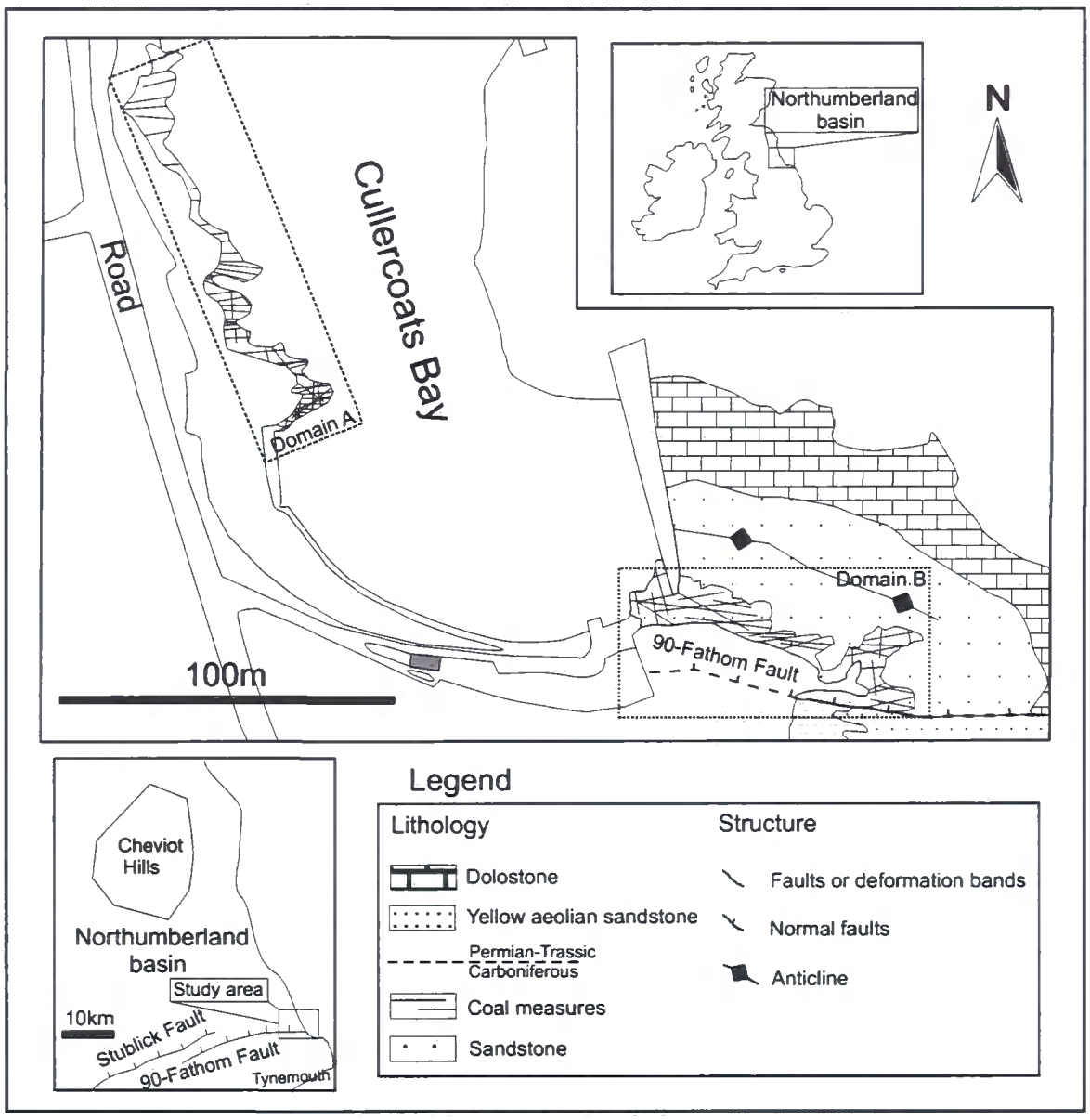

Figure 3.1: Map of the study area. The outcrop lies north of Tynemouth on the southern margin of the Northumberland Basin, defined by the Stublick-90-Fathom fault system. Boxes of dashed lines correspond to the two well exposed outcrops (named Domain A and B) in the immediate hanging-wall of the 90-Fathom Fault used to investigate the spatial heterogeneity of the fractures in N-S and E-W directions, respectively.

(Collier, 1989; De Paola et al., 2005a)). The sandstone developed local-sale cross-beddings and the dolomites developed regional-scale beddings, both of which are gently folded due to the hanging-wall deformation (Fig. 3.1). The fault core, where

most of the slip was accommodated is in sharp contact with the damage zone comprised of deformation band clusters and associated slip-surfaces in the hangingwall. In a detailed analysis of fracture geometries in the immediate hangingwall of the fault, De Paola et al. (2005a) demonstrated that the sharply-defined fractures in the dolostones are much simpler (conjugate, bimodal) compared to the linked, contemporaneous deformation bands developed in the sandstones (polymodal). They suggested that this occurred due to markedly different strain response during the same post-Carboniferous dextral transtension due to lithologically-controlled variations in the value of Poisson's ratio in the adjacent rock units. These authors also observed that the fractures/deformation bands in the sandstone comprised mutually cross-cutting dip-slip normal and dextral strike-slip faults.

In the sandstones, fractures in the form of deformation bands and deformation band clusters are well exposed in a 100 m long cliff (Figs. 3.1 3.2) trending approximately N-S (Domain A) and on the foreshore pavement and cliffs (Figs. 3.1 3.3) that run E-W roughly parallel to the strike of the 90-Fathom Fault (Domain B). The host sandstone preserves widespread cross-bedding at cm- to m-scales, is relatively porous and poorly cemented, and apart from a well developed mm- to cm-scale banding, is lithologically homogeneous. The rocks are cross cut by numerous deformation bands that are finer grained, better cemented, and have lower porosity (Fig. 3.2c-f). A few minor faults or fault splays relating to the main fault may exist in the center of the cliff section in that the fracture density is showing a bulk increase from north to south with some local fluctuations. Based on their similarity with other well-described deformation features in equivalent rock types, the faulting mechanism that generated these cataclastic deformation bands is likely to have involved strain-hardening and intense grain-size reduction along the localized brittle faults (e.g. Aydin 1978; Underhill and Woodcock 1987; Knott et al. 1996). Most of the deformation bands at Cullercoats Bay are classified as shear bands (Fossen et al., 2007) with small (mm- to tens of cm-scale) offsets of bedding developed(e.g. Fig. 3.2c).

The deformation band fractures in Domain A show an overall bimodal distribution with a larger spread of orientations in the southern part than in the northern part (Fig. 3.2a). In the northern part of the cliff section, the fractures, most of which are single deformation bands, typically display conjugate faulting patterns with one major set moderately dipping to the north and the other dipping to the south (Fig. 3.2a d). Traversing southwards into the damage zone where most fractures are in the form of deformation band clusters, the fracture density rises as noted by Knott et al. (1996) and a more complex anastomosing geometry becomes

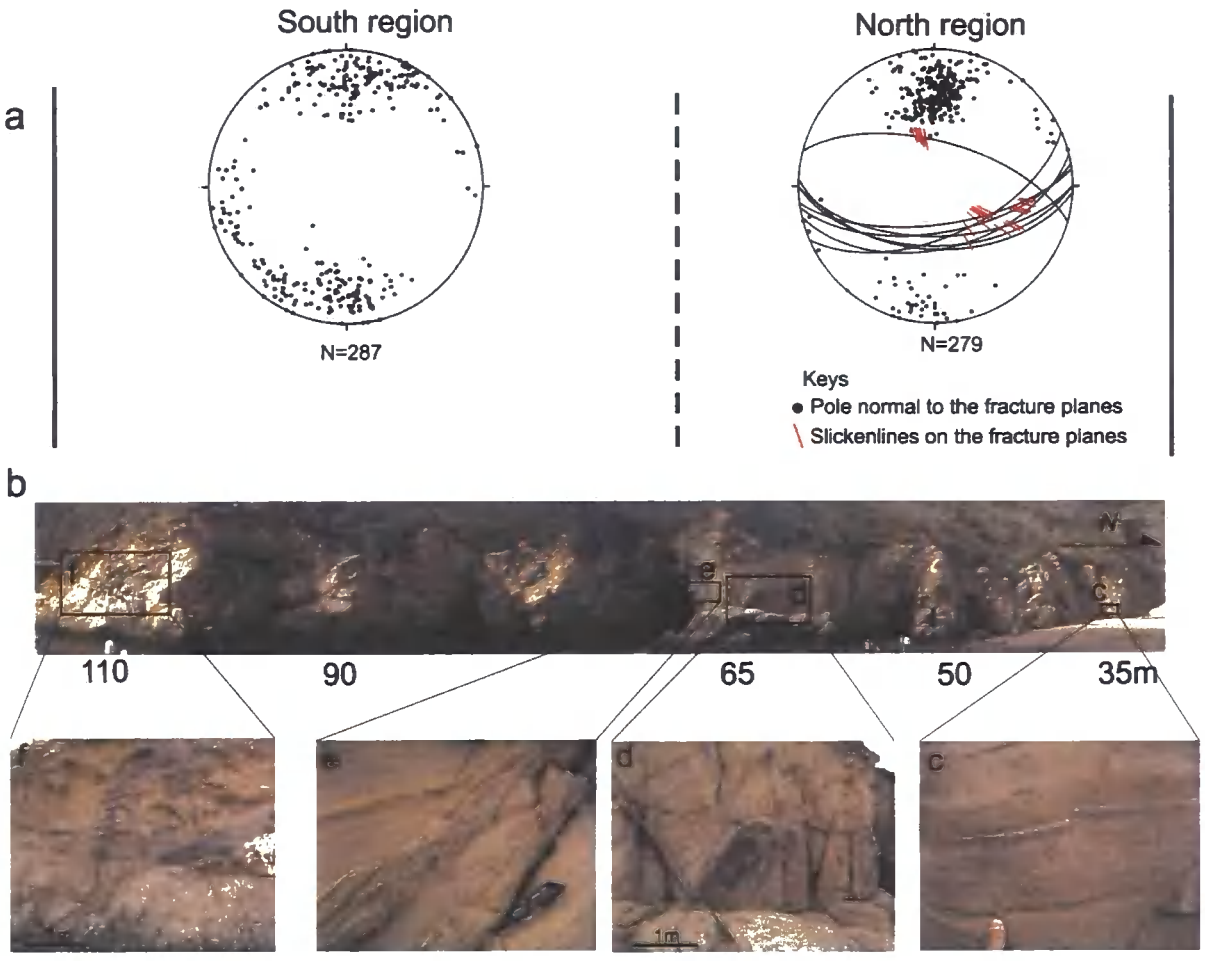

Figure 3.2: Outcrop overview of Domain A. (a) Stereoplots of data from the north and south regions of Domain A. (b) Photo of the cliff showing that the fracture pattern is conjugate in the north and changes to complex multiple orientations in the south. (c) A single shear band exposed in the northern end of the outcrop cliff, showing dip-slip displacement. (d) Conjugate deformation band clusters developing slip surfaces shown in (e). (f) Multiple sets of mutually cross-cutting deformation band clusters.

prevalent with multiple sets of fracture orientations striking approximately E-W and NW-SE exposed in the exposures forming the southern part of the cliff (Fig. 3.2a e f). Oblique dip-slip slickenlines are preserved on some of the fracture slip surfaces (Fig. 3.2a).

On the exposed pavement outcrop and cliffs of damage zone in Domain B, fracture sets trending ENE-WSW, ESE-WNW, and N-S can be easily distinguished both in the field and on the stereonet (Fig. 3.3). Traversing from west to east, the

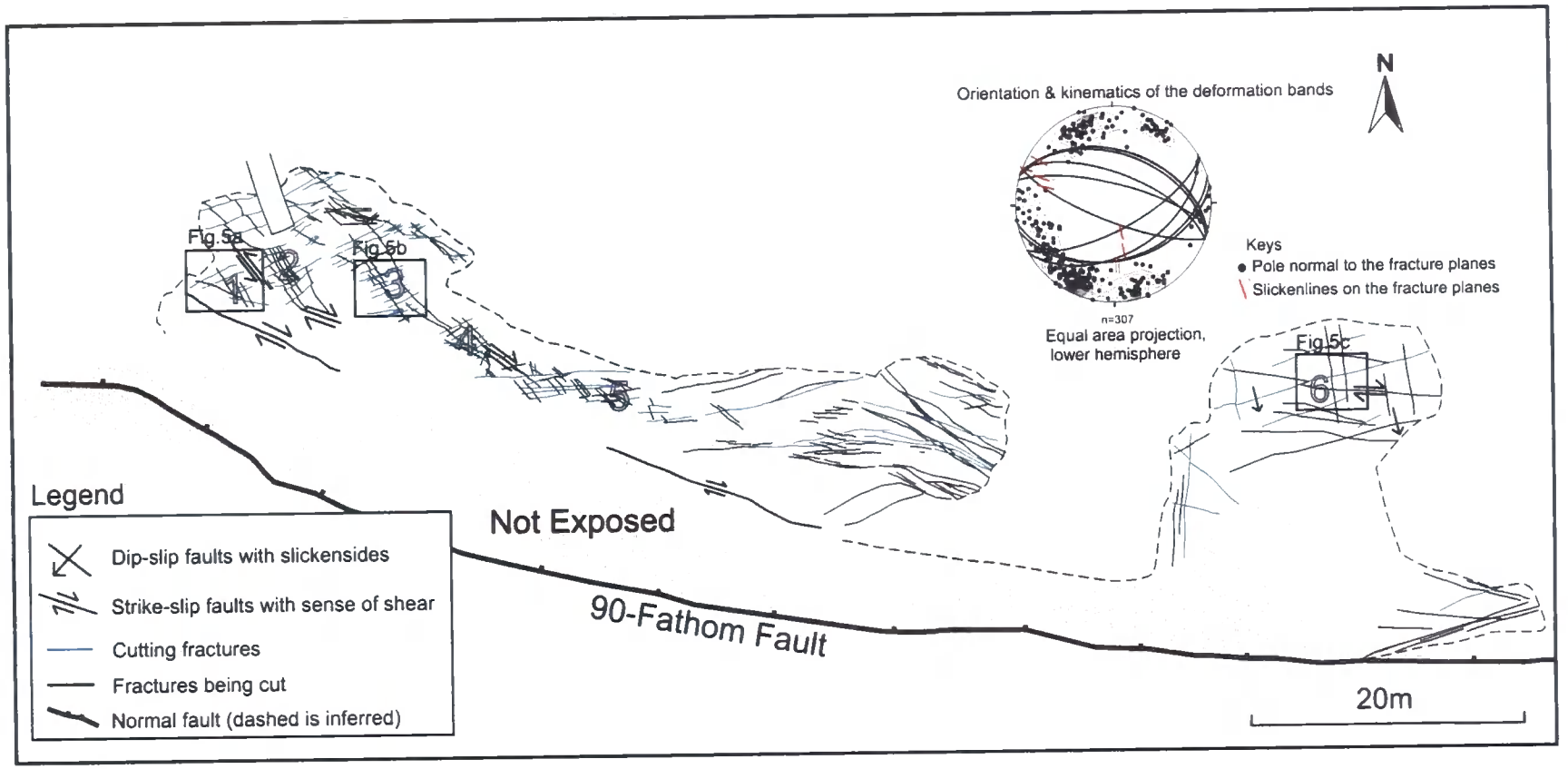

Figure 3.3: Detailed fracture map of the pavement in Domain B. Fractures cutting the others are coloured in blue. Numbers in grey colour on the map represent the sampling stations. Kinematic data show that the approximately ESE-WNW and N-S striking fractures bear conjugate strike-slip relation, whilst the ENE-WSW striking fractures (mostly in blue) exhibit dip-slip displacements. Stereoplots clearly show a bulk polymodal fracture orientation pattern.

Figure 3.4: Kinematics of distinct fault sets in Domain B. (a) A fault plane striking ESE-WNW showing dextral strike-slip displacement. (b) A fault plane striking SSE-NNW showing sinistral strike-slip displacement. (c) A fault plane striking ENE-WSW showing dip-slip displacement.

fracture density remains high and constant. Strains were partitioned into strike-slip and dip-slip displacements that were taken up along distinct fracture orientation sets (Fig. 3.3). The ESE-WNW fractures and a subordinate minor set of N-S striking fractures exhibit sub-horizontal slickenlines with dextral and sinistral displacements, respectively (Fig. 3.4a b). The predominant set of ENE-WSW striking fractures exhibit dip-slip slickenlines (Fig. 3.4c) and normal-sense offsets of bedding. The investigation of the fracture cross-cutting relationship shows that in the western part of Domain B, the ENE-WSW trending fractures offset the ESE-WNW trending strike-slip fractures (Fig. 3.5). This relationship becomes less obvious in the eastern part of the pavement outcrop where more ENE-WSW trending fractures are cut by other fracture sets (Figs. 3.3 3.5). Overall, they are mutually cross-cutting so that no fracture set is consistently younger than any other throughout the outcrop.

Compared with the deformation patterns observed in the Permian aeolian sandstones, faults in the adjacent units of Carboniferous sandstone are geometrically simple, predominantly E-W-trending structures that preserve dip-slip slickenlines in the foreshore footwall region of the 90-Fathom Fault. Collier (1989) ascribed the complex fracture pattern in the immediate hanging wall of the fault to the dextral oblique reactivation of the pre-existing E-W striking Dinantian normal fault at depth. De Paola et al. (2005a) have further suggested that the hangingwall sandstone deformation experienced a wrench-dominated transtension whose transport direction was oriented approximately NE-SW. The spatial heterogeneity of the fractures developed in the Permian aeolian sandstone is now discussed.

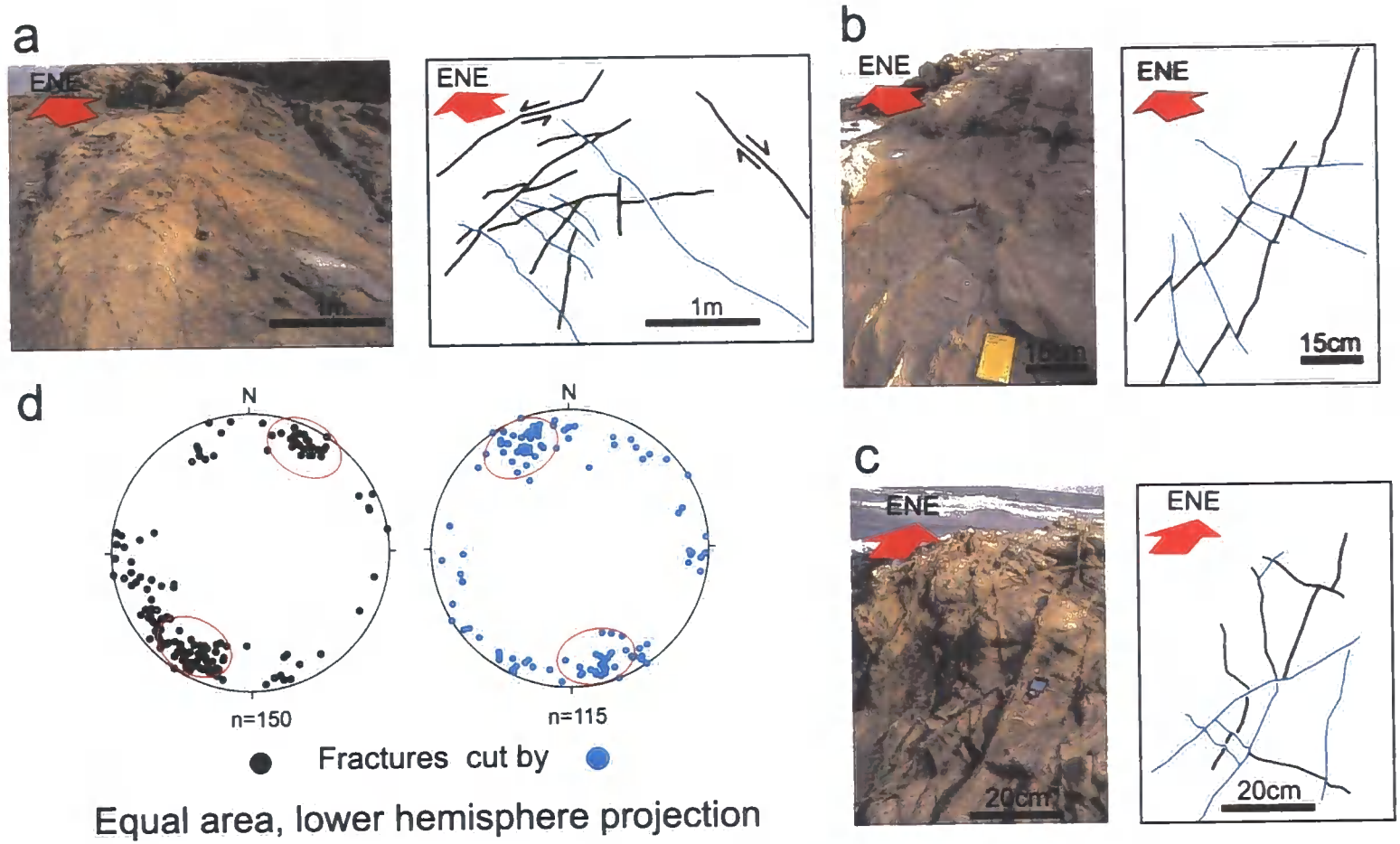

Figure 3.5: (a)-(c) Field photos of the fractures and sketches showing cross-cutting relationship: blue-coloured fractures are cutting the others in black. (d) Stereoplots illustrate that most blue-coloured fractures are striking ENE-WSW and most black-coloured fractures are striking ESE-WNW.

3.3 Methodology

Nearly 1000 fracture orientations and a few sparsely distributed slickenline data have been collected from the 100 m long N-S-trending cliff (Domain A) and 20 x 80 m cliff and pavement outcrop (Domain B) elongated in an E-W direction at Cullercoats Bay (Fig. 3.1). These two regions allow investigation of the spatial heterogeneity of fracture orientations in the hangingwall damage zone in directions trending approximately orthogonal and parallel to the strike of the 90-Fathom Fault.

3.3.1 Sampling strategy

Fracture orientation data were collected from north to south and east to west across the exposed cliffs and rock pavements in Domains A and B, respectively. An approximately 5 x 5 m moving sampling station was used to acquire sufficient numbers of measurements, with the spatial locations of the sampling window being systematically recorded as it moves across the outcrop (Fig. 3.6a b). The location of the window was defined by the distance from the northern end of the cliff in Domain A and western end of the outcrop in Domain B. Measurements from each sampling station are assigned the same spatial location as the station.

3.3.2 Spatial analysis

3.3.2.1 Spatial variation: bootstrapping in the moving window

Bootstrapping is a non-parametric approach used to estimate the distribution by randomly drawing a large number of samples of size n from the original sample (an approximation of the population) and calculating the associated value of a statistic without assuming the distribution model (Efron, 1982), (c.f. 1.1.2.6). In this study, this technique was combined with the moving average (Isaaks and Srivastava, 1989) in order to quantify any substantial variations that occur in the orientation datasets sampled across the exposures. The moving average is a smoothing operation which was originally used in analysing time-series data (Davis, 2002). In practice, however, the data structure does not have to be based on time, providing the measurements are arranged in a successive and systematic fashion, e.g. successive spatial locations arranged with a spacing significantly smaller than the total length of the sampling traverse. As the datasets were constructed by logging measurements from a sampling station that moves sequentially from the beginning to the end of the exposures, the order of the data therefore reflects the change in spatial location (Fig. 3.6a b). This

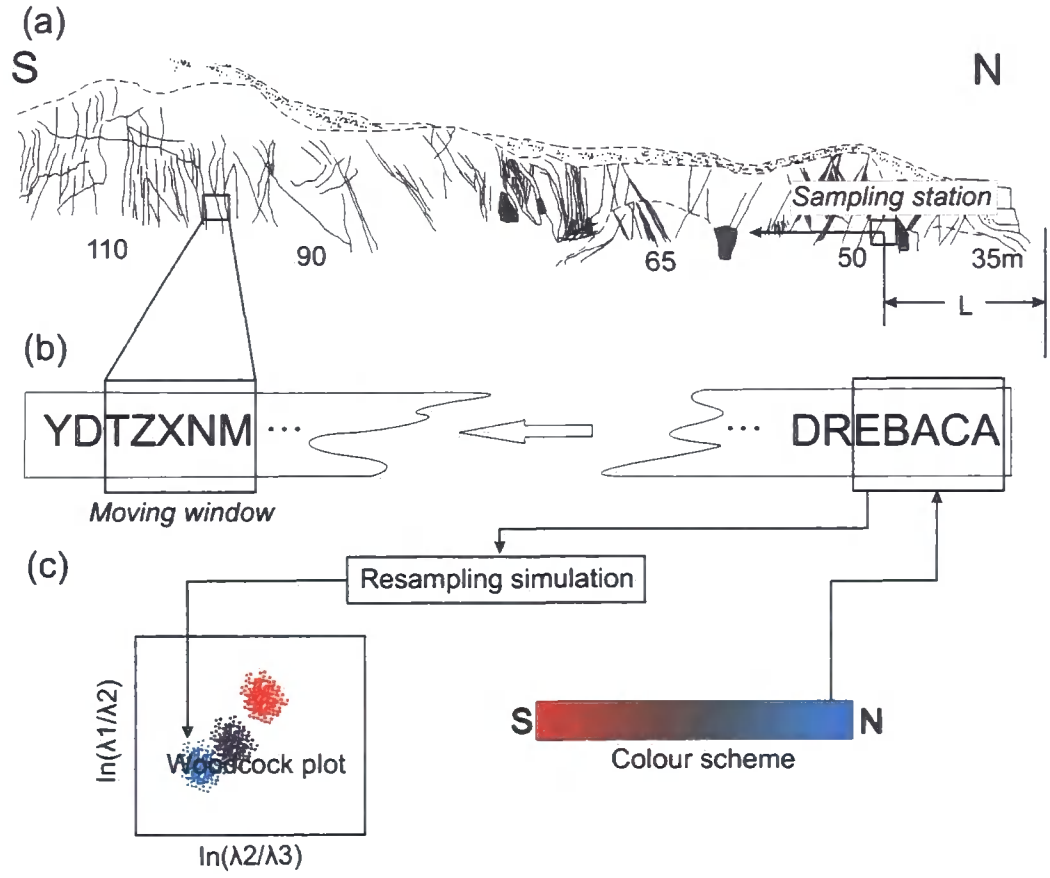

Figure 3.6: (a) Sketch of an outcrop from which fracture orientations were measured in an approximately 5 x 5 m moving sampling station whose spatial location is defined by 'L'. (b) Schematic diagram depicting the dataset structure: the orientation data A, B, C etc. was logged in sequence as the sampling station moves from the beginning to the end of the outcrop in (a). Moving window statistics were performed across the dataset to investigate the spatial heterogeneity in the sampling direction. (c) Bootstrapping in the moving windows with a colour scheme applied (see text for further details).

does not happen at scales less than 5m in the present study, since the size of the sampling station is 5 x 5 m.

To estimate substantial variations in the local dataset patterns, two approaches were used:

1. Bootstrapped means and associated standard errors of the eigenvalue ratios ($\ln(\lambda_1/\lambda_2)$, $\ln(\lambda_2/\lambda_3)$), (c.f. 1.1.2.3), where eigenvalues $\lambda_1 \geq \lambda_2 \geq \lambda_3$, are calculated directly from the sampling stations defined in the field (c.f. Mardia

et al. 1979; Woodcock and Naylor 1983).

2. Using a suitably sized moving 'window', a resampling simulation was performed on the sequentially arranged datasets to generate eigenvalue ratios that are pooled by location (Fig. 3.6b). This simulation is in some ways analogous to the moving sampling stations used in the field: we take fracture orientation samples with replacement in a window that moves across the datasets (Fig. 3.6b).

However, unlike in the field, the moving windows in this second approach have large overlaps. The 'size' of the moving window should not be too large - since this will smear out significant orientation variations - or too small as this will produce noisy fluctuations. The pooled ratios of eigenvalue $\ln(\lambda_1/\lambda_2)$ can be plotted against $\ln(\lambda_2/\lambda_3)$ on a so-called Woodcock diagram in order to investigate the clustering of the orientation data (Woodcock and Naylor, 1983).

To visualize the results, the bootstrapped $\ln(\lambda_1/\lambda_2)$ means were plotted against $\ln(\lambda_2/\lambda_3)$ means and error bars were calculated. For each bootstrapped mean, an integer number was allocated to indicate the relative spatial location of the sampling station along a traverse, e.g. in Domain A, integer number 1, 2, 3 etc. represents sampling stations located 5 m, 10 m and 15 m etc, from the northern end of the cliff (Fig. 3.6a). The schematic log shown in Fig. 3.6b illustrates that, from right to left, the data are arranged by the spatial location of the corresponding sampling stations where they were collected. For the simulated moving window approach, we chose a colour scheme (e.g. a colour bar changing from blue to red corresponding to the successive change of the spatial location) to colour-code the simulated ratios of the eigenvalues from a moving window. Pooled points (simulated ratios of the eigenvalues) from the same window are assigned the same colour and two spatially adjacent moving windows will have similar colours. If any substantial variations occur in the datasets, the visualized results will show systematic colour shifts associated with the location change (Fig. 3.6c). The point clouds coloured in blue on the Woodcock diagram indicate that the data are from the spatial location in the northern part of the cliff (Fig. 3.6b c). As the sampling station moves southwards, the estimated value shifts and turns red, suggesting that there is a relationship between the fracture pattern and spatial location (Fig. 3.6b c). The size of the moving window depends on the size of the data of each sampling station: if the moving window is too small, i.e. less than the data size of a sampling station, the results will show too much noisy fluctuation. A large moving window size, i.e. two or three times the average data size of a sampling station was found to better delineate the

data structure as it averages out the insignificant variations within and between the sampling stations.

3.3.2.2 Spatial correlation: variogram analysis

The spatial correlation of the fracture orientation data is quantified by the semivariance $\hat{\gamma}(h)$ or variance $\hat{Y}$(h) expressed by equation 2.1 or 1.6, respectively. As $\hat{\gamma}(h)$ and $\hat{Y}$(h) are , in essence, the same, variograms were created by plotting h against $\hat{Y}$(h) instead of using semivariograms in the h-$\hat{\gamma}(h)$ space. Fig. 3.7 depicts important features of the plots:

1. Range: as the lag h increases, the associated $\hat{Y}$(h) or $\hat{\gamma}(h)$ value will also increase until it flattens out. At this stage, any increase of the lag will no longer cause an increase in $\hat{Y}$(h) or $\hat{\gamma}(h)$ The threshold value of h at which $\hat{Y}$(h) or $\hat{\gamma}(h)$ reaches a 'plateau' is called the range.

2. The associated 'plateau' is called the sill. When the $\hat{Y}$(h) or $\hat{\gamma}(h)$ reaches the sill, no spatial correlation exists in the fracture orientation data.

3. Nugget effect: the jump from 0 for the value of $\hat{Y}$(h) or $\hat{\gamma}(h)$ at the origin of the variogram/semivariogram at extremely small lags is called the nugget effect (c.f. Isaaks and Srivastava 1989) and is thought to occur mainly due to multiple fracture sets (Fig. 3.7).

The range describes within what distance - or at what scales - the data have spatial correlation. When the data eventually lose this correlation, the sill estimates the average angular difference of the fracture orientations separated by distances larger than the range. By the contrast, within a very small distance close to 0, the nugget effect delineates the intrinsic angular difference of the fracture orientations. This can be caused by conjugate or polymodal faulting with wide spread of possible orientations. In addition, since the sampling error is normally much smaller than the angular difference caused by the presence of features such as conjugate fracture sets, it is likely that a vanished nugget effect indicates a unimodal fracture distribution with sampling errors.

3.4 Results

The 'moving window stereoplots' of the fracture data show an increase in the complexity of the orientation pattern from N to S in Domain A (Fig. 3.8) and a consistent polymodal orientation pattern in an W to E direction in Domain B (Fig. 3.9).

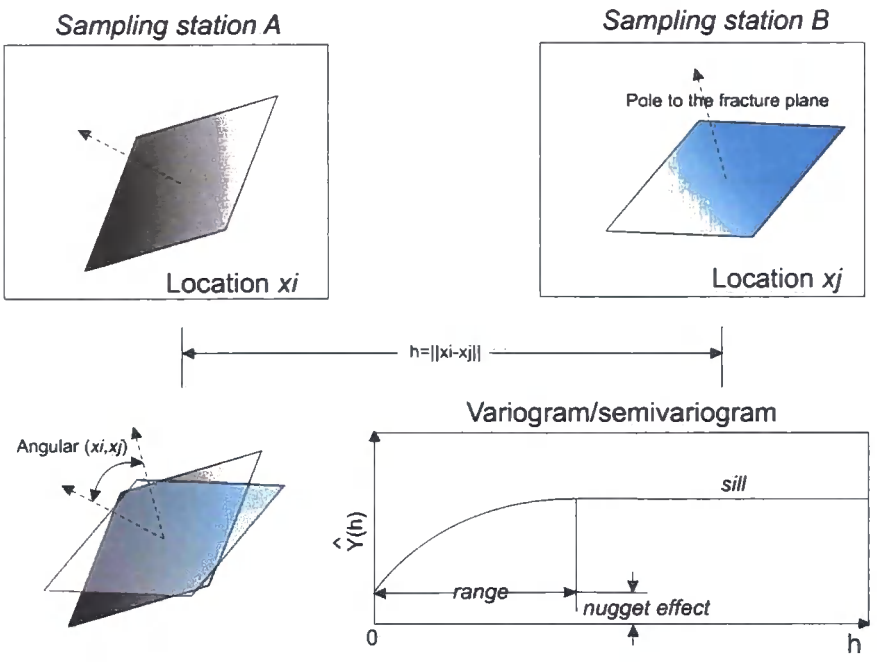

Figure 3.7: Schematic diagram of the variogram analysis of the fracture orientations. Any two fractures from the sampling station A and B are separated by distance h (lag). The quadratic mean of their acute angular difference was calculated and plotted against h to generate a variogram. The spatially correlated datasets have a variogram curve whose variance increases and flattens out as the lag h increases.

Bootstrapped mean ratios of the eigenvalues plotted on the Woodcock diagram show a bulk shift from a strong to a weak clustering from north to south in Domain A (Fig. 3.10a). The variations of this bootstrapped parameter in Domain A do not seem to be particularly systematic: from sampling station 1 (northern end of section) to 17 (southern end of the section) the degree of fracture orientation clustering does not show a consistent decrease. It is suggested that this results from a sampling bias inevitably introduced by the geometry and extent of the exposures available. In general the dimensions and preferred orientation of the rock outcrops will exert significant influence on the likelihood that particular fracture orientation will be well represented, i.e. fractures whose orientations lie subparallel to the outcrop faces will be less likely to be measured in sufficient numbers. In this study, it is suggested that the local irregularity of the cliff in Domain A has led to significant fluctuations in the bootstrapped mean ratios of the eigenvalues. Compared with the bootstrapped mean ratios of the eigenvalues, the results of the moving window simulation gave a reasonable consistent shift of the colours in Domain A, indicating a bulk decrease in

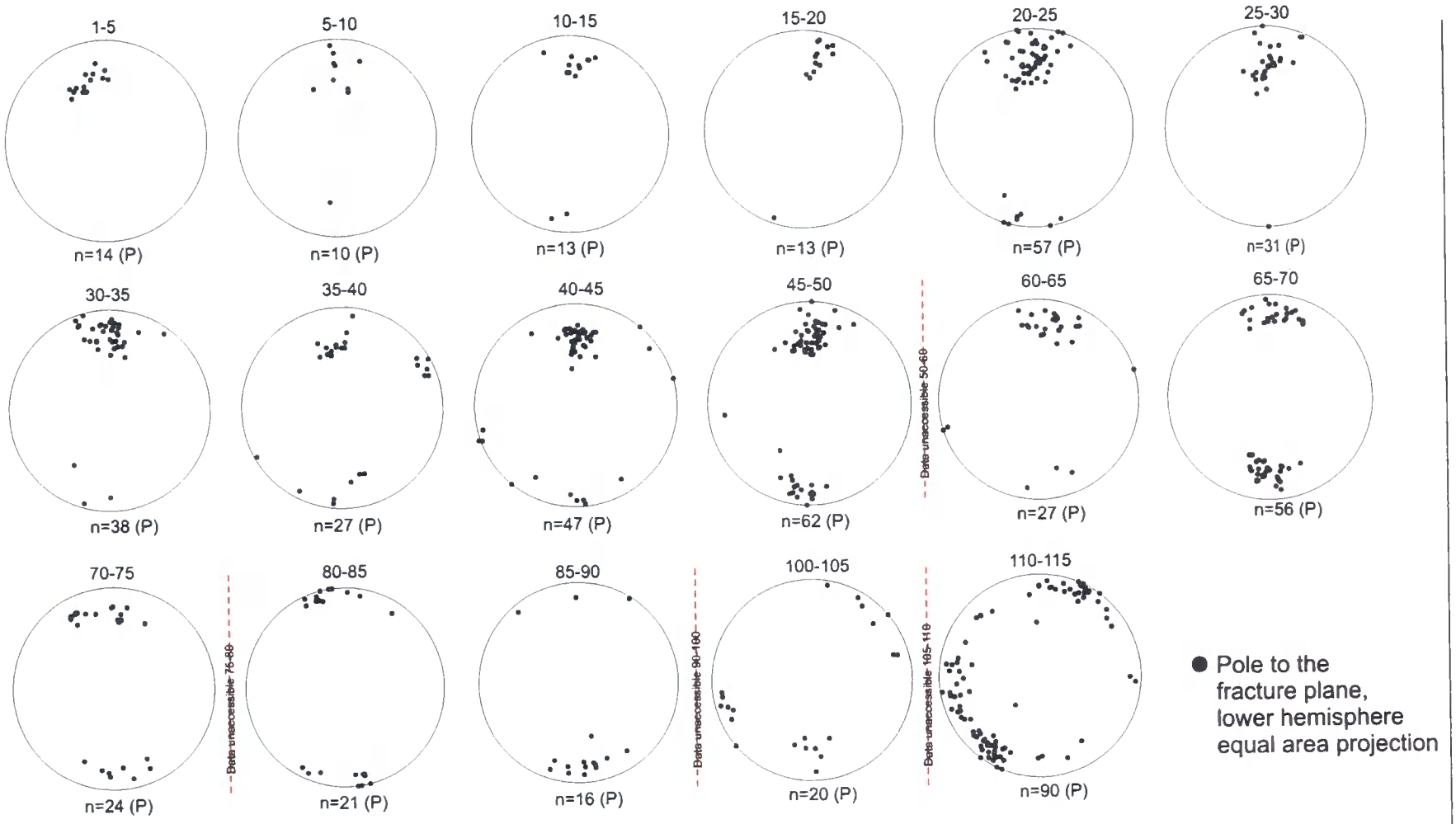

Figure 3.8: Stereoplots of the fracture orientations from Domain A. Numbers on top of each stereoplots e.g. 1-5, 5-10 indicate the relative spatial locations of the 5 x 5 m sampling stations where the data was collected. As the relative spatial location moves from north to south close to the 90-Fathom Fault, the fracture orientation pattern shows an increase in complexity.

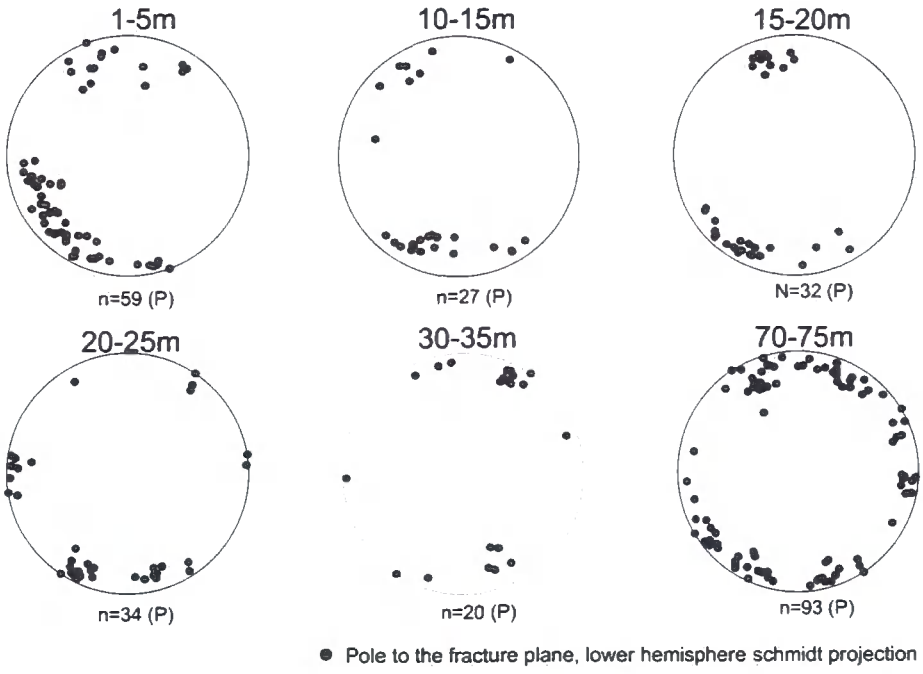

Figure 3.9: Stereoplots of the fracture orientations from Domain B. There are no substantial variations in the dataset in the direction parallel to the strike of the 90-Fathom Fault; the pattern stays consistent to the one from the southern end of the cliff (110-115m) (Fig. 3.9) in Domain A.

the degree of clustering of the fracture orientations moving from N to S (Fig. 3.10a b). In sharp contrast, in Domain B, there is no substantial trend in the degree of clustering moving from W to E (Fig. 3.10a b).

There is a strong correlation between the variance $\hat{Y}(h)$ and the lag (separation) distance h in the N-S direction along the cliff in Domain A revealed by the variogram (Fig. 3.10b c). The nugget effect is 40^o, i.e. the variance in orientation of very closely separated fractures. As the lag distance h increases, the variance increases correspondingly through the whole range of the cliff length (Fig. 3.10c). The range and sill in Domain A is therefore, probably larger than 100 m and 60^o, respectively. By contrast, in Domain B, along the strike of the 90-Fathom Fault (Fig. 3.10b), no substantial correlation exists between variance $\hat{Y}(h)$ and the separating distance h. Here, the variogram levels out at a variance of 50^o along the entire section (Fig. 3.10c). This suggests that in the traverse parallel to the 90-Fathom Fault, the fracture orientations are independent to each other with the average angular difference 50^o (quadratic mean).

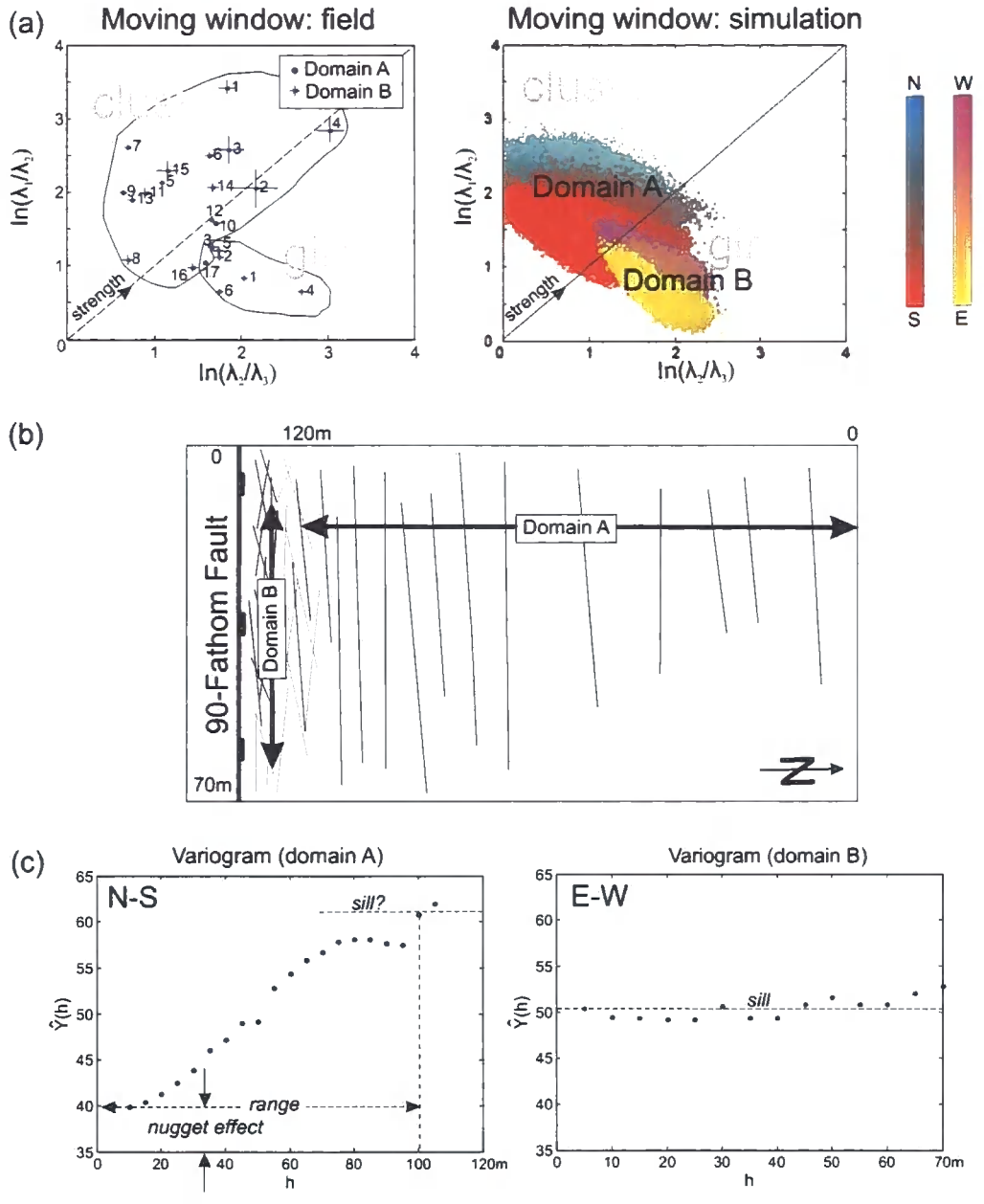

Figure 3.10: (a) Bootstrapped eigenvalue ratios of $\ln(\lambda_1/\lambda_2)$ & $\ln(\lambda_2/\lambda_3)$ (λ_i i=1, 2, 3 are the eigenvalues of the fracture orientations, $\lambda_1 \leq \lambda_2 \leq \lambda_3$) indicating that the bulk fracture orientation pattern changes from cluster to girdle as the spatial location of the fractures moves approximately N-S in the direction orthogonal to the 90-Fathom Fault strike (Domain A) and the orientation pattern does not change substantially W-E in the direction parallel to the 90-Fathom Fault strike (Domain B). (b) Schematic diagram showing the directional spatial heterogeneity displayed by the fracture networks in Domain A and Domain B, respectively. (c) Variograms showing strong spatial correlation of the fracture orientation in Domain A and no substantial spatial correlation in Domain B.

3.5 Discussion

Many features of the secondary structures have been demonstrated to change progressively inward towards the fault core in fault damage zones (e.g. Chester et al. 1993; Knott et al. 1996; Shipton and Cowie 2001; Johansen and Fossen 2008). In this case study, Domain A exhibits a substantial change of the fracture orientation patterns and kinematics from outer zone (less deformed) to inner zone (highly deformed) and Domain B reveals more details of the fracture geometry and kinematics as well as the spatial characteristics in the damage zone around the fault core. Our investigation of fractures in the damage zone suggests that there is an increase in the degree of complexity and intensity of the local strains due to the pre-existing master fault control.

3.5.1 The spatial heterogeneity of fracture orientations in damage zones

The fracture orientation patterns studied here reveal a strong and systematic spatial heterogeneity in a direction orthogonal to the strike of the 90-Fathom Fault. It is well known that for many damage zones, there is an overall increase in the strain magnitude and fracture density towards the fault core (c.f. Kim et al. 2004; Caine et al. 1996). Our results show that the spatial heterogeneity of the fractures changes also in terms of fracture plane orientations and kinematics. Changes in orientation have been observed in many natural systems as one passes from the wall rocks into the damage zones of larger faults (e.g. Faulkner et al. 2006). However, it seems that the fracture systems do not simply rotate as they change orientation — they also change in terms of their complexity. Thus, in the case of the 90-Fathom Fault, the fracture orientation patterns follow a bimodal conjugate fault model at locations more than 100 m from the main fault slip plane. At distances less than 100m, the fractures display a polymodal pattern which has orthorhombic or triclinic symmetry with one or two sets dominant. This change is thought to reflect a partitioning of transtensional 3D non-coaxial deformation (De Paola et al., 2005a).

The change in the orientation pattern is effectively quantified by the bootstrap methods. By contrast, the results from the Appleby case study (c.f 2) show that the model of fracture orientations from the damage zone simply rotates without becoming complex (c.f. 2.4) as approaching the fault core. Two end-member types of spatial variation are therefore tentatively proposed:

1. Model A: spatial variations occur due to changes in the orientation pattern (i.e. bimodal to polymodal) whilst the overall transport vector means remains stable (this case study), (Fig. 3.11a).

2. Model B: spatial variations occur due to rotations of the overall transport vector (or 'stress field') with changing spatial location whilst the orientation pattern remains relatively consistent (Fig. 3.11b), (c.f. 2).

The spatial variations in Model A will be identifiable using the Woodcock and Naylor (1983) plots and the bootstrapped eigenvalue ratios $\ln(\lambda_1/\lambda_2)/\ \ln(\lambda_2/\lambda_3)$ (Fig. 3.11a)), but this method is not effective to identify Model B. Instead, in those cases, one should use the bootstrapped estimation to examine the orientation model for each fracture set that undergoes rotation from location to location in the fault zone (Fig. 3.11c).

A simultaneous problem raised here is how to find an effective way to define and track the evolution of clusters in the fracture orientation data. For ideally unimodal or bimodal distributions, the simplest approach is to analyze each cluster separately, but it is not easy to apply the same approach to polymodal or girdle distributed orientation data as a standard definition of clusters does not exist. This illustrates a common problem encountered in the geostatistical analysis of natural datasets: that particular methods associated with a criterion are not always consistent with the underlying data structure (Ye and Rabiller, 2000). In fact, fracture orientations from most natural fault zones can be broadly classified into bulk unimodal/bimodal distribution catalogue even in cases where the actual applied strain was 3D. This occurs because natural variations in fracture orientation — possibly introduced during fracture nucleation and growth (see Healy et al. 2006b for example) — often obscure more complex clustering patterns at different scales. At larger scales, the fracture orientation could show a bulk bimodal distribution whereas when zoom in, complex multiple fracture patterns begin to emerge (c.f. 2 Appleby case study). Alternatively, fracture sets are often manually grouped into different sets based on certain geological criteria, e.g. lithology, fracture type etc. (e.g. Gross 1995; Holdsworth et al. 2002; Schopfer et al. 2006). From north to south along the cliff in the traverse orthogonal to the 90-Fathom Fault, the fracture orientations do not show a consistent rotation of the bootstrapped vector means (Fig. 3.12), indicating that this case study is more akin to Model A. Our results further suggest that if the results of bootstrapping the fracture eigenvalues by using moving windows do not show any

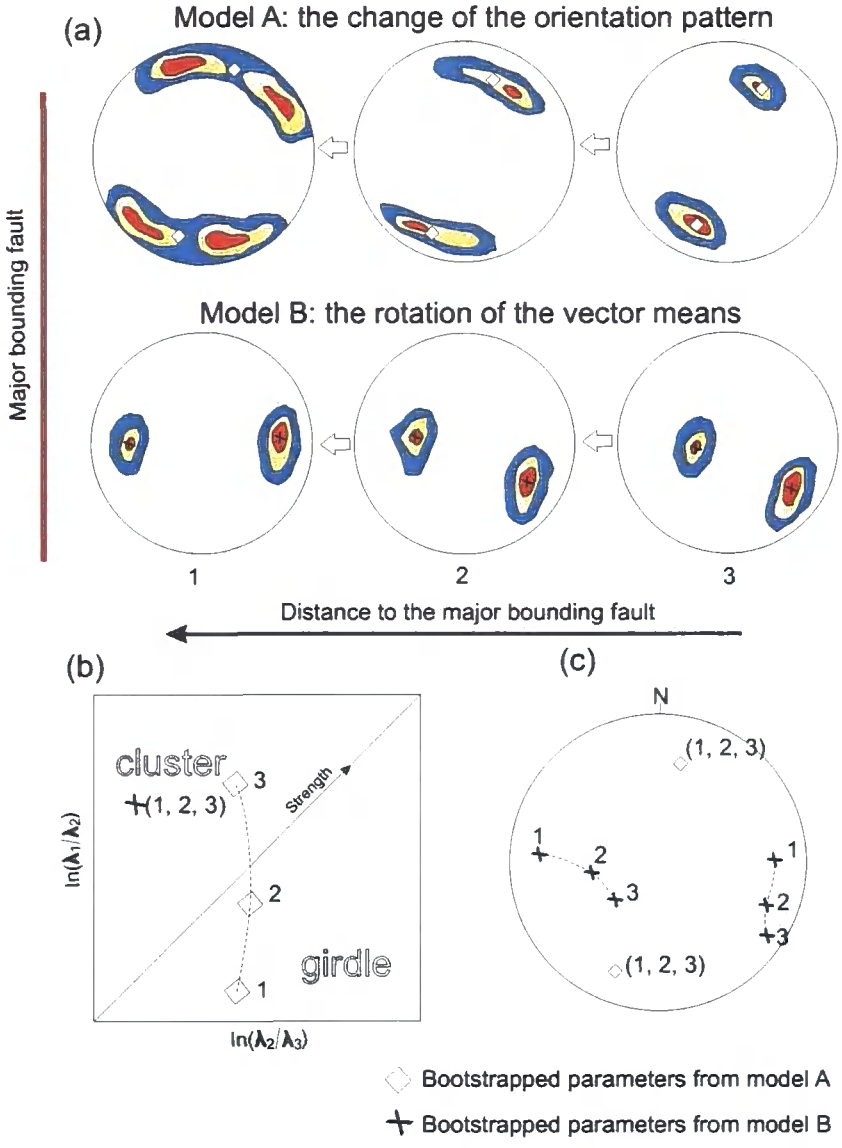

Figure 3.11: (a) Schematic diagram of two types of spatial variations in the orientation patterns. As the sampling station moves close to the fault zone centre, the fracture orientation pattern can change without substantially changing the mean orientations (model A) or the mean fracture orientations rotate without substantially changing the orientation patterns (model B). (b) Schematic diagram illustrating that bootstrapped eigenvalue ratios of model A-type spatial variation will exhibit obvious shifts on the Woodcock diagram. (c) Schematic diagram illustrating that the bootstrapped vector means of model B type spatial variation will show an obvious shift on the stereoplots.

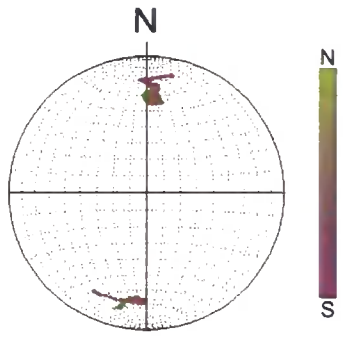

Figure 3.12: Bootstrapped means in the moving window: the bootstrapped mean in each window is relatively stable from north to south of the outcrop cliff in Domain A.

substantial variations across fault zones, the variations most likely indicate a simple fracture rotation scenario (Model B) rather a change of the orientation pattern (Model A) (Fig. 3.11b c) and vice versa.

Another characteristic feature of the spatial heterogeneity is the spatial correlation defined by the quadratic mean of the orientation difference of any two spatially separated fractures. The measure of this spatial dissimilarity/similarity by variogram/semivariogram analysis is not based on an assumption of a certain distribution model that fracture orientations must follow. This is important since studies of natural fracture patterns in obliquely divergent/convergent settings generally seems to result in a level of complexity that cannot be thoroughly and accurately described by simple unimodal/bimodal distributions (e.g. see examples in Dewey et al. 1998; Dewey 2002; De Paola et al. 2005b; Clifton and Kattenhorn 2006; Taylor et al. 2008). Variogram/semivariogram analyses are potentially a robust technique that may be used to delineate spatial correlations in fracture orientations which may have a very 'fuzzy' bimodal distribution or polymodal distribution. Compared with stereoplots and bootstrapping the eigenvalues, variograms can accurately describe the similarity/dissimilarity trends of fracture orientations separated by increasing lag h.

3.5.2 Kinematic relationships between the multiple fault sets

In the damage zone of Domain B near the fault core, the strains were clearly partitioned into simple shear and pure shear accommodated by distinct fracture ori-

entations: ESE-WNW (dextral) and N-S trending (sinistral) faults/fractures took up the strike-slip component of the bulk strain; ENE-WSW trending fractures took up the dip-slip extensional component of the bulk strain. By contrast, kinematics in domain A show oblique-slip displacement indicating a decrease in the degree of strain partitioning possibly as this region lies sufficiently far away from the influence of the main pre-existing boundary fault (Fig. 3.2). Previous studies suggest that strain partition is actually taken up progressively during transpression/transtension (c.f. Withjack and Jamison 1986; Tikoff and Teyssier 1994). Particularly in Domain B where strains were highly heterogeneous, the main boundary fault was first reactivated to accommodate pure shear component of the bulk strain, followed by invoking the conjugate strike-slip faults (ESE-WNW and N-S trending) in the hangingwall aeolian sandstone. The residual strain was subsequentially accommodated by ENE-WSW trending normal faults. Moving north away from the main fault, the kinematics of the originally distinct fault sets close to the fault core become oblique dip-slip and the fracture orientation pattern tends to be simpler (Fig. 3.2).

The dominance of non-coaxial versus coaxial strain component is not only determined by the angle between the zone boundary and the transport direction but also by the host rock lithology (McCoss, 1986; Tikoff and Teyssier, 1994; De Paola et al., 2005a). In a progressive change from a wrench-dominated to an extension-dominated strain regime one would expect the extensional faults to consistently cross-cut the strike-slip faults because they are the product of the final strain (De Paola et al., 2005a). This feature does exist in the west part of Domain B (Figs. 3.3 3.5a b). However, the 'swap-over' of the cross-cutting relationship in the east part of the pavement outcrop suggests that the fracture sets of distinct kinematics are broadly contemporaneous (Figs. 3.3 3.5 c). It is proposed that the actual behaviour of rock in transtensional strain regimes is not easy to predict and the strain patterns are further complicated by the variations of the pre-existing structures or weakness (Taylor et al., 2008) and the influence of the geofluids (Chester et al., 1993). This study supports the general case that complex patterns of simultaneously initiated normal and wrench fault arrays are likely to characterize most transpressional/transtensional fault zones (De Paola et al., 2005a; Lewis, 2007; Taylor et al., 2008).

3.5.3 Factors controlling fracture patterns

Concerning the orientation of the fractures in fault damage zones, many factors are supposed to influence the fracture pattern. The investigation present here has clearly demonstrated that such geometric and spatial heterogeneity in fracture orientations

is highly related to the major fault control. The bulk lithology determines how the wall rock responds to the regional displacement and may produce different strain patterns (c.f. De Paola et al. 2005a). But this could also be substantially affected by mechanical weakening zones such as beddings: the dolomites exposed in Cullercoats exhibit regional beddings of tens of centimeters thick, whilst the underlying aeolian sandstone has local cross-beddings. No obvious slips of the beddings in the sandstone suggest that the strain was simply accommodated by fracturing. For the dolomites, regional beddings may serve as mechanical weakness that accommodates part of the strain and leaves the rest accommodated by fractures of simpler patterns.

Fractures in porous and poorly cemented granular rocks may develop in order to accommodate the geometrically-necessary strains (e.g. reverse drag folds) in the wall rocks adjacent to normal faults (e.g. Shipton and Cowie 2001). The fold in the immediate hanging-wall of the 90 Fathom Fault appears to have a greater amplitude than is typically associated with the reverse drag folding. Folding within the hanging-wall of the 90 Fathom Fault - in addition to slip on the fault itself - may therefore influence fracturing and hence affect the geometric and spatial distribution of the fractures (c.f. Collier 1989).

The density of the fractures in the form of deformation bands or clusters is somehow unevenly distributed throughout the damage zone, although there is a bulk increase in a direction orthogonal to the main fault trace. This may be the results of hanging-wall faulting associated with the 90-Fathom Fault or simply the initiation of slip surfaces due to the maturity of the deformation band clusters (Aydin, 1978). At meter scale of observations, these minor faults or fault splays will inevitably affect the distribution pattern of the fractures. The sudden 'jump' of the fracture orientation pattern changing from 'bimodal' to 'polymodal' within meters in the center of the cliff possibly reflects such minor faults control inferred by the increase of the fracture density (Fig. 3.8). Nevertheless, the overall trend of the fracture orientation pattern becomes more complicated as approaching the fault core.

3.6 Conclusions

The complex fracture patterns exposed in the Permian Yellow aeolian sandstones in the damage zone in the hangingwall of the 90-Fathom Fault at Cullercoats have a characteristic spatial heterogeneity in terms of their fracture orientation patterns. In particular:

1. The orientation pattern changes from simple bimodal conjugate faulting far away from the 90-Fathom Fault to complex polymodal faulting in the 100 m nearest to the 90-Fathom Fault; no substantial variations in the orientation pattern occur in an along-strike direction along the 90-Fathom Fault.

2. Fracture orientations are spatially correlated in a direction orthogonal to the strike of the 90-Fathom Fault at scales larger than 100m; no substantial spatial correlations of the fracture orientations occur in the direction parallel to the strike of the 90-Fathom Fault.

3. The bulk strain, which initiated due to the oblique reactivation of the 90-Fathom Fault experienced partitioning into strike-slip and dip-slip displacements along differently oriented fracture sets in the region of complex fractures close to the 90-Fathom Fault.

The results imply that pre-existing structures lying obliquely to the renewed bulk strain will exert a substantial influence on later formed damage zones in which fracture orientations, kinematics and geometric relationships will vary in response to the distance from the fault core. Hence, by investigating local scale structures in a spatially constrained context, we may be able to predict possible fluid flow paths affected by spatially heterogeneous fracture networks in the fault controlled aquifers or hydrocarbon reservoirs.

Chapter 4

Deformation patterns in heterogeneous sandstone sequence

The characterization of spatial heterogeneity in fracture networks is important in predicting fluid flow in the earth's subsurface. Many previous studies have focused on determining scaling laws for fracture attributes such as length and spacing etc. However, fracture orientation, a fundamental geometric characteristic has received relatively little attention and there are few techniques that currently exist in order to analyse spatial heterogeneity in orientation datasets. In this chapter, the spatial analysis is adopted to quantify fracture orientation data collected in the outer zone of an extensional fault damage zone exposed in Mesozoic conglomerates and pebbly sandstones at Laide, NW Scotland. The results suggest that lithology affects fracture orientation at both centimetre and meter scales. Mm- to cm-scale heterogeneities such as pebble lithology and pebble shape do not exert substantial influences on the bulk orientation of fractures in the pebbles, but give a certain degree of control on the spatial correlation and orientation patterns within individual pebbles. The findings imply that fracture orientation patterns in fault zones developed during crustal extension are likely to vary at different scales and locations due to lithological controls operating at various scales in addition to any influences exerted by larger-scale faults.

4.1 Introduction

The development of an improved understanding the spatial attributes of natural fracture system has been an active field of research over the last 25 years (e.g. Aydin and Reches 1982; Gillespie et al. 1993; Knott et al. 1996; Bonnet et al. 2001;

Tran 2007). A number of strategies and methodologies in sampling and data analysis, such as scan-line sampling schemes, box-counting methods, fractal geometry analysis, eigenvalue analysis, and multidimensional fracture density measures etc., have been derived from other disciplines (mathematics and physics in particular) and used to quantify fracture geometry and spatial variations associated with scale and spatial location (c.f. Mandelbrot 1982; Woodcock and Naylor 1983; Dershowitz and Herda 1991; Gillespie et al. 1993; Mauldon et al. 2001). These techniques have demonstrated that the natural fracture networks are heterogeneous at different scales. In many fault zones, these studies have shown that there is a rotation of the stress field leading to variations in the secondary fault density and displacement patterns in the traverse directions orthogonal to the fault trace, suggesting that the master faults control the bulk strain distribution (e.g. Wojtal 1989; Peacock 1991; Knott 1994; Knott et al. 1996; Hardebeck and Hauksson 1999; Wilson et al. 2003; Faulkner et al. 2006). Field studies and laboratory experiments suggest that many other factors also control the spatial characteristics of the fractures such as lithological heterogeneity, pre-existing structures and contrasts in the rheological behaviour of materials (e.g. McEwen 1981; Gross 1995; Lin et al. 1998; Mandal et al. 2001; De Paola et al. 2005a,b; Schopfer et al. 2006; Putz-Perrier and Sanderson 2008). Yet the spatial heterogeneity of fracture orientation data from natural fault zones has not been characterized very well (Tran, 2007). Methodology developed in the thesis (c.f. 1 2) is applied to investigate the spatial heterogeneity in fracture orientations from a Mesozoic sequence of conglomerates and pebbly sandstones exposed at Laide, NW Scotland. The findings support the results of previous studies (e.g. McEwen 1981; Gross 1995; Faulkner et al. 2006) that local strains generally vary with their proximity to master faults and changes in the host rock lithology.

4.2 Geological background

Widespread accumulations of Mesozoic sedimentary rocks occur in offshore basins located around the NW Scottish mainland, but relatively few outcrops are preserved onshore due to the effects of later Palaeogene regional uplift (Roberts and Holdsworth, 1999). The Precambrian basement underlying the Mesozoic sediments of NW Scotland offshore and exposed onshore has suffered a long and complex history of deformation and reactivation from the Archaean to the present day (e.g. Beacom et al. 2001; Park et al. 2002). The Caledonian foreland, located west of the Moine Thrust in the extreme NW of Scotland, exposes the Lewisian Complex which

comprises Archaean to Proterozoic crystalline, mainly gneissose rocks. These form a broad coastal strip running from Cape Wrath in the north to Loch Torridon in the south (Park et al., 2002). In Gruinard Bay, the Lewisian rocks consist of mafic and acid gneisses that preserve some of the oldest ages (2730Ma) in NW Scotland (Davis, 1977; Corfu et al., 1998). The unconformably overlying Torridon Group sandstones are fluviatile red-bed deposits of Neoproterzoic age (Stewart, 1982, 1991, 1993), which in the area of Gruinard Bay comprise basal conglomerates and coarse grained sandstones with syn-sedimentary folds and numerous later systems of anastomosing fractures (Beacom, 1999).

The New Red Sandstone in the Laide area forms a fault-bounded strip of sedimentary rocks trending NE-SW (Fig. 4.1). It consists of a thin basal breccia overlain by ca. 100 m of thinly-interbedded, purple, pebbly sandstones and conglomerates; deposits that were derived from local uplands, and laid down in alluvial fans (Johnstone and Mykura, 1989). This onshore outlier of Mesozoic sedimentary rocks is the correlative of much thicker sequences deposited in the adjacent Minch Basin offshore and immediately to the west. The onshore sequence at Laide is cut by a series of NNE-trending normal faults which have a similar trend to regional scale normal faults that define the Minch Basin offshore. Some previous, regional-scale studies (e.g. Brewer and Smythe 1984; Stein 1988) have suggested that the location of these normal faults may be controlled by the reactivation of the pre-existing Outer Hebrides Fault Zone which was active as a thrust during the Caledonian orogeny. However, there is little evidence to support this hypothesis and invoking basement reactivation may be simply unnecessary (Roberts and Holdsworth, 1999). Beacom (1999) has shown that the timing of multiple faulting and reactivation events preserved in the underlying Lewisian basement and Torridonian sedimentary rocks at Laide is poorly unconstrained. By contrast, the Mesozoic sediments are only affected by one Mesozoic or Cenozoic episode of extensional faulting.

The outcrop examined in detail during the present study at Laide forms an approximately 70 x 30 m pavement located 60 m south of Am Fiachaclan where a major NNE-SSW trending fault downthrows New Red Sandstone in the hanging-wall to the south against a footwall sequence of Torridonian sandstone to the north (Fig. 4.2). Two main conglomerate units are exposed north and south of the jetty, in regions referred to here as locality 1 and locality 2, respectively (Figs. 4.2 4.3). The pebbles exposed in the conglomerates are typically ellipsoidal in shape with their long axes orientated perpendicular to the fault traces whilst their short axes are sub-vertical (Fig. 4.4a b). There are two dominant pebble lithologies in this area:

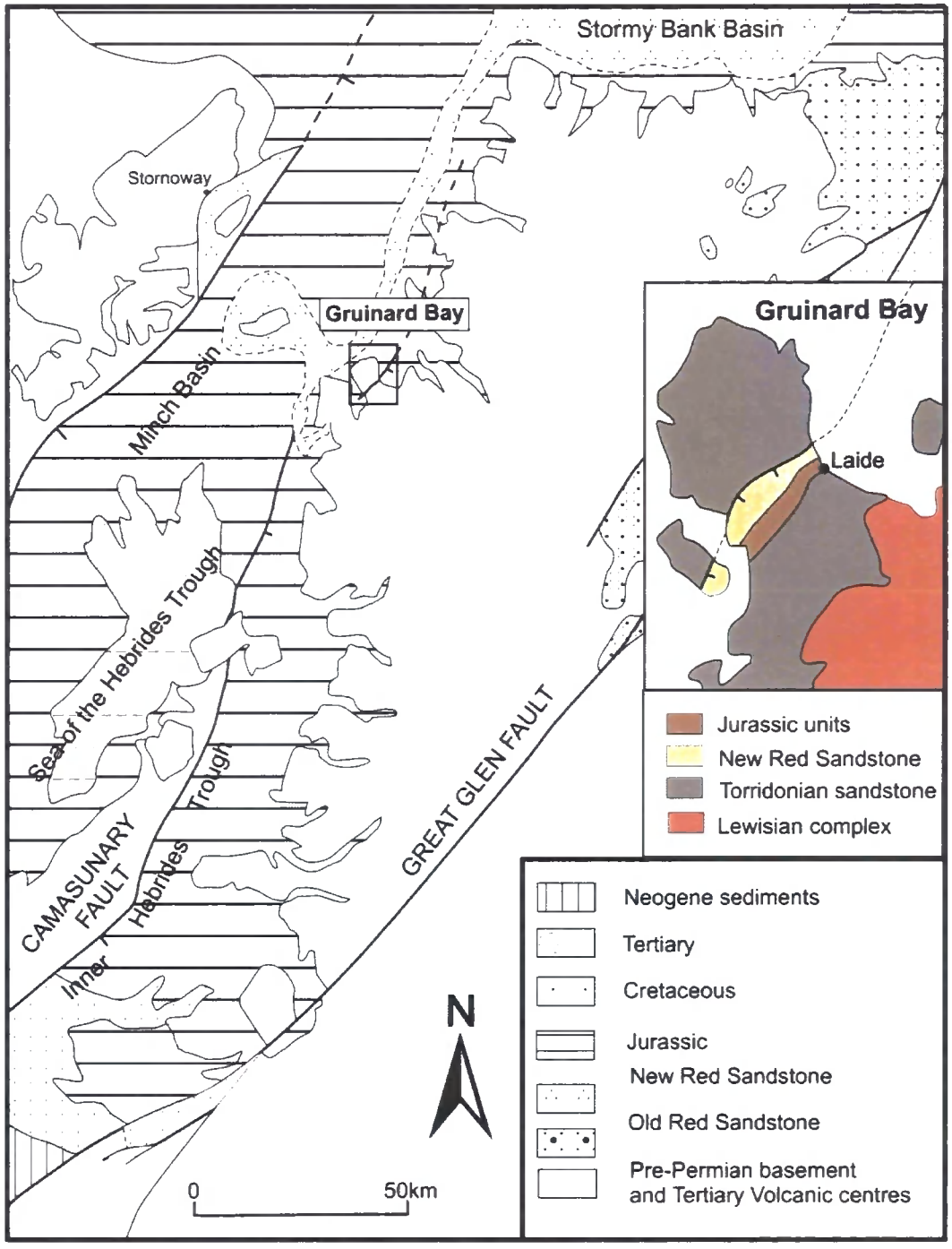

Figure 4.1: Geological map of the NW Highlands of Scotland showing the location of major Mesozoic basins and the NNE-SSW trending normal faults that bound the Minch Basin. The location of Laide, Gruinard Bay, lying close to the eastern margin of the Minch Basin is also shown (after Johnstone and Mykura 1989; Lovell 1991).

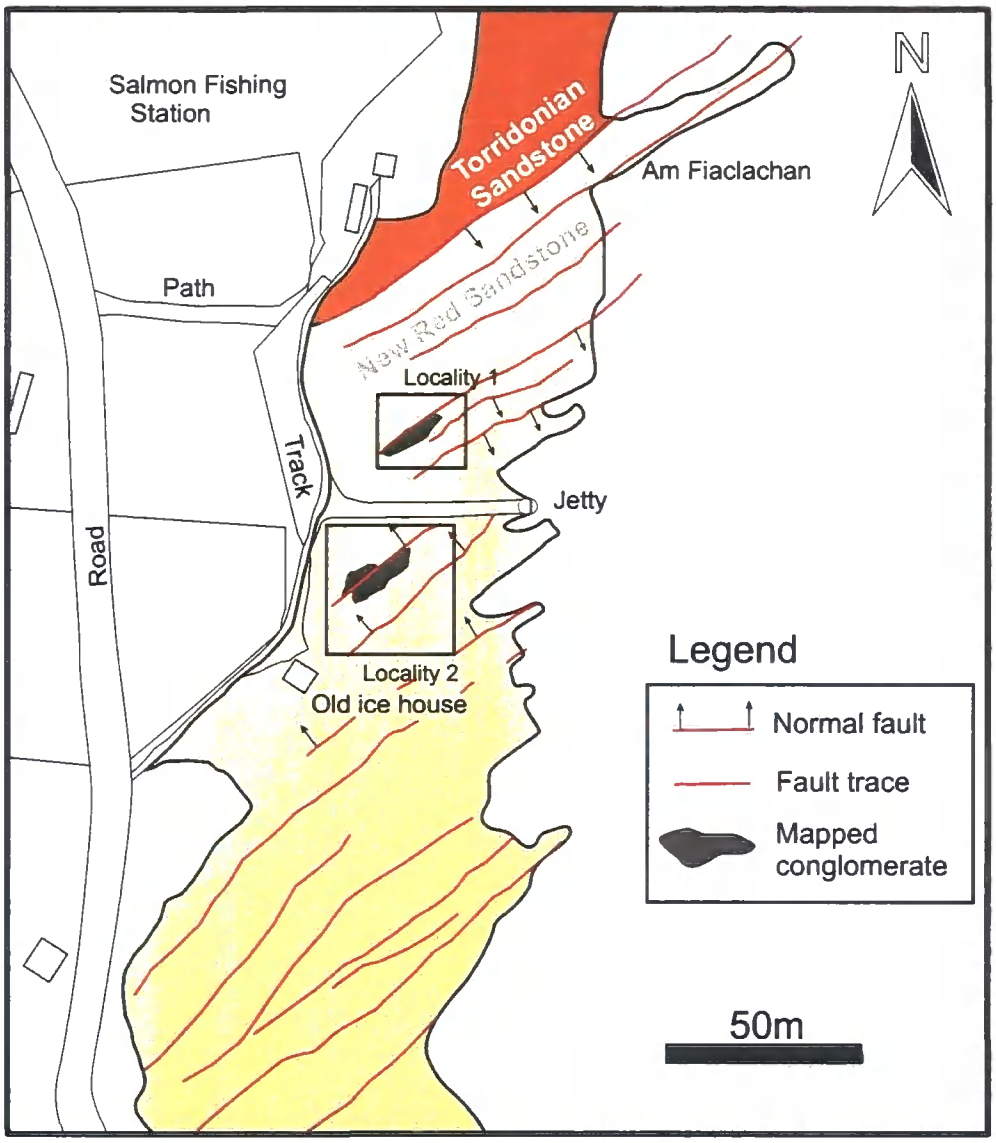

Figure 4.2: Map of normal fault system exposed in the Mesozoic sedimentary rocks (New Red Sandstone). Local-scale fractures are studied in two well exposed conglomerates at Locality 1 (north of the Jetty) and Locality 2 (south of the Jetty), (Fig. 4.3).

Precambrian crystalline quartzite and red Torridonian sandstones, both of which are cut by numerous intra- to transgranular fractures.

Most of these fractures are developed within the pebbles, whilst the matrix does not exhibit obvious fracture traces at the same scale (Fig. 4.4b). These ca. 2 m thick conglomerate units are cut by a series of NNE-SSW trending normal faults with < 2 m offsets (Fig. 4.4a b). There is little evidence for reactivation of the faults

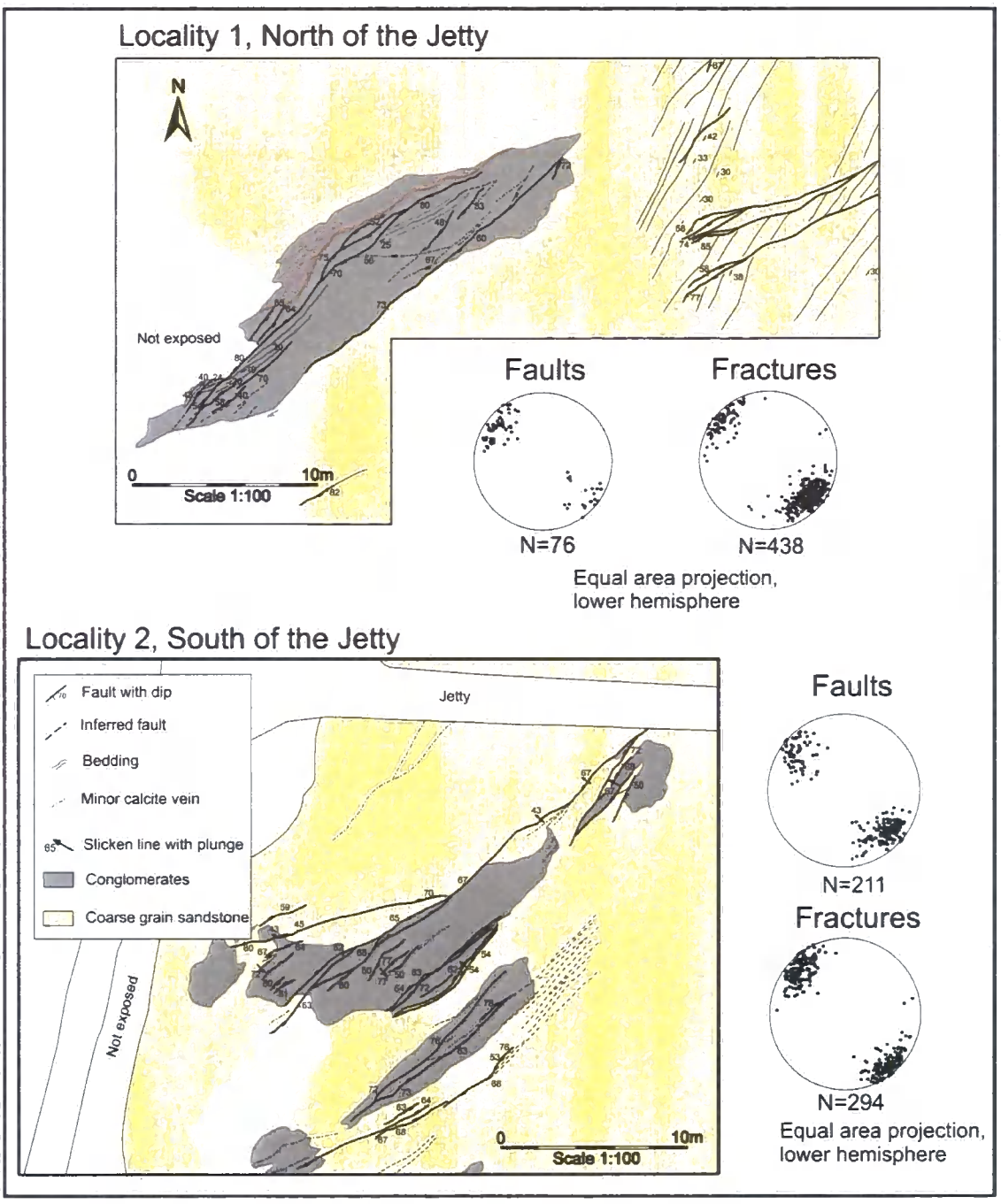

Figure 4.3: Detailed structural maps of fractured conglomerates and associated Sandstones at Locality 1 and Locality 2. The faults show bulk conjugate orientation patterns as shown on the stereoplots. Fractures in the pebbles are showing conjugate patterns with equal numbers of steeply SE and NW dipping sets. Stereoplots data plotted as poles normal to the fracture planes.

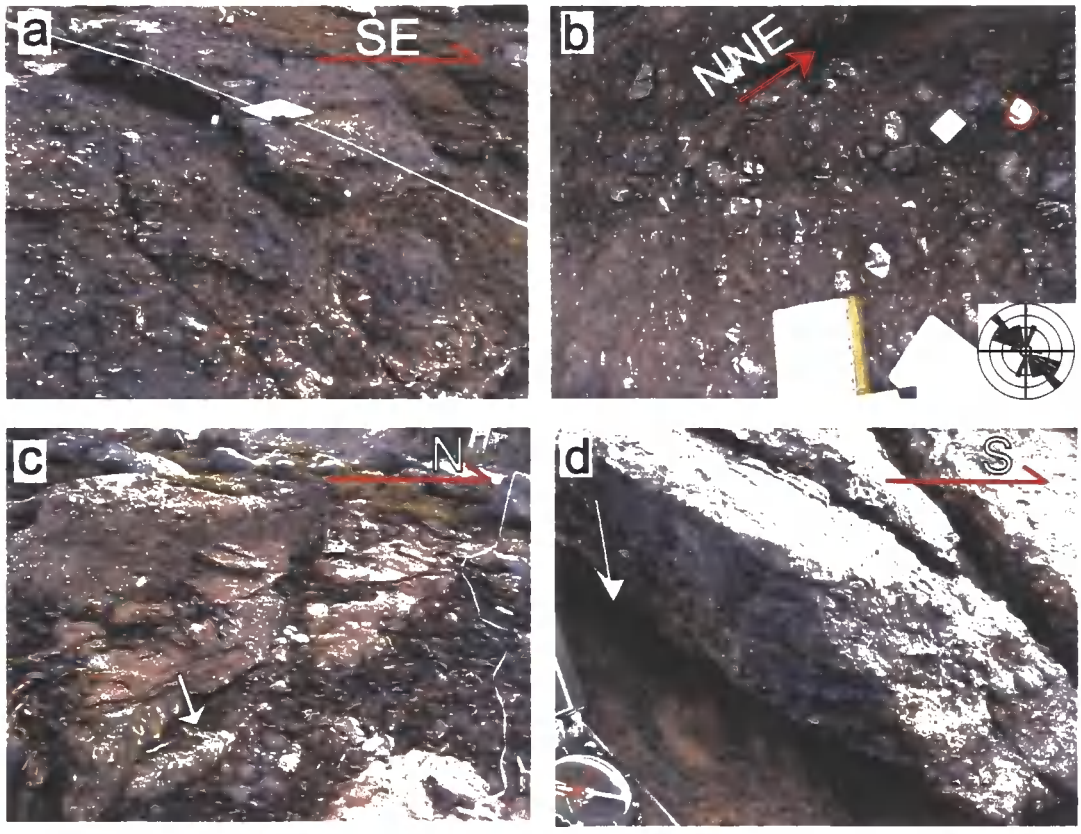

Figure 4.4: Field photos of the fractured conglomerates and coarse grained sandstone. (a)-(b) Faulted conglomerates in which pebbles show preferred orientations. Fracture traces in the pebbles are sub-parallel to the fault trend (b). (c)-(d) Faults developed in the coarse grained sandstone showing dip-slip normal displacement with ca. 0.5 m offsets. The white arrow shows the trend of the slickenlines on the exposed fault surface.

in the New Red Sandstone exposed in Laide (Beacom, 1999). Slickenlines preserved on the fault surfaces are showing dip-slip displacement (Fig. 4.4c d).

At microscopic scales, the deformation is highly heterogeneous with fractures widely developed both in the matrix grains and the pebbles. The matrix comprises an amalgamation of poorly sorted fractured quartz and feldspar-rich quartzite grains cemented by calcite (Fig. 4.5a b). Fractures occurring within the grains open towards the grain boundaries, suggesting that the direction of their propagation is normal to the grain boundary due to the inter-grain point-loading (McEwen, 1981), (Fig. 4.5b). Fracturing in the grains/pebbles locally generates microbreccias and features consistent with the onset of cataclastic flow (Fig. 4.5c). Compared to the matrix, the grains of quartz and feldspar that make up the sandstone pebbles have

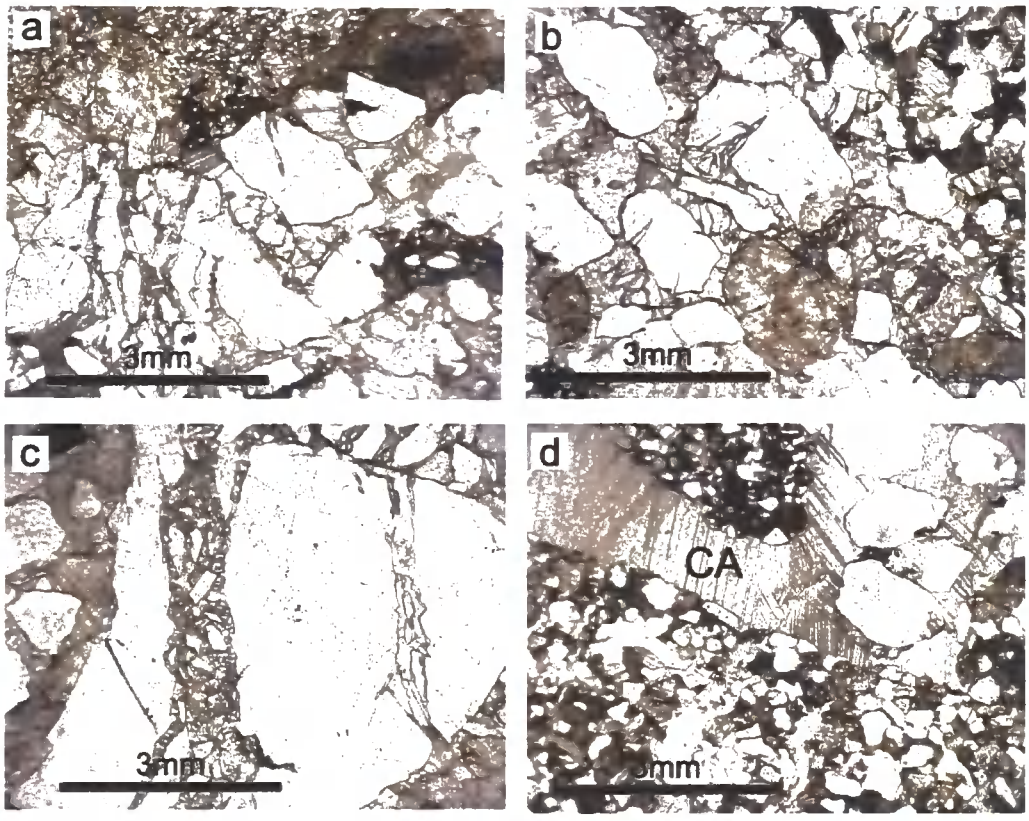

Figure 4.5: Photomicrographs of the fractured conglomerates. (a)-(b) white to light brown coloured grains of quartz and feldspar-rich sandstone are typically heavily fractured. (c) Fractures within a quartzite pebble showing a zone of cataclasite. (d) Undeformed calciate cements (CA) filling pore space between pebbles and grains. PPL

much smaller sizes (ca. 0.3 mm) than that in the matrix (0.5 mm $\sim$ 5 mm). The pore space in the matrix grains and pebble fractures are filled with generally undeformed calcite, indicating that the fracture networks likely formed during a single deformation event (Fig. 4.5d).

4.3 Sampling strategy

The orientation of fractures and faults was sampled systematically across Locality 1 & Locality 2 in the region of the jetty (Fig. 4.3). Fracture orientations from each sampling station (defined by an approximately 1 x 1 m window) were allocated the same spatial location that was recorded on the map to give a geographic reference frame (Fig. 4.6a). Many pebbles in the conglomerates are sufficiently well exposed at

the surface to allow direct measurement of all three axes that define their ellipsoidal shape in 3D (Fig. 4.6b). Thus pebble shape, together with the orientation and spatial location, was recorded for each fracture measurement (Fig. 4.6c). Fault orientation data properties also included the Locality (1 or 2) and bedding lithology from which the data were collected.

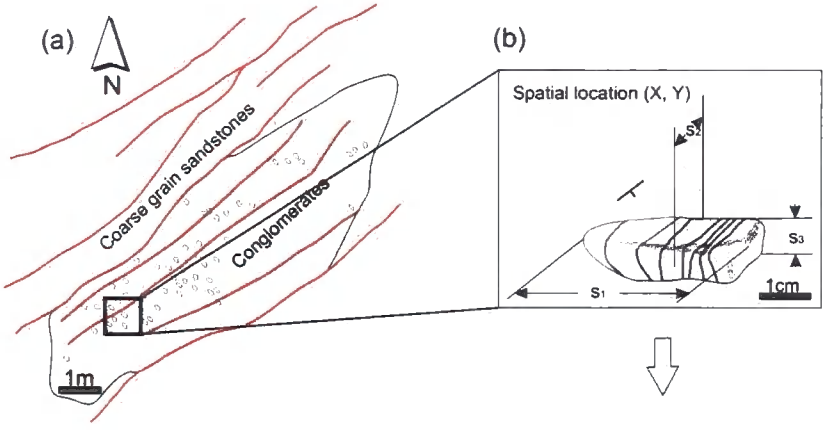

(c)

Pebbles					fractures	
lithology	spatial location	S1	S2	S3	Azimuth	Dip
Quartzite/Sandstone	(X,Y)	a	b	c	θ1	φ1
					θ2	φ2
					⋮	⋮
					θn	φn

Figure 4.6: Schematic diagram of the sampling strategy. (a) Fracture orientation data were collected using a 1 x 1 m sampling window that moves across the conglomerate outcrops. (b) The mutually orthogonal axial lengths of the pebbles. (c) The typical data format.

4.4 Methodology

4.4.1 Bootstrap estimation

4.4.1.1 Bootstrap replications of the mean orientations

The raw orientation data was rotated to the centre of the stereonet for later convenient comparison (Fig. 4.7). For a given sample, after it was rotated to the stereonets centre, a fixed number of the data were randomly sampled from the sample and the mean of these data was calculated. If we repeat this manipulation of data sampling

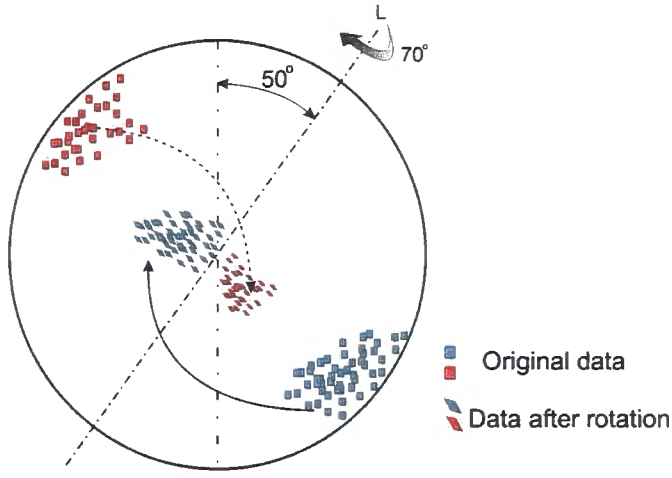

Figure 4.7: The original data were rotated about the 050° axis L by 70° in order to locate the data close to the centre of the stereonets for convenient comparison.

and mean orientation calculation a large number of times, we will get bootstrap replications called simulated data (c.f. 1.1.2.6) of the raw data (Efron, 1982).

4.4.1.2 Bootstrapping the eigenvalues of the orientation data

In order to analyse the relationship between the pebble shape and the orientation pattern of the fractures in the pebbles, the eigenvalues have been calculated from the orientation data selected randomly in a 'moving window' (c.f. 2.3.2). Fracture orientations measured from the pebbles of each lithology are ranked using the k-value derived from the ellipsoid axial ratios of the pebbles from which the orientation data have been collected (c.f. Flinn 1962). A 'window' which contains the fracture orientations measured in the pebbles of similar k-value moves across the dataset from low to high values. Inside each window, a fixed number of the orientation data are sampled randomly and the corresponding eigenvalues λ_1, λ_2, λ_3 ($\lambda_1 \geq \lambda_2 \geq \lambda_3$) are calculated. This random selection in each 'window' is repeated for a very large number of times (e.g. 1000) in order to generate pooled eigenvalues. If we plot the $\ln(\lambda_1/\lambda_2)$ vs. $\ln(\lambda_2/\lambda_3)$ values of each simulation on a Woodcock diagram, the position of the points will reflect the degree of clustering (c.f. 1.1.2.2, Fig. 1.10). If the data plot in the top left corner of the diagram, this indicates a clustered distribution; conversely, if they plot in the bottom right corner, the orientation data follow a girdle distribution (Fig. 1.10). The further the data lie from the origin, the stronger the intensity of that distribution will be; data located near to the origin suggest orientations that are uniformly distributed. A color scheme

can be applied to aid visualization of the relationship between the clustering of the fracture distributions and the pebble shapes: hence, plotted results of the pooled eigenvalues of the fractures sampled randomly in each 'window' are assigned a colour on the Woodcock diagram. As the 'window' moves across the dataset from low to high k-values, the pattern on the Woodcock diagram may change in response to the change of the pebble shape (Fig. 4.8).

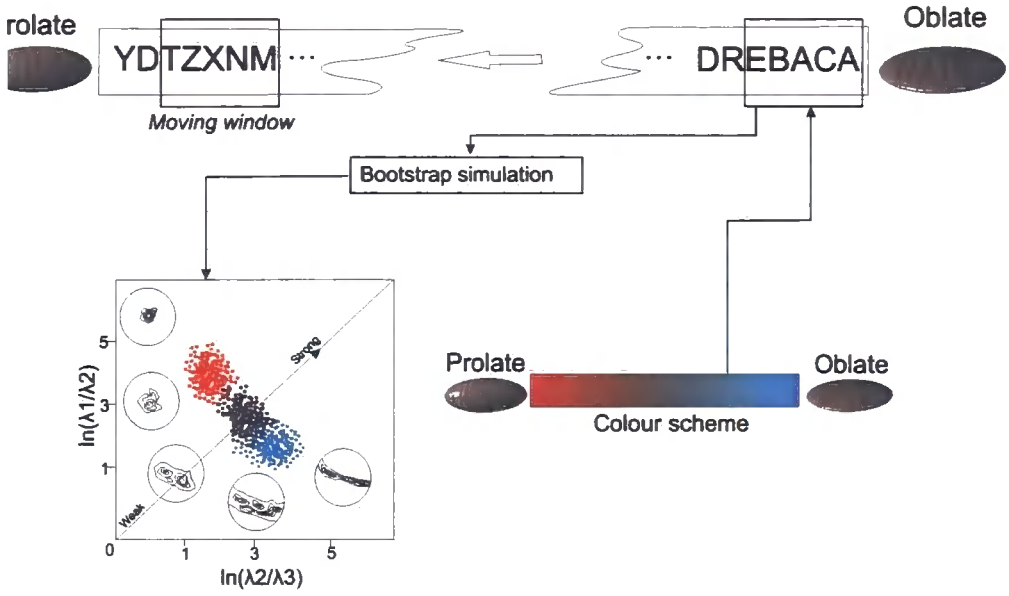

Figure 4.8: (a) Schematic data structure showing that the orientation data were ranked using pebble shapes. Bootstrap simulations were carried out in the moving window to estimate the clustering of the fracture orientations in different parts of the dataset. (b) A colour scheme was simultaneously applied during the simulation to represent the change of the pebble shape from oblate to prolate.

4.4.2 Testing the significance

The simulated orientation data show the error in the true mean orientation and the nature of the distribution for the population (Fisher et al., 1987). The Watson test Watson (1983) was used to test whether two rotationally symmetric distributions have a common mean orientation. To launch this test, we first run the bootstrap simulation in each raw dataset for the same number of times to generate the simulated datasets. Therefore the simulated dataset G_1 from the first and G_2 from the second raw datasets have the same size, namely N. Then we are able to calculate the resultant lengths R_{w1} and R_{w2} (c.f. 1.1.2.3) of each simulated dataset,

respectively. If we mix these two simulated datasets G_1 and G_2 (sample size = 2N), we can calculate the resultant length R_w of the mixed dataset. By using the test statistic (Watson, 1983):

$$G_w = 4N(\rho_w - R_w) \tag{4.1}$$

where $\rho_w = \frac{(R_{w1}+R_{w2})}{2}$, the null hypothesis that the mean orientations are from the same population will be rejected for large G_w values. The Watson test (Watson, 1983) is based on $\chi^2_{\nu,\alpha}$ distribution modal, where ν is the degree of freedom and α is the type I error which should be set up before running the test (Davis, 2002), (c.f. Appendix B). In this two sample test, the degree of freedom ν is 2 and the decision of whether to reject or accept the hull hypothesis is referred to Appendix C.

4.4.3 Variograms

The idea of correlating the spatially distributed dataset is that the data from two closer separated sampling stations are more similar to each other than that from two further separated sampling stations (Isaaks and Srivastava, 1989). This spatial correlation is quantified by the semivariograms or simply variograms (c.f. 1.1.3). For the fracture orientation data, a modified equation 1.6 is required to investigate the spatial correlation.

4.5 Results

4.5.1 Spatial variation of the fractures

The simulated data of the raw dataset show a satisfactory estimation of the distribution model (Fig. 4.9). The fractures and faults orientations display a weak bulk unimodal distribution. The Watson test of the simulated data suggests that the faults developed in both conglomerates and surrounding pebbly sandstones are significantly different at Locality 1 and Locality 2 with 5% type I error, while at each locality the mean orientations of the faults in the conglomerates and coarse grained sandstone are also significantly different with 5% type I error (Fig. 4.9a). The fracture orientations measured from the sandstone and quartzite pebbles in the conglomerates at Locality 1 and Locality 2 have similar results to the faults at bedding-scale, but the pebble lithology does not make any difference in the mean fracture orientations (Fig. 4.9b).

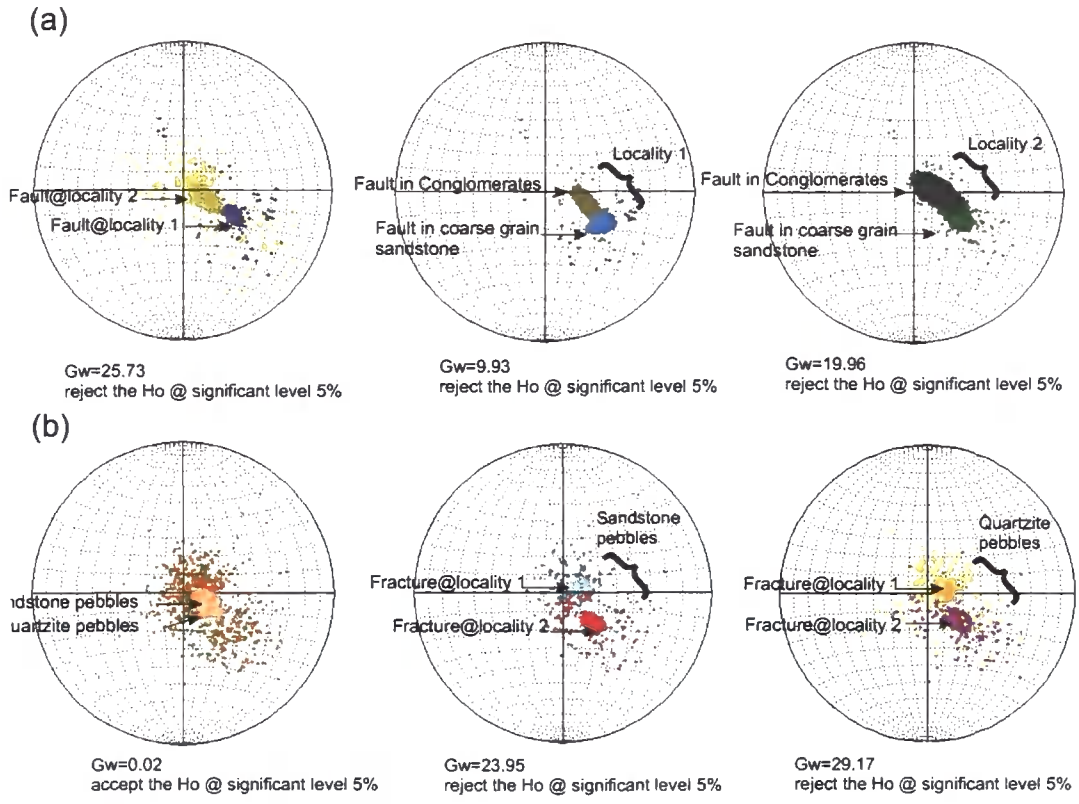

Figure 4.9: Results of the Watson test. The scattered data are the rotated fault/fracture orientations as indicated in Fig. 4.7. High concentration plots are the corresponding bootstrapped estimations. The orientation data present on the standard stereonets are the poles normal to the planes. Ho represents the null hypothesis that the data are from the same population. (a) Meter-scale fault orientation data. (b) fracture orientation data from the pebbles.

4.5.2 Spatial correlation of the fractures in the pebbles

Variogram analysis show that fractures developed in the sandstone and quartzite pebbles have a weak spatial correlation — a general increase in the variance $\hat{Y}(h)$ as the separating distance h (lag) increases (Fig. 4.10). The nugget effects and sill of fracture orientations from both pebble lithologies seem to be similar around 27^o, whilst the range of the data from each are somehow different. In the sandstone pebbles, the variance $\hat{Y}(h)$ of the fracture orientation appears to increase more sharply than that in the quartzite pebbles, reaching the sill ca. 34^o when the separating distance h is at a range of ca. 30 m (Fig. 4.10a). It seems that the variance $\hat{Y}(h)$ of the fracture orientation data from quartzite pebbles does not reach the sill until ca. 36^o at a range of h of ca. 50 m (Fig. 4.10b).

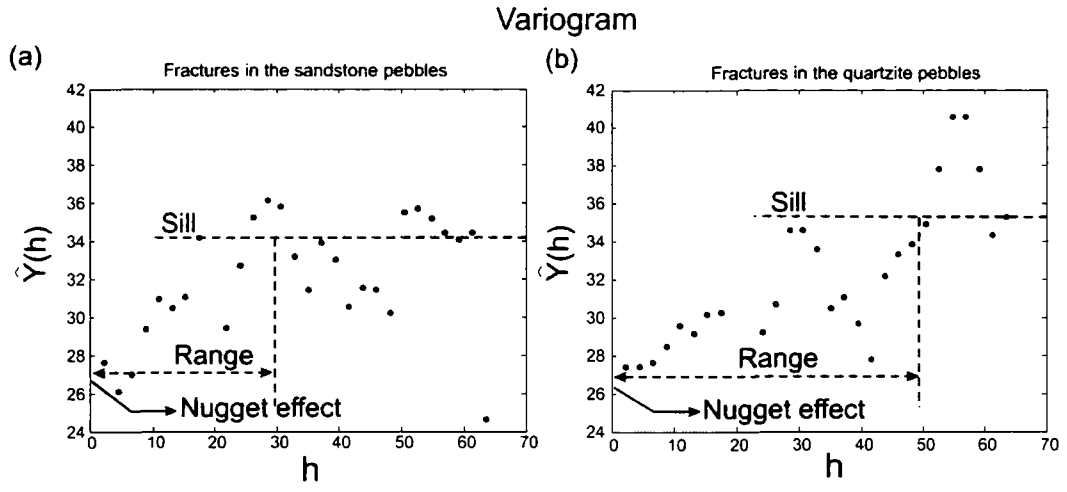

Figure 4.10: Results of the variogram analysis. The variograms of the fracture orientation data from sandstones (a) and quartzite pebbles (b) seem to be different. The scale of h-axis is meter

4.5.3 Pebble shape vs. fracture orientation pattern

The results of the analysis presented in 4.4.1.2 suggest that the fracture patterns in the quartzite pebbles are affected by pebble shape. Colours shown on the plots correspond to the change in k-value illustrated by the colour bar. As this changes from low to high values ($0.63 \sim 3.5$), the colour changes from blue to red (Fig. 4.11). As the pebble shape changes from oblate to prolate, the fracture distribution model changes from bimodal to unimodal, indicating an increase in the degree of the fracture orientation clustering (Fig. 4.11). In the sandstone pebbles, the fracture orientations do not show such a well-developed correlation to pebble shape compared to the quartzite pebbles (Fig. 4.11).

4.6 Discussion

4.6.1 Bulk spatial variations

The results suggest that the bulk mean orientations of the fault/fractures at Localities 1 and Locality 2 are significantly different, at a 5% type I error (Fig. 4.9). There is also a relationship between the bulk lithology (at bedding-scales) and mean fault orientations. Within each lithology (conglomerates and coarse grained sandstone), the mean fault orientations are significantly different at both localities. Furthermore, the fault mean orientations from these lithologies at the same locality are also

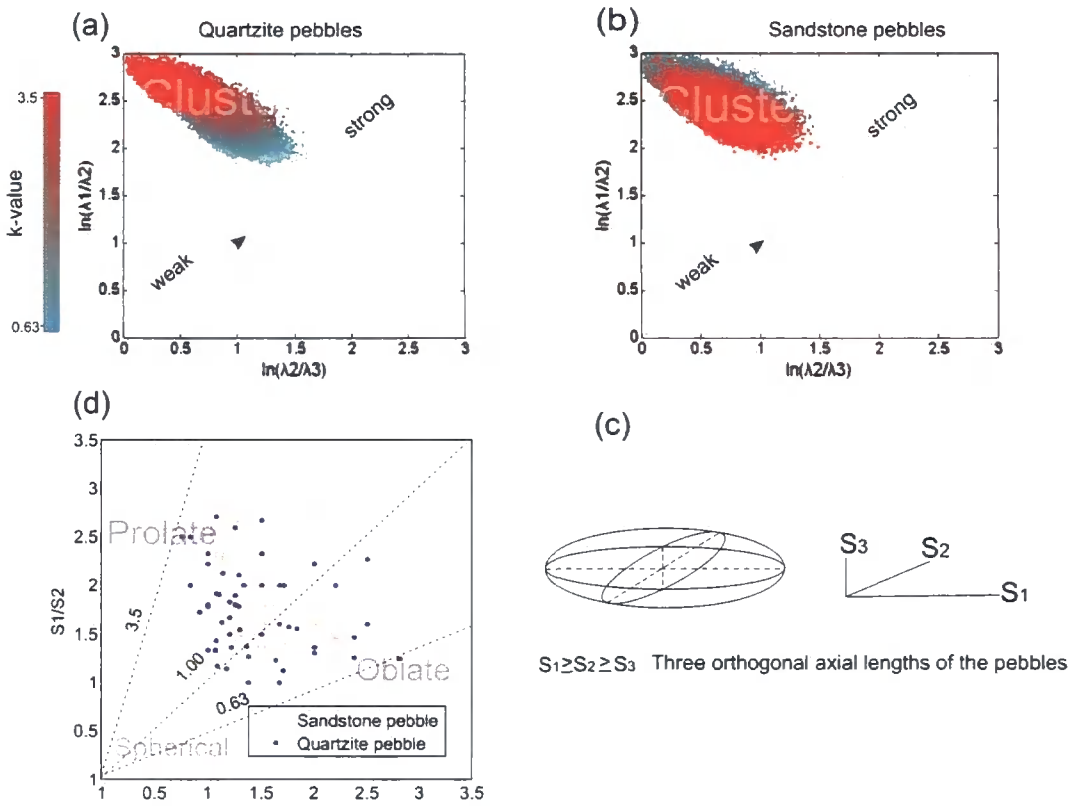

Figure 4.11: Relationships between pebble shape and fracture orientation pattern. For quartzite pebbles, their shape exerts more impact on the fracture patterns compared to sandstone pebbles: as the shape varies from oblate to prolate, the degree of clustering of the fracture orientations increases.

significantly different from each other (Fig. 4.9a b).

The general implication from these results is that significant variation in fault orientation in the same lithology at different localities suggests that the adjacent large-scale normal fault that formed these local deformations is controlling the local strain field. In the fault damage zones, it has been suggested that changes in faulting patterns on approaching the fault core region reflect local stress field rotations (Faulkner et al., 2006). In addition, the heterogeneity of the lithology may also modify the local strains even under a homogeneous displacement field (Eshelby, 1957; Reches et al., 1992). Ideally, to understand the spatial variations of fault orientations, one has to map out the distribution of the lithologies which are considered to have similar deformation histories as well as recording the locations of the sampling stations relative to the adjacent master fault.

Previous studies have already demonstrated that variations in fault density, fault

zone thickness and other attributes occur when there is a change in both location and lithology (Knott et al., 1996; Wilson et al., 2003; Putz-Perrier and Sanderson, 2008). However, none of these studies have examined the spatial heterogeneity in the fault orientation as their focus. Furthermore, as real field data can be very noisy (c.f. 1.1.2.6), a simple visual comparison of orientation data from different groups (e.g. spatial locality, lithology etc.) may be very difficult without use of the statistical methods suggested in this chapter. The findings of the present study suggest that subtle and significant variations in the bulk fault/fracture orientations are common in nature and confirms the general heterogeneity of the strains developed in fault zones.

4.6.2 Spatial correlation of the fracture sets

The variograms of the fracture orientations from sandstone and quartzite pebbles indicate a general spatial correlation (Fig. 4.10) within ca. 40 m separating distance. Although the nugget effect and sill are more or less the same in fractures from sandstone and quartzite pebbles, the range values appears to be different (Fig. 4.10). The fracture orientation data from the sandstone pebbles lose their spatial correlation within 30 m; whilst those from quartzite pebbles gradually lose their spatial correlation within 50 m (Fig. 4.10). As the field-based variograms are very scattered (Fig. 4.10), the significance of the difference needs to be further investigated (c.f. 5). Such a difference, to a certain extent, reflects the influence of the mechanical contrast between the pebbles and surrounding matrix (Eshelby, 1957; Gay and Fripp, 1976), as discussed below.

4.6.3 fracture/fault orientation pattern

2D experiments on deforming brittle inclusions within a ductile matrix suggests that, under pure shear, rigid elliptical inclusions of spherical shape tend to develop bimodal (conjugate) shear fractures whilst less rigid ones of prolate shape tend to develop unimodal tensile fractures (the long axis of the inclusion is parallel to the extensional displacement) (Mandal et al., 2001). In practice, differentiating these two modals still remains a problem in that a diffuse unimodal orientation pattern may be a bimodal (or polymodal) whose clusters are very closely separated. The 'elongated' clusters (e.g. the fracture/fault orientation pattern in the present study) which are geometrically simplified as 'weak unimodal' (c.f. 4.5.1) can represent different deformation mechanisms. Given a fixed local strain field and pebble orientation, the

fracture patterns in the pebbles depend on the lithological contrast (pebble/matrix) and the pebble shape (c.f. Eshelby 1957; Mandal et al. 2001). Therefore different fracture patterns (bimodal/unimodal) may represent the same local strain or even the regional displacement field (e.g. Eidelman and Reches 1992). For the fault orientations, conjugate sets (bimodal) can be used to infer the maximum and minimum principle strain direction whereas the unimodal sets may belong to one cluster of the conjugate sets or representing a simple shearing mechanism. This suggests that simplifying fault orientation pattern only by the geometrical similarity should be taken great care. The faults in the present study exhibit an 'elongated' unimodal and simplified as a 'weak unimodal' only for statistical comparisons and are not suitable for interpreting deformation mechanisms.

4.6.4 Pebble shape & lithology

The results of the shape analysis clearly indicate that the shape of the quartzite pebbles affects the fracture orientation patterns that develop, yet the sandstone pebbles shown no such relationship. According to Eshelby's theory (Eshelby, 1957), the shape of the inclusion is one of the critical factors that should affect the internal state of stress. Other factors also include the contrast of Poisson's ratio, viscosity, and frication coefficient etc. between the inclusions and matrix (Eshelby, 1957; Gay and Fripp, 1976; McEwen, 1981).

It is proposed that the sandstone pebbles have no clear relationship between the pebble shape and fracture orientation patterns because their mechanical properties are more similar to those of the surrounding sandstone matrix. Gay and Fripp (1976) have demonstrated that inclusions with lower viscosities relative to the matrix will experience more deformation. Thus sandstone pebbles set in a marble matrix deform much more compared to quartzites under very low grade metamorphic conditions. In the present study, the viscosity of the poorly cemented sandstone matrix is likely to have been lower than that of the sandstone and quartzite pebbles. This suggests that the compaction and traction on the pebble boundary applied by the flowing matrix during deformation should not be ignored (McEwen, 1981). Local lithological heterogeneity will therefore perturb the uniform far field stress field applied to the imaginary homogeneous rock mass (Eshelby, 1957). Eidelman and Reches (1992) have pointed out that competent pebbles embedded within a compliant matrix will tend to amplify the stresses in the matrix. This seems consistent with the results presented here: 'harder' quartzite pebbles have a larger mechanical contrast with

their surrounding sandstone matrix: hence these competent inclusions are more sensitive to the inclusion shape.

4.6.5 Mechanical stratigraphy and bedding orientation

In the study area, the bedding orientation has a regional ca. 20^o dipping to the NE with a few moderately dipping beds of ca. 40^o close to the meter-scale faults. These tilted beds were developed during the faulting/fracturing and supposed to be another factor that affects the fracture orientation in the pebbles (c.f. Van-der Zee et al. 2008). As a mechanical stratigraphy, the bedding thickness and lithology will normally determine the deformation mechanism and influence the fracture pattern in the wall rocks (e.g. Gross 1995; Schopfer et al. 2006; Van-der Zee et al. 2008), but in some cases such as in porous, poorly cemented granular rocks, the bedding and cross bed sets has no substantial effect on fault behaviour (e.g. Underhill and Woodcock 1987). The structure data in Laide are mainly from one single bed (data sampled on the pavement) of similar orientation (only a few from highly tilted beds). This suggests that the influence of the bedding thickness and orientation can be minor compared to the bulk lithology and master fault control.

4.7 Conclusions

The fractures in the pebbles and meter-scale faults in the conglomerate-sandstone sequences exposed at Laide, NW Scotland, provide an example of brittle deformation in a lithologically and mechanically heterogeneous sequence of rocks during extensional faulting. The results indicate that:

1. Spatial variations in the fault orientations at different scales are common even in a very small area (ca. 30 x 70 m). Such variations can be very subtle but are nevertheless significant, and may be easily overlooked. The key factors that control these variations are believed to be the distribution of the bulk (bedding-scale) lithologies and distance from major faults.

2. Fracture orientations from quartzite pebbles in the conglomerates studied here are spatially correlated over a larger range compared to sandstone pebbles, even though the nugget effect and sill are similar for both types of pebble.

3. Although the pebble lithology does not exert a profound influence on the bulk fracture orientation pattern, it does affect the fractures developed within individual pebbles. There is a clear relationship between the quartzite pebble

shape and the fracture orientation pattern developed inside the pebbles: prolate shapes are likely to develop unimodal fracture distributions and oblate shapes are likely to develop girdle or bimodal fracture distributions. This has been confirmed using the different variogram patterns of the fracture orientations from quartzite and sandstone pebbles.

The significant contribution from this study is that spatial variations in fault/fracture orientations are common in natural fault zones — subtle, yet significant variations in fault and fracture bulk orientations seem to be common in nature and can now be incorporated into fault models.

Chapter 5

Discussion & Conclusions

Three field-based case studies present in the thesis have demonstrated that geometric relationship, orientation and kinematics of the fractures change substantially inward towards the fault core in damage zones. In spite of different bulk strains, the fracture orientation patterns vary from outer zone to inner zone, indicating a systematic change of the local strains. This spatial heterogeneity is possibly due to the scale of observation, influence from the fault core, and mechanical anisotropy. However, these three are not independent factors and if one changes, the other can change correspondingly, e.g. lithologies at crustal scale and mesoscale may behave in a different way (e.g. Faulkner et al. 2008); spatial variations of the fracture pattern can be affected by local mechanical heterogeneities (e.g. Gross 1995). For the above reasons, the bulk fracture orientation data are normally very diffuse and may contain several subsets which are believed to have significantly different models (Fig. 5.1). It has been demonstrated that bootstrapping technique and spatial correlation analysis are robust to delineate the spatial heterogeneity in the diffusely distributed datasets. The advantage of including the associated methodology becomes apparent: the ability to launch more rigorous comparison between noisy datasets and correlate each measurement in a spatially constrained context. This allows one to simulate the high connectivity and conductivity of channels in subsurface (La Pointe, 1993) and predict fracture patterns in unsampled areas (Isaaks and Srivastava, 1989).

5.1 Scale of observation

Fracture orientation patterns observed at finer scales tend to be more complicated than patterns at coarser scales (Jones et al., 2005). This is because the local strains are heterogeneous due to the interaction between local factors (layering, foliation,

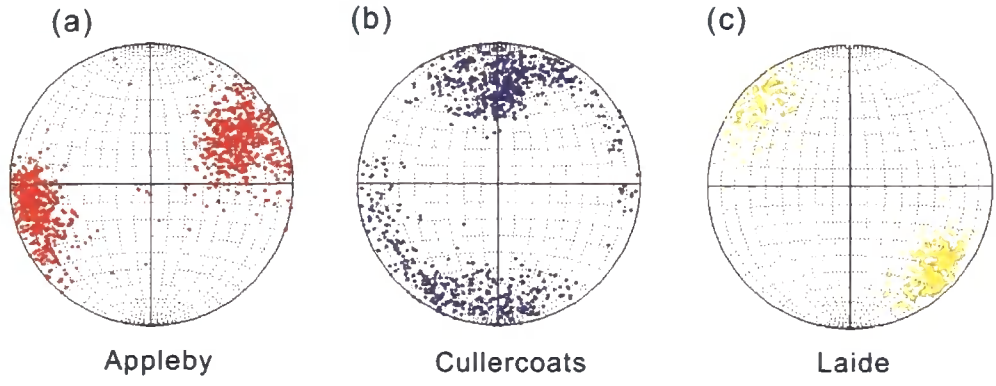

Figure 5.1: The whole fracture orientation datasets from three fault damage zones. (a) Appleby: the diffuse orientation patterns are due to the scale of observation and rotation of the subsets collected at localities moving progressively close to the fault core. (b) Cullercoats: the diffuse orientation patterns are the combination of distribution modal changing from bimodal to polymodal as the sampling station moving towards the fault core. (c) Laide: the diffuse orientation patterns are caused by lithological heterogeneities with local boundary conditions (pebble shape) and spatial locality.

faults, lithology, etc.) and therefore not parallel to the bulk strain (Hesthammer et al., 2000; De Paola et al., 2005a,b; Jones et al., 2005). For example, the geometry and spatial patterns of structures within the Northumberland Basin is best explained by a 3D strain partitioned heterogeneously due to pre-existing structures and lithology (c.f. De Paola et al. 2005a,b). The granularity of the fracture system (c.f. 2) is the 'pixel' size at which the system is viewed: the finer scales suggest 'smaller pixels'. Take the Appleby case study for example, the model of the fracture orientations collected at fine scales can be different from coarse scales (Fig. 2.4a b). For the spatial correlation analysis, the range of the spatially distributed data in a given region reveals the scale at which the dataset can be viewed as being essentially homogeneous with the variance close to the sill. The spatial correlation analysis shows that at scales below the range, the dataset is heterogeneous and their distribution pattern will vary at different scales; whereas at scales larger than the range, the datasets will be homogeneous and their distribution pattern will be scale-invariant.

For this scale issue, in practice, the various sizes of the sampling stations will indirectly reflect the scale of observation. Thus, datasets made up of measurements from small sized sampling stations represent local scale features of the fracture

orientation. Similarly, large size sampling stations which cover a regional area will provide the global estimation of the fracture orientations. The deformation bands exposed in George Gill, Appleby illustrate that at fine-scale of observation, the deformation bands display polymodal sets masked by the bimodal orientation data collected at a coarse-scale of observation (Figs. 2.4 5.1a). Similar features have also been discussed in other natural fault zone examples (e.g. Aydin and Reches 1982; Healy et al. 2006a). This heterogeneity is more obvious in Cullercoats: regionally E-W trending faults with the polymodal fractures developed under 3D non-coaxial strain (De Paola et al., 2005a,b). Additionally, the distribution of strain in this transtensional fault zone is so heterogeneous that the fracture orientation spatial correlation is not isotropic (Fig. 3.10b c). In a direction perpendicular to the main fault trace, the fracture orientations are spatially correlated; traverse parallel to the main fault, the orientation data are not spatially correlated at any scales. This implies that the heterogeneity in orientation datasets may be anisotropic in fault zones: perpendicular to the main fault trace direction, the orientation data vary with scales up to the range of the variogram (e.g. 80 m in Cullercoats); parallel to the main fault trace, the orientation data are scale-invariant.

For extensional fault zones, the secondary fracture orientations seem to be simpler than reactivated fault zones. Fine-scale fractures at Laide in Gruinard Bay have orientations that are similar to the faults and can be used as indicators of the bulk strain (Fig. 4.3). This is consistent with fracture variograms that show a fluctuating pattern, indicating a weak spatial correlation: finer-scale observations may be similar to the coarser-scale observations (Fig. 4.10).

By comparing the field data, variograms with intensively simulated random modals, one can find the significance of the spatial correlation. A random variogram modal is generated by randomly permutating the original spatially distributed data a large number of times. The variogram of the randomly permutated dataset at each simulation forms a zone (Fig. 5.2). If the field data variogram falls into this zone, it indicates that these data are not likely to be spatially correlated and vice versa. As Figure 5.2 shows, the variogram of the fracture orientations from Gruinard Bay fall into the zone of its random modal counterparts, the data is reasonably homogeneous and expected to exhibit scale-invariant characteristics (Figs. 4.3 5.2a a'). For the Appleby deformation band orientation data, the field variogram curve is located just outside the random model before the lag h reaches ca. 25 m after which it falls into the random zone (Fig. 5.2b). The field variogram in the direction perpendicular to the 90-Fathom Fault shows a big difference to its random modal (Fig. 5.2c), whilst parallel to the main fault trace the result is similar to the Gruinard Bay case

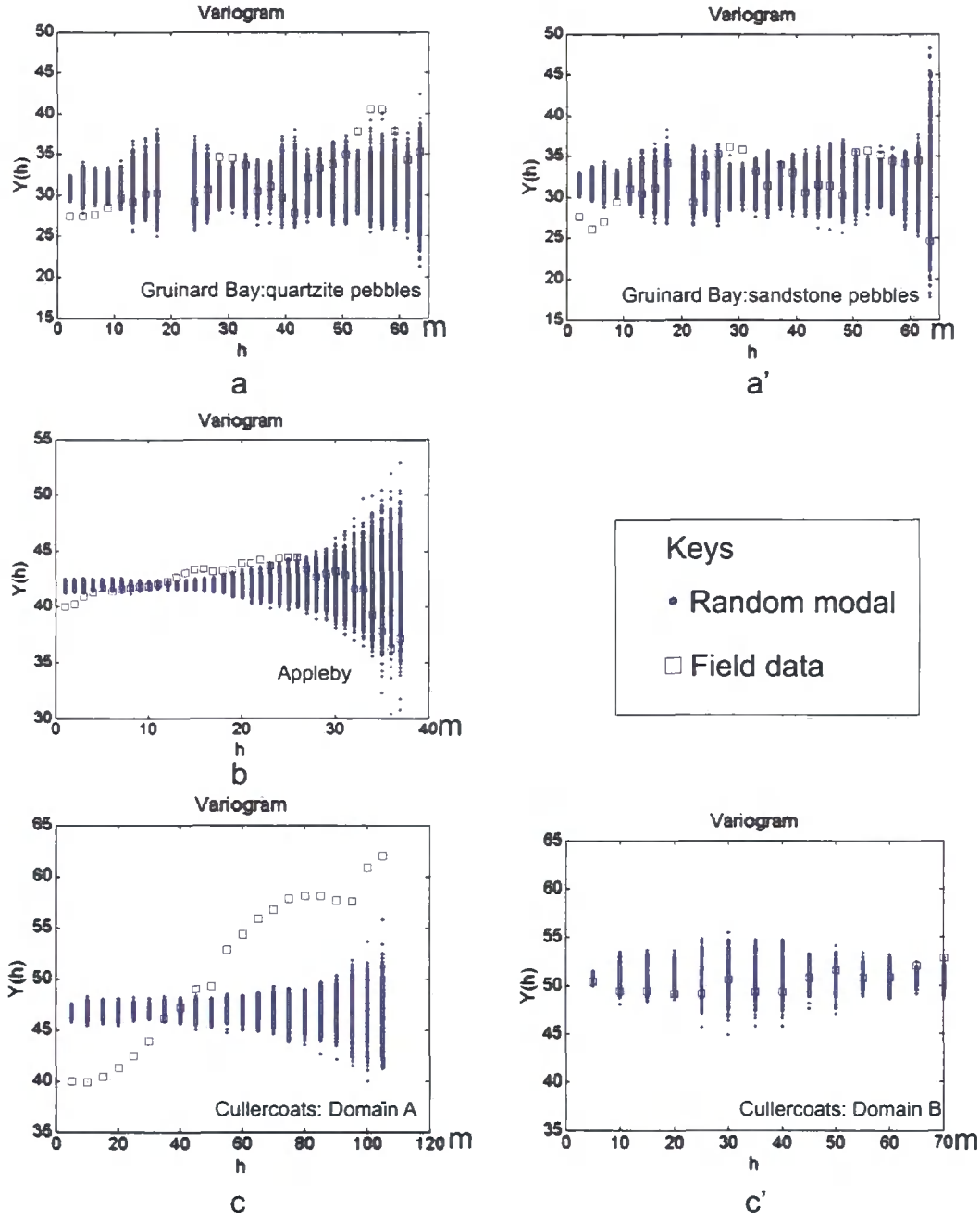

Figure 5.2: Comparison between field variograms and their random model counterparts. (a)-(a') The field variograms lie in the random zone, indicating no significant spatial correlation amongst the measurements. (b) The field variogram of the Appleby deformation band orientation data shows strong spatial correlation before the separating distance reaches ca. 25 m, after which the curve of the field variogram falls into the random zone. (c) Variogram of the fracture orientations sampled in the direction perpendicular to the trend of the 90-Fathom Fault showing a very strong spatial correlation. (c') In a sampling direction parallel to the main fault trace, however, no significant spatial correlation has been found.

(Fig. 5.2c'). This comparison clearly suggests that the fracture orientation dataset from Cullercoats is more heterogeneous than that from Appleby, and both examples illustrate characteristics that vary with scale from meter- to regional-scales.

The spatial correlation analysis gives rise to detecting interconnected fracture patterns in damage zones which may form high permeability fluid pathways through the rock mass and makes it possible to identify large scale interconnected block structures in fault zones that are critical for reservoir development and simulation (La Pointe, 1993).

5.2 Geometric & spatial variation

Existing mechanisms of fault damage zone evolution suggest that fracture orientation patterns become complicated near the fault core (Shipton and Cowie, 2001). The pattern is also simpler in the fault tip area than in the fault zone center (Aydin, 1978; Shipton and Cowie, 2001). In 3D strain, the propagation and interaction of microfractures or fault segments will eventually create polymodal fault patterns (Vermilye and Scholz, 1998; Healy et al., 2006b). Such geometric complexity in fracture sets make it statistically difficult to define a 'good' cluster (c.f. Ye and Rabiller 2000). Thus many previous workers were constantly using geological constrains such as timing, lithology, spatial location, etc. to investigate the geometric and spatial heterogeneity in fracture sets (e.g. Johansen and Fossen 2008; Gross 1995; Wilson et al. 2006). Delineating the 'polymodal' fracture pattern is still qualitative in the thesis and is constrained by mutually cross-cutting fractures of multiple orientation in the field.

Across fault zones from damage zone to fault core, stress conditions change gradually as shown by the stress trajectories in laboratory analogues (Fig. 5.3), (Hafner, 1951). In natural fault zones, stresses can rotate as their magnitude increases towards the fault core (Faulkner et al., 2006), causing a change of the fracture patterns, such as density, displacements and orientation (e.g. Peacock 1991; Knott 1994; Knott et al. 1996; Johansen and Fossen 2008). The mechanisms generating these fractures are proposed to control their spatial characteristics (c.f. 2 3 4.2). The overlap of local variation in fracture orientations will subsequently diffuse the bulk distribution modal on the stereonets (Fig. 5.1a b). This also makes the discrimination of multiple fault sets even more difficult, as polymodal pattern can be always masked by diffuse orientation patterns.

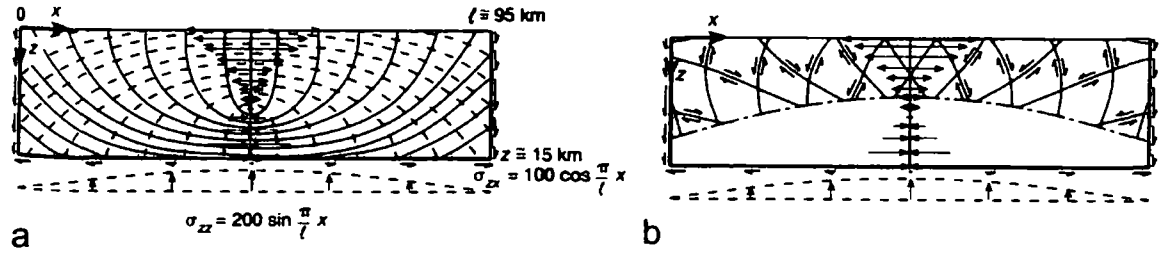

Figure 5.3: A laboratory analogue experiment showing stress trajectories and predicted fault planes. (a) Tractions and stress trajectories of a block with a basal normal stress σ_{zz} varying as a sine function and shear stress σ_{zx} varying as a cosine function; solid lines are trajectories of maximum principle stress and dashed lines are trajectories of minimum principle stress. (b) Predicted fault surfaces indicating that the orientation of the fault planes should have systematic spatial variation under the displacement field (Hafner, 1951).

For classifying the spatial variation patterns, two tentative end-member models were proposed in 3.5:

- Model A: the fracture orientation patterns change across the fault zone.
- Model B: the fracture orientation patterns mainly rotate as moving close to the fault core without substantially being complicated.

In a traverse direction perpendicular to the main fault trace, fracture orientations in the hanging wall of the 90-Fathom Fault vary by changing the pattern from bimodal to polymodal without significantly rotating the mean orientations (Figs. 3.8 3.12 5.4a), (Model A dominant). By contrast, the fracture orientations from Appleby rotate systematically with a relatively simple bulk bimodal orientation pattern (Figs. 2.8 5.4b), (Model B dominant). It is likely that the Gruinard Bay data will exhibit the Model B pattern, as both the bulk orientations of the fractures and faults have simple bimodal distribution patterns and only show rotation (Fig. 4.9) but more sampling stations are required to give confidence to this inference.

It seems that orientations of the internal fractures in transpressional/transtensional fault zones where strain partitioning has developed — a seemingly common situation (e.g. Shipton and Cowie 2001; Jones et al. 2005; Lewis 2007) — should follow a Model A pattern, indicating that the strain changes on moving from damage zone to fault core. Model B fracture patterns seems to emerge in extensional fault zones.

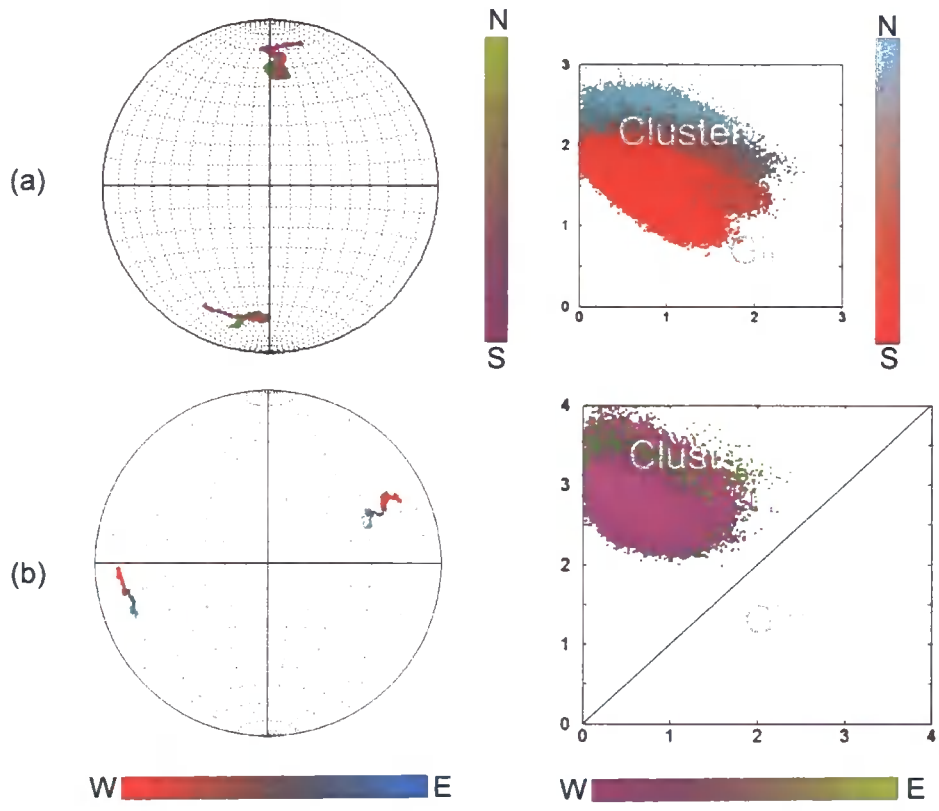

Figure 5.4: (a) Fracture orientations in Cullercoats follow the Model A variation pattern: in N-S direction, the mean orientations do not change substantially, whereas the orientation pattern changes from strong to weak degree of clustering. (b) Fracture orientation in Appleby follow the Model B variation pattern: in E-W direction, the mean orientations rotate systematically, whereas the orientation pattern does not show substantial variation.

Examples of natural fault zones in Utah (Black Hole Fault, Blueberry Fault, Moab Fault, etc.) display similar polymodal deformation patterns close to the fault cores (Shipton and Cowie, 2001; Johansen and Fossen, 2008). The propagation of the localized fault cores in the porous aeolian sandstone are believed to control the local strain field, invoking 3D deformation in their vicinity, whilst subjected to relatively simple extensional bulk strain (Shipton and Cowie, 2001). Therefore, a hybrid A + B model might more realistically characterize the spatial variations in fractures of general fault zones.

5.3 Mechanical heterogeneity

Many field-based studies suggest that bulk lithology substantially affects fracture patterns (e.g. Shipton and Cowie 2001; De Paola et al. 2005a; Healy et al. 2006a; Johansen and Fossen 2008; Putz-Perrier and Sanderson 2008). Thus, different rocks may response differently under similar tectonic loading conditions, e.g. as illustrated by the fracture systems in Cullercoats and Gruinard Bay (c.f. 3 4.2). The co-existence of bimodal and polymodal faulting patterns at different scales and/or at different locations relative to major faults indicates that bulk strain is commonly modified by mesoscale mechanical heterogeneities.

The rock mass is often subjected to a volume change during the deformation — an effect that will be more obvious in high porosity rocks (Aydin, 1978). De Paola et al. (2005a) have demonstrated that fractures developed in porous sandstone and the overlying dolostone in the region close to the 90 Fathom Fault at Cullercoats have polymodal and bimodal patterns, respectively, in immediately adjacent beds (also c.f. 3). In Gruinard Bay, fractures and faults in the conglomerate-sandstone sequence have similar bimodal conjugate patterns (c.f. 4.2) whereas deformation bands in the surrounding porous sandstone exhibit polymodal patterns as described by Healy et al. (2006a). This evidence clearly suggests that lithology is one of the critical factors that controls faulting patterns.

At various scales, the distribution and orientation of faults are also influenced significantly by pre-existing structures. These seem to be particularly important in reactivated fault zones where the pre-existing structure lies significantly oblique to the regional displacement field (Dewey et al., 1998). By contrast, the bulk lithology does not affect the degree of heterogeneity in the fractures developed at the regional scale. The influence of local scale lithological heterogeneity also varies: the bulk fracture orientations do not appear to be affected by the pebbles in the conglomerates (c.f. 4.2), whilst the fracture style is genetically related to interbedded mechanical units (Gross, 1995; Schopfer et al., 2006). In many cases, bulk 3D non-coaxial strains are broadly partitioned into several domains due to pre-existing regional scale structures (zone of mechanical weakness), whereas at mesoscales, the bulk lithology does not primarily control the fracture localization, but rather determines the fracture pattern in response to the applied strain field to form sub-domains (e.g. Beacom et al. 2001; De Paola et al. 2005a,b; Taylor et al. 2008).

Stratigraphic anisotropies i.e. beddings can behave as mechanically weak layers to accommodate part of the bulk strain and subsequently affect the fracture pattern. Three case studies do not show discernible relative slip surfaces between the adjacent

beds. In addition, most of the fractures are cutting in high angle to the bedding orientation. For porous poorly cemented sandstones, beddings are simply chronological sequences and do not show preferred mechanical weaknesses along adjacent beds (c.f. Tucker 2001). This is typical for cross-bedding aeolian sandstones, which can be approximated as homogeneous materials. For rocks of distinct mechanical stratigraphy, the lithology and thickness of each individual bed will significantly affect fracture patterns by controlling the failure mode (e.g. Gross 1995; Schopfer et al. 2006; Johansen and Fossen 2008).

Overall, mechanical heterogeneity exists in a wide range of scales and determines the failure mode of the rock mass and spatial distribution of fractures. Given a regional displacement field, major pre-existing structures forming mechanical weakness zones that influence fault distributions and determine strain domains (e.g. transpression and transtension) where bulk lithologies and mechanical stratigraphy control the failure mode during deformation.

5.4 Bedding orientation & minor fault influence

It is supposed that the influence of folded beds relating to the hanging-wall deformation will influence the fracture orientation pattern. Fracturing and folding are interlinked deformation that takes place simultaneously during faulting (Ramsay, 1967). The bedding can be tilted during the on-going faulting process and early formed fractures may be correspondingly rotated and reactivated, producing complex patterns (e.g. Van-der Zee et al. 2008). There is no obvious folded beds in the cliff section in Appleby and only an open fold present in the hanging-wall of the 90-Fathom Fault. Although in Laide, some beds are moderately dipping relating to the meter-scale faults, the bedding shows a broad shallowly dipping characteristic. At large scale of observations, these local fluctuations of bedding orientation may only exert minor effects on fracture patterns. Complex fracture patterns near the fault core can also be the result of accumulative slip (Shipton and Cowie, 2001), minor faults or fault splays reconnected to the main fault (Van-der Zee et al., 2008). Nevertheless, factors influencing fracture patterns seem to be correlated with each other and all controlled by the fault core deformation.

5.5 Influence on the fluid flow

Fault zones can significantly affect the fluid flow pathways in aquifers or hydrocarbon reservoirs by either increasing or reducing the connectivity (e.g. Adams and Dart 1998; Knipe et al. 1998; Sigda et al. 1999; Aydin 2000). Large-scale faults provide information about juxtaposing or connecting distinct permeability units in subsurface: generally, an increased overall vertical connectivity and decreased overall horizontal connectivity; but at fine-scale, the fluid flow behavior can be more complex caused by the presence of secondary structures in fault zones (Manzocchi et al., 1999). Fracture network simulation suggests that the distribution pattern and nature of fracture intersections will substantially affect the fluid pathway, e.g. conjugate fracture patterns may channel the fluid flow in one preferred direction parallel to the fracture intersections and polymodal fracture patterns may not provide a preferred channel (c.f. Huseby et al. 1997; Caine and Forster 1999). The field investigations in the present study suggest that there is an increase in the degree of complexity in the geometric and spatial heterogeneity of fracture orientations from damage zone to fault core. This may lead to the change of the fluid flow behavior at different parts within fault zones while the large-scale pathways may remain relatively simple (c.f. Matthai et al. 1998; Manzocchi et al. 1999). The variogram analysis indicates that, at scale of observation beyond the separating distance (range), the fracture orientation will not be spatially correlated and the pattern will not change regarding the scale (c.f. La Pointe 1993; Manzocchi et al. 1999). It is anticipated that the fluid flow behavior will be unpredictable at fine-scale less than the range and a representative elementary volume (REV) which is four times larger than the range of the variogram defining in the field can be assigned for a more realistic reservoir model (c.f Manzocchi et al. 1999).

5.6 Applications

5.6.1 Fractures in folded beds

The methodologies adopted in the thesis can be used to quantify fracture orientations from other geological settings. An example is a fold (data locations anonymised for commercial reasons, McCaffrey pers. comm.) where fractures distribute across the limb-hinge area (Fig. 5.5). The whole dataset exhibits a very diffuse distribution pattern on the stereonets. Splitting the dataset into subsets based on the spatial location of scanlines, the fracture orientations display obvious spatial variations

(Fig. 5.5a), revealed by both raw data and bootstrapped replicates. In the $S_1 - S_2$ zone of the steep limb (green) fracture orientations are relatively homogeneous (Fig. 5.5b). Yet from S_1 across the fold hinge to S_4, the fractures have a very strong spatial correlation (Fig. 5.5b). In the gentle fold limb area $S_4 - S_7$, the spatial correlation becomes unclear due to the sparsely distributed data (Fig. 5.5b). Nevertheless, these three combined scanlines ($S_1 - S_2$; $S_1 - S_4$; $S_4 - S_7$) have similar nugget effect ca. 40^o (Fig. 5.5b). In particular, the spatial correlation delineates a highly correlated fracture zones in the fold hinge area, implying a potentially fluid pathways through the rock mass (c.f. La Pointe 1993). The results clearly show that folding controls the spatial heterogeneity in the fracture network.

5.6.2 Future work

The present study suggests that the fracture orientations vary significantly across fault zones. The variograms can be used to measure the spatial heterogeneity and delineate the anisotropy of the secondary structures. As sampling is always restricted by the exposure conditions, it is inevitable that one is forced to use scattered data to estimate the values of inaccessible localities. A commonly used procedure of estimation is called kriging, in which a linear regression method is applied to estimate unsampled localities (Isaaks and Srivastava, 1989). If the form of the variogram is estimated by an appropriate model, kriging can be realized. Nowadays hydrocarbon exploration in the sub-surface could apply this methods to investigate the spatial correlation of fractures from borehole image logs, creating 2D estimation map of the spatial distribution of the fracture orientation. This has not been attempted in this study, but the application of variograms with significance testing using random resampling should represent a more robust first step in this workflow.

Laser-scanning is a novel technique used to collect the spatial data efficiently and accurately (Clegg et al., 2005). Thus far it has mainly been applied to capturing the 3D geometry of objects and to create virtual outcrops (e.g. McCaffrey et al. 2005; Trinks et al. 2005; Waggot et al. 2005). The spatial analysis applied in this study is an ideal tool to quantify the orientation data for fractures and faults captured using these new technologies.

For the analysis of noisy datasets, bootstrapping and associated techniques can robustly pull out 'hidden' information. Many datasets that are believed to be of poor quality may still have potential to provide useful information.

In terms of the lithology, the faults in the studied sandstones of high porosity may not have the similar characteristics to faults seen in low porosity rocks such as

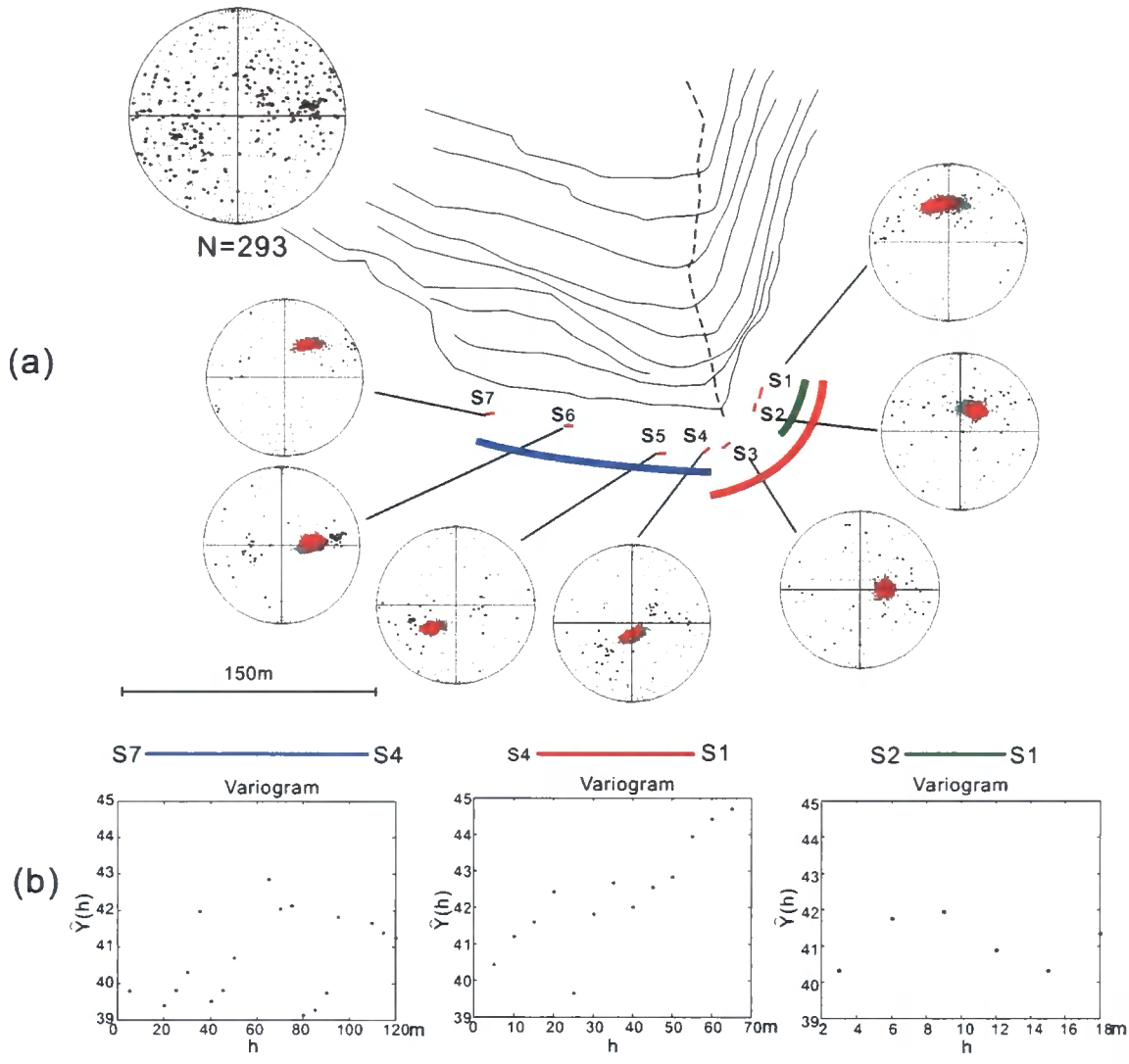

Figure 5.5: The spatial heterogeneity in the fracture orientations from a folded strata. (a) Orientation data at 7 localities moving on across the steep to the gentle limb show substantial variations. (b) Spatial correlation of the fracture orientation data from $S_1 - S_2$, $S_1 - S_4$, and $S_4 - S_7$, respectively.

mudstones, carbonates or crystalline rocks. The rotation and interlocking of reduced grains in high porosity sandstones during faulting will induce slip-hardening and create a damage zone where secondary faults or cataclasties accommodate most of the slip (Aydin and Johnson, 1983). For low porosity rocks, most of the slip can be accommodated by a major fault plane but a damage zone of cataclasties to the major fault is also common in many fault zones (e.g. Tarasewicz et al. 2005; Faulkner et al. 2006; Smith et al. 2008). Where is possible, the methodology developed in the

thesis may be applied in fault zones developed in low porosity lithologies.

5.7 Conclusions

The present investigation of the geometry and spatial heterogeneity of fracture orientations from three different tectonic settings has shown that the spatial heterogeneity and directional anisotropy of secondary fault patterns varies systematically towards the centre of fault zones. Seemingly diffuse conjugate fault patterns are, in many cases, an average-out representation of more complex fault polymodal or rotated fault patterns developed at different scales and/or at different localities relative to the master fault. These complexities can arise due to either the presence of pre-existing structures — especially when these are oblique to far-field tectonic transport directions and changes in lithology.

Appendix A

Innerproduct of vectors

The inner product of two vectors $\vec{V_1}$ and $\vec{V_2}$ in the Cartesian coordinate frame is expressed as:

$$\vec{V_1} \star \vec{V_2} = \|\vec{V_1}\| \cdot \|\vec{V_2}\| \cos\alpha \tag{A.1}$$

where α is the acute angle between $\vec{V_1}$ and $\vec{V_2}$. The equation A.1 suggests that if $\vec{V_1}$ is a unit vector, the inner product of $\vec{V_1}$ and $\vec{V_2}$ is the length $\|\vec{V_2}\|$ of $\vec{V_2}$ projected perpendicularly onto $\vec{V_1}$ (Fig. A.1).

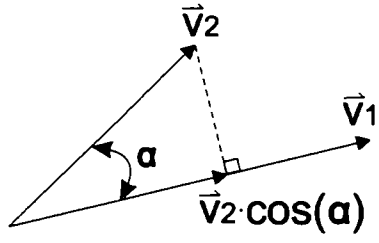

Figure A.1: The inner product of two vectors $\vec{V_1}$ and $\vec{V_2}$.

Appendix B

Type I error

In the standard statistical inference, the level of significance donated by α must be set before running the test. Given a distribution model of the test, if the value of the test is too large, it may fall into the critical region defined by α (Fig. B.1) and the null hypothesis will be rejected. The decision made is not always correct as the rejected null hypothesis may be true. The probability of rejecting the null

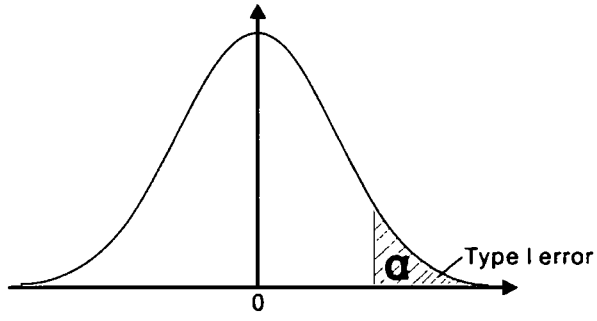

Figure B.1: Distribution of a statistical test with preset critical region specified for rejection of the hypothesis

hypothesis when it is actually true is called *type I error* which is equivalent to the level of significance. If we accept the null hypothesis for small test values, there is an unknown probability of making the wrong decision: the accepted null hypothesis is not true. The risk of committing such unknown error is called type II error. As such, we always tend to reject the null hypothesis with known type I error.

Appendix C

χ^2 distribution

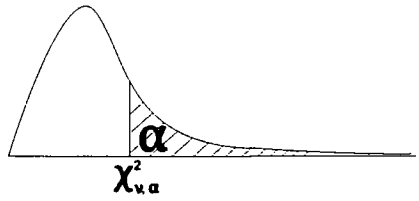

Table C.1: Preset type I error of $\chi^2_{\nu,\alpha}$ for ν degrees of freedom.

No. of degrees of Freedom, ν	Type I error, α				
	0.2	0.10	0.05	0.025	0.01
1	1.64	2.71	3.84	5.02	6.63
2	3.22	4.61	5.99	7.38	9.21
3	4.64	6.25	7.81	9.35	11.34
4	5.99	7.78	9.49	11.14	13.28
5	7.29	9.24	11.07	12.83	15.09
6	8.56	10.64	12.59	14.45	16.81
7	9.80	12.02	14.07	16.01	18.48
8	11.03	13.36	15.51	17.53	20.09
9	12.24	14.68	16.92	19.02	21.67
10	13.44	15.99	18.31	20.48	23.21

References

Adams, J. T., Dart, C., 1998. The appearance of potential sealing faults on borehole images. In: Jones, G., Fisher, Q. J., Knipe, R. J. (Eds.), Faulting, Fault Sealing and Fluid Flow in Hydrocarbon Reservoirs. Vol. 147. Geological Society, London, pp. 71–86.

Anderson, E. M., 1954. The dynamics of faulting and dyke formation with applications to Britain, 2nd Edition. Oliver and Boyd, [s.l.].

Angelier, J., 1979. Determination of the mean principal directions of stresses for a given fault population. Tectonophysics 56 (3-4), T17–T26.

Angelier, J., 1984. Tectonic analysis of fault slip data sets. Journal of Geophysical Research 89 (Nb7), 5835–5848.

Antonellini, M., Aydin, A., 1994. Effect of faulting on fluid-flow in porous sandstones - petrophysical properties. Aapg Bulletin-American Association of Petroleum Geologists 78 (3), 355–377.

Aydin, A., 1978. Small faults formed as deformation bands in sandstone. Pure and Applied Geophysics 116 (4-5), 913–930.

Aydin, A., 2000. Fractures, faults, and hydrocarbon entrapment, migration and flow. Marine and Petroleum Geology 17 (7), 797–814.

Aydin, A., Johnson, A. M., 1983. Analysis of faulting in porous sandstones. Journal of Structural Geology 5 (1), 19–31.

Aydin, A., Reches, Z., 1982. Number and orientation of fault sets in the field and in experiments. Geology 10 (2), 107–112.

Barton, C. A., Zoback, M. D., 1992. Self-similar distribution and properties of macroscopic fractures at depth in crystalline rock in the Cajon Pass Scientific Drill Hole. Journal of Geophysical Research-Solid Earth 97 (B4), 5181–5200.

Barton, C. C., 1995. Fractal analysis of scaling and spatial clustering of fractures. In: Barton, C. C., La Pointe, P. R. (Eds.), Fractals in the earth sciences. Plenum Press, New York, pp. 146–148.

Beacom, L. E., 1999. The kinematic evolution of reactivated and non-reactivated faults in basement rocks, NW Scotland. Ph.D. thesis, Queen's University of Belfast, 35-50.

Beacom, L. E., Holdsworth, R. E., McCaffrey, K., Andersen, T. B., 2001. A quantitative study of the influence of pre-existing compositional and fabric heterogeneities upon fracture-zone development during basement reactivation. In: Holdsworth, R. E., Strachan, R. A., Magloughlin, J. F., Knipe, R. J. (Eds.), The nature and tectonic significance of Fault zone weakening. Vol. 186. The Geological Society, London, pp. 195–211.

Bonnet, E., Bour, O., Odling, N. E., Davy, P., Main, I., Cowie, P., Berkowitz, B., 2001. Scaling of fracture systems in geological media. Reviews of Geophysics 39 (3), 347–383.

Bour, O., Davy, P., 1997. Connectivity of random fault networks following a power law fault length distribution. Water Resources Research 33 (7), 1567–1583.

Brewer, J. A., Smythe, D. K., 1984. Moist and the continuity of crustal reflector geometry along the Caledonian-Appalachian orogen. Journal of Geological Society, London 141, 150–120.

Caine, J. S., Evans, J. P., Forster, C. B., 1996. Fault zone architecture and permeability structure. Geology 24 (11), 1025–1028.

Caine, J. S., Forster, C. B., 1999. Fault zone architecture and fluid flow: insights from field data and numerical modeling. In: Haneberg, W. C., Mozley, P. S., Moore, J. C., Goodwin, L. B. (Eds.), Faults and subsurface fluid flow in the shallow crust, Geophysical monograph. Vol. 113. American Geophysical Union, Washington, DC, pp. 101–127.

Castaing, C., Halawani, M. A., Gervais, F., Chiles, J. P., Genter, A., Bourgine, B., Ouillon, G., Brosse, J. M., Martin, P., Genna, A., Janjou, D., 1996. Scaling relationships in intraplate fracture systems related to Red Sea rifting. Tectonophysics 261 (4), 291–314.

Chester, F. M., Evans, J. P., Biegel, R. L., 1993. Internal structure and weakening mechanisms of the San-Andreas Fault. Journal of Geophysical Research-Solid Earth 98 (B1), 771–786.

Clegg, P., Bruciatelli, L., Domingos, F., Jones, R. R., De Donatis, M., Wilson, R. W., 2006. Digital geological mapping with tablet PC and PDA: A comparison. Computers and Geosciences 32 (10), 1682–1698.

Clegg, P., Trinks, I., McCaffrey, K., Holdsworth, R., Jones, R., Hobbs, R., Waggott, S., 2005. Towards the Virtual Outcrop. Geoscientist 15 (1), 8–9.

Clifton, A. E., Kattenhorn, S. A., 2006. Structural architecture of a highly oblique divergent plate boundary segment. Tectonophysics 419 (1-4), 27–40.

Collier, R. E. L., 1989. Tectonic evolution of the Northumberland Basin - the effects of renewed extension upon an inverted extensional basin. Journal of the Geological Society, London 146, 981–989.

Corfu, F., Crane, A., Moser, D., Rogers, G., 1998. U-pb zircon systematics at gruinard bay, Northwest Scotland: implications for the early orogenic evolution of the Lewisian Complex. Contributions to Mineralogy and Petrology 133, 329–345.

Crampin, S., Mcgonigle, R., Bamford, D., 1980. Estimating crack parameters from observations of P-Wave velocity anisotropy. Geophysics 45 (3), 345–360.

Davis, F. B., 1977. Archaean evolution of the Lewisian Complex of Gruinard Bay. Scottish Journal of Geology 13, 189–196.

Davis, J. C., 2002. Statistics and data analysis in geology. John Wiley and Sons, pp. 11–594.

De Paola, N., Holdsworth, R. E., Mccaffrey, K. J. W., 2005a. The influence of lithology and pre-existing structures on reservoir-scale faulting patterns in transtensional rift zones. Journal of the Geological Society, London 162, 471–480.

De Paola, N., Holdsworth, R. E., McCaffrey, K. J. W., Barchi, M. R., 2005b. Partitioned transtension: an alternative to basin inversion models. Journal of Structural Geology 27 (4), 607–625.

Dershowitz, W., Herda, H., 1991. Interpretation of fracture spacing and intensity. In: Tillerson (Ed.), the 33rd U.S. Symposium on Rock Mechanics. Santa Fe, NM, USA, pp. 757–766.

Dewey, J. F., 2002. Transtension in arcs and orogens. International Geology Review 44 (5), 402–439.

Dewey, J. F., Hempton, M. R., Kidd, W., Saroglu, F., Sengor, A., 1986. Shorten of continental lithosphere: the neotectonics of eastern Anatolia—a young collision zone. In: Coward, M. P., Ries, A. C. (Eds.), Collision tectonics, Geological Society special publication. Published for the Geological Society by Blackwell Scientific, Oxford, pp. 3–36.

Dewey, J. F., Holdsworth, R. E., Strachan, R. A., 1998. Transpression and transtension zones. In: Holdsworth, R. E., Strachan, R. A., Dewey, J. F. (Eds.), Continental transpressional tectonics and transtensional tectonics, Geological Society special publication. Vol. 135. Geological Society, London, pp. 1–14.

Efron, B., 1982. The jackknife, the bootstrap and other resampling plans. In: Efron, B. (Ed.), Regional conferences series in applied mathematics. Philadelphia, Pennsylvania, pp. 27–36.

Eidelman, A., Reches, Z., 1992. Fractured pebbles - a new stress indicator. Geology 20 (4), 307–310.

Ellevset, S. O., Knipe, R. J., Olsen, T. S., Fisher, Q, J., Jones, G., 1998. Fault controlled communication in the Sleipner Vest Field, Norwegian Continental Shelf; detailed, quantitative input for reservoir simulation and well planning. In: Jones, G., Fisher, Q. J., Knipe, R. J. (Eds.), Faulting, Fault Sealing and Fluid Flow in Hydrocarbon Reservoirs, Geological Society special publication. Vol. 147. Geological Society, London, pp. 283–297.

Eshelby, J. D., 1957. The determination of the elastic field of an ellipsoidal inclusion, and related problems. Proceedings of the Royal Society of London Series a-Mathematical and Physical Sciences 241 (1226), 376–396.

Faulkner, D. R., Mitchell, T. M., Healy, D., Heap, M. J., 2006. Slip on 'weak' faults by the rotation of regional stress in the fracture damage zone. Nature 444 (7121), 922–925.

Faulkner, D. R., Mitchell, T. M., Rutter, E. H., Cembrano, J., 2008. On the structure and mechanical properties of large strike-slip faults. In: Wibberley, C. A. J., Kurz, W., Imber, J., Holdsworth, R. E., Collettini, C. (Eds.), The internal structure of fault zones. Vol. 299. Geological Society, London, pp. 139–150.

Fisher, N. I., Lewis, T., Embleton, B. J. J., 1987. Statistical analysis of spherical data. Cambridge University Press, Cambridge, 198-208.

Flinn, D., 1962. On folding during three dimensional progressive deformation. Quarterly Journal of Geological Society, London 118, 385–428.

Fossen, H., Schultz, R. A., Shipton, Z. K., Mair, K., 2007. Deformation bands in sandstone: a review. Journal of the Geological Society, London 164, 755–769.

Fossen, H., Tikoff, B., 1993. The deformation matrix for simultaneous simple shearing, pure shearing and volume change, and its application to transpression transtension tectonics. Journal of Structural Geology 15 (3-5), 413–422.

Gay, N. C., Fripp, R. E. P., 1976. Control of ductility on deformation of pebbles and conglomerates. Philosophical Transactions of the Royal Society of London Series a-Mathematical Physical and Engineering Sciences 283 (1312), 109–128.

Gillespie, P. A., Howard, C. B., Walsh, J. J., Watterson, J., 1993. Measurement and characterization of spatial distributions of fractures. Tectonophysics 226 (1-4), 113–141.

Gross, M. R., 1995. Fracture partitioning - failure mode as a function of lithology in the Monterey Formation of Coastal California. Geological Society of America Bulletin 107 (7), 779–792.

Guion, P. D., Gutteridge, P., Davis, S. J., 2000. Carboniferous sedimentation and volcanism on the Laurussian margin. In: Woodcock, N. H., Strachan, R. A. (Eds.), Geological history of Britain and Ireland. Blackwell Science, Oxford, pp. 227–270.

Gupta, A. K., Adler, P. M., 2006. Stereological analysis of fracture networks along cylindrical galleries. Mathematical Geology 38 (3), 233–267.

Hafner, W., 1951. Stress distributions and faulting. Geological Society of America Bulletin 62 (4), 373–398.

Hardebeck, J. L., Hauksson, E., 1999. Role of fluids in faulting inferred from stress field signatures. Science 285 (5425), 236–239.

Harland, W. B., 1971. Tectonic transpression in Caledonian Spitsbergen. Geological Magazine 108 (1), 27–42.

Healy, D., Jones, R. R., Holdsworth, R. E., 2006a. New insights into the development of brittle shear fractures from a 3D numerical model of microcrack interaction. Earth and Planetary Science Letters 249 (1-2), 14–28.

Healy, D., Jones, R. R., Holdsworth, R. E., 2006b. Three-dimensional brittle shear fracturing by tensile crack interaction. Nature 439 (7072), 64–67.

Heffer, K. J., Bevan, T. G., 1990. Scaling relationships in natural fracture-data, theory and applications. Society Petroleum Engineers 20981.

Hesthammer, J., Johansen, T. E. S., Watts, L., 2000. Spatial relationships within fault damage zones in sandstone. Marine and Petroleum Geology 17 (8), 873–893.

Hobbs, B. E., Means, W. D., Williams, P. F., 1976. Analysis of areas with complex structure. In: Hobbs, B. E., Means, W. D., Williams, P. F. (Eds.), An outline of structural geology. Wiley, New York, pp. 364–375.

Holdsworth, R. E., Butler, C. A., Roberts, A. M., 1997. The recognition of reactivation during continental deformation. Journal of the Geological Society, London 154, 73–78.

Holdsworth, R. E., Tavarnelli, E., Clegg, P., Pinheiro, R. V. L., Jones, R. R., McCaffrey, K. J. W., 2002. Domainal deformation patterns and strain partitioning during transpression: An example from the Southern Uplands terrane, Scotland. Journal of the Geological Society, London 159, 401–415.

Huseby, O., Thovert, J. F., Adler, P. M., 1997. Geometry and topology of fracture systems. Journal of Physics a-Mathematical and General 30 (5), 1415–1444.

Isaaks, E. H., Srivastava, R. M., 1989. Applied geostatistics. Oxford University Press, New York, pp. 46–49;140–183.

Johansen, T. E. S., Fossen, H., 2008. Internal geometry of fault damage zones in interbedded siliciclastic sediments. In: Wibberley, C. A. J., Kurz, W., Imber, J., Holdsworth, R. E., Collettini, C. (Eds.), The internal structure of fault zones. Vol. 299. Geological Society, London, pp. 35–56.

Johnston, J. D., McCaffrey, K. J. W., 1996. Fractal geometries of vein systems and the variation of scaling relationships with mechanism. Journal of Structural Geology 18 (2-3), 349–358.

Johnstone, G. S., Mykura, W., 1989. Mesozoic: New Red Sandstone; Jurassic; Cretaceous. In: Johnstone, G. S., Mykura, W. (Eds.), British regional geology : the Northern Highlands of Scotland, 4th Edition. H.M.S.O., London, pp. 145–162.

Jones, R. R., Holdsworth, R. E., Bailey, W., 1997. Lateral extrusion in transpression zones: the importance of boundary conditions. Journal of Structural Geology 19 (9), 1201–1217.

Jones, R. R., Holdsworth, R. E., Clegg, P., McCaffrey, K., Tavarnelli, E., 2004. Inclined transpression. Journal of Structural Geology 26 (8), 1531–1548.

Jones, R. R., Holdsworth, R. E., McCaffrey, K. J. W., Clegg, P., Tavarnelli, E., 2005. Scale dependence, strain compatibility and heterogeneity of three-dimensional deformation during mountain building: a discussion. Journal of Structural Geology 27 (7), 1190–1204.

Jones, R. R., Tanner, P. W. G., 1995. Strain partitioning in transpression zones. Journal of Structural Geology 17 (6), 793–802.

Kemp, E. A., Schetselaar, E. M., Sprague, K., 2006. 3-d symbolization of L-S fabrics as an aid to the analysis of geological structures. Computer and Geosciences 32 (1), 52–63.

Kim, Y. S., Peacock, D. C. P., Sanderson, D. J., 2004. Fault damage zones. Journal of Structural Geology 26 (3), 503–517.

Kimbell, G. S., Chadwick, R. A., Holliday, D. W., Werngren, O. C., 1989. The structure and evolution of the Northumberland Trough from new seismic-reflection data and its bearing on modes of continental extension. Journal of the Geological Society, London 146, 775–787.

Knipe, R. J., Jones, G., Fisher, Q. J., 1998. Faulting, fault sealing and fluid flow in hydrocarbon reservoirs: an introduction. In: Jones, G., Fisher, Q. J., Knipe, R. J. (Eds.), Faulting, Fault Sealing and Fluid Flow in Hydrocarbon Reservoirs. Vol. 147. Geological Society, London, pp. vii–xxi.

Knott, S. D., 1994. Fault zone thickness versus displacement in the Permo-Triassic sandstones of NW england. Journal of the Geological Society, London 151 (1), 17–25.

Knott, S. D., Beach, A., Brockbank, P. J., Brown, J. L., McCallum, J. E., Welbon, A. I., 1996. Spatial and mechanical controls on normal fault populations. Journal of Structural Geology 18 (2-3), 359–372.

La Pointe, P. R., 1993. Pattern analysis and simulation of joints for rock engineering. In: Judson, J. A. (Ed.), Comphrensive rock engineering: rock testing and site characterization. Vol. 3. pp. 215–239.

Laubach, S. E., Olson, J. E., Gale, J. F. W., 2004. Are open fractures necessarily aligned with maximum horizontal stress? Earth and Planetary Science Letters 222 (1), 191–195.

Leeder, M. R., Fairhead, D., Lee, A., Stuart, G., Clemmey, H., Green, B., Alhadden, B., 1989. Sedimentary and tectonic evolution of the Northumberland Basin. Proceedings of the Yorkshire Geological Society 47, 207–233.

Lewis, J. C., 2007. Fine-scale partitioning of contemporary strain in the southern Walker Lane: Implications for accommodating divergent strike-slip motion. Journal of Structural Geology 29 (7), 1201–1215.

Lin, S., Jiang, D., Williams, P. F., 1998. Transpression (or transtension) zones of triclinic symmetry: natural example and theoretical modelling. In: Holdsworth, R. E., Strachan, R. A., Dewey, J. F. (Eds.), Continental transpressional tectonics and transtensional tectonics. Vol. 135. Geological Society, London, pp. 41–57.

Lisle, R. J., Leyshon, P. R., 2004. Stereographic projection techniques in structural geology, 2nd Edition. Cambridge University Press, Cambridge.

Lovell, J. P. B., 1991. Permain and Triassic. In: Craig, G. Y. (Ed.), Geology of Scotland, 3rd Edition. Geological Society, London, pp. 421–438.

Maillot, B., Cowie, P., Lague, D., 1998. Simulating polyphase faulting with a tensorial 3D model of fault growth. In: Jones, G., Fisher, Q. J., Knipe, R. J. (Eds.), Faulting, Fault Sealing and Fluid Flow in Hydrocarbon Reservoirs. Vol. 147. Geological Society, London, pp. 209–216.

Mandal, N., Chakraborty, C., Samanta, S. K., 2001. Controls on the failure mode of brittle inclusions hosted in a ductile matrix. Journal of Structural Geology 23 (1), 51–66.

Mandelbrot, B. B., 1982. The fractal geometry of nature. W.H. Freeman, San Francisco, 1-460.

Manzocchi, T., Walsh, J. J., Nell, P., Yielding, G., 1999. Fault transmissibility multipliers for flow simulation medels. Petroleum Geoscience 5, 53–63.

Mardia, K. V., Jupp, P. E., 2000. Directional statistics. John Wiley and Sons Ltd, Chichester, pp. 159–167.

Mardia, K. V., Kent, J. T., Bibby, J. M., 1979. Multivariate analysis. Academic Press, London, pp. 333–359.

Matthai, S. K., Aydin, A., Pollard, D. D., Roberts, S. G., 1998. Numerical simulation of departures from radial drawdown in a faulted sandstone reservoir with joints and deformation bands. In: Jones, G., Fisher, Q. J., Knipe, R. J. (Eds.), Faulting, Fault Sealing and Fluid Flow in Hydrocarbon Reservoirs, Geological Society special publication. Vol. 147. Geological Society, London, pp. 157–192.

Mauldon, M., Dunne, W. M., Rohrbaugh, M. B., 2001. Circular scanlines and circular windows: new tools for characterizing the geometry of fracture traces. Journal of Structural Geology 23 (2-3), 247–258.

McCaffrey, K. J. W., Jones, R. R., Holdsworth, R. E., Wilson, R. W., Clegg, P., Imber, J., Hollman, N., Trinks, I., 2005. Unlocking the spatial dimension: digital technologies and the future of geoscience fieldwork. Journal of the Geological Society, London 162, 927–938.

McCoss, A. M., 1986. Simple constructions for deformation in transpression transtension zones. Journal of Structural Geology 8 (6), 715–718.

McEwen, T. J., 1981. Brittle deformation in pitted pebble conglomerates. Journal of Structural Geology 3 (1), 25–37.

Michael, A. J., 1984. Determination of stress from slip data - faults and folds. Journal of Geophysical Research 89 (Nb13), 1517–1526.

Middleton, G. V., 2000. Data analysis in the earth science using MATLAB. Prentice Hall; Prentice-Hall International (UK), London.

Molnar, P., 1992. Brace-Goetze strength-profiles, the partitioning of strike-slip and thrust faulting at zones of oblique convergence, and the stress-heat flow paradox of the San Andreas Fault. In: Evans, B., Wong, T.-f. (Eds.), Fault mechanics

and transport properties in rocks: a Festschrift in honor of W.F. Brace. Academic Press, London, pp. 435–459.

Odling, N. E., Gillespie, P., Bourgine, B., Castaing, C., Chiles, J. P., Christensen, N. P., Fillion, E., Genter, A., Olsen, C., Thrane, L., Trice, R., Aarseth, E., Walsh, J. J., Watterson, J., 1999. Variations in fracture system geometry and their implications for fluid flow in fractured hydrocarbon reservoirs. Petroleum Geoscience 5 (4), 373–384.

Ortega, O. J., Marrett, R. A., Laubach, S. E., 2006. A scale-independent approach to fracture intensity and average spacing measurement. Aapg Bulletin 90 (2), 193–208.

Ouillon, G., Castaing, C., Sornette, D., 1996. Hierarchical geometry of faulting. Journal of Geophysical Research-Solid Earth 101 (B3), 5477–5487.

Park, R. G., Stewart, A. D., Wright, D. T., 2002. The Hebridean terrane. In: Trewin, N. H. (Ed.), The Geology of Scotland. The Geological Society, London, pp. 45–80.

Peacock, D. C. P., 1991. Displacements and segment linkage in strike-slip-fault zones. Journal of Structural Geology 13 (9), 1025–1035.

Philip, Z. G., Jennings Jr., J. W., Olson, J. E., Laubach, S. E., Holder, J., 2005. Modelling coupled fracture-matrix fluid flow in geomechanically simulated fracture networks. SPE Reservoir Evaluation & Engineering 8, 300–309.

Putz-Perrier, M., Sanderson, D., 2008. Spatial distribution of brittle strain in layered sequences. Journal of Structura Geology 30, 50–64.

Ramsay, J., 1967. Folding and fracturing of rocks. McGraw Hill, New York.

Ramsay, J. G., Huber, M. I., 1987. The techniques of modern structural geology, Vol. 2, Folds and fractures. Academic Press, London.

Reches, Z., 1978. Analysis of faulting in 3-dimensional strain field. Tectonophysics 47 (1-2), 109–129.

Reches, Z., 1983. Faulting of rocks in 3-dimensional strain fields 2. Theoretical-analysis. Tectonophysics 95 (1-2), 133–156.

Reches, Z., Baer, G., Hatzor, Y., 1992. Constraints on the strength of the upper crust from stress inversion of fault slip data. Journal of Geophysical Research-Solid Earth 97 (B9), 12481–12493.

Reches, Z., Dieterich, J. H., 1983. Faulting of rocks in 3-dimensional strain fields 1. Failure of rocks in polyaxial, servo-control experiments. Tectonophysics 95 (1-2), 111–132.

Roberts, A. M., Holdsworth, R. E., 1999. Linking onshore and offshore structures: Mesozoic extension in the Scottish Highlands. Journal of the Geological Society, London 156, 1061–1064.

Sanderson, D. J., Marchini, W. R. D., 1984. Transpression. Journal of Structural Geology 6 (5), 449–457.

Schopfer, M. P. J., Childs, C., Walsh, J. J., 2006. Localisation of normal faults in multilayer sequences. Journal of Structural Geology 28 (5), 816–833.

Schulz, S. E., Evans, J. P., 1998. Spatial variability in microscopic deformation and composition of the Punchbowl Fault, southern California: implications for mechanisms, fluid-rock interaction, and fault morphology. Tectonophysics 295 (1-2), 223–244.

Shipton, Z. K., Cowie, P. A., 2001. Damage zone and slip-surface evolution over mu m to km scales in high-porosity Navajo sandstone, Utah. Journal of Structural Geology 23 (12), 1825–1844.

Shipton, Z. K., Cowie, P. A., 2003. A conceptual model for the origin of fault damage zone structures in high-porosity sandstone. Journal of structural geology 25 (3), 333–344.

Sibson, R. H., 2000. Fluid involvement in normal faulting. Journal of Geodynamics 29 (3-5), 469–499.

Sigda, J. M., Goodwin, L. B., Mozley, P. S., Wilson, J. L., 1999. Permeability alteration in small-displacement in poorly lithified sediments: Rio grande rift, central new mexico. In: Haneberg, W. C., Mozley, P. S., Moore, J. C., Goodwin, L. B. (Eds.), Faults and subsurface fluid flow in the shallow crust, Geophysical monograph. Vol. 113. American Geophysical Union, Washington, DC, pp. 51–68.

Smith, J. V., Durney, D. W., 1992. Experimental formation of brittle structural assemblages in oblique divergence. Tectonophysics 216 (3-4), 235–253.

Smith, S. A. F., Collettini, C., Holdsworth, R. E., 2008. Recognizing the seismic cycle along ancient faults: CO2-induced fluidization of breccias in the footwall of a sealing low-angle normal fault. Journal of Structural Geology 30 (8), 1034–1046.

Stein, A. M., 1988. Basement controls upon basin development in the Caledonian foreland, NW scotland. Basin Research 1, 107–119.

Stewart, A. D., 1982. Late Proterozoic Rifting in NW scotland - the Genesis of the 'Torridonian'. Journal of the Geological Society, London 139 (Jul), 413–420.

Stewart, A. D., 1991. Torridonian. In: Craig, G. Y. (Ed.), The Geology of Scotland, 3rd Edition. Geological Society, London, pp. 65–85.

Stewart, A. D., 1993. Late Proterozoic and Late Paleozoic Movement on the Coigach Fault in NW-Scotland. Scottish Journal of Geology 29, 21–28.

Tarasewicz, J. P. T., Woodcock, N. H., Dickson, J. A. D., 2005. Carbonate dilation breccias: Examples from the damage zone to the Dent Fault, northwest england. GSA Bulletion 117 (5/6), 736–745.

Taylor, T. R., Dewey, J. F., Monastero, F. C., 2008. Transtensional deformation of the brittle crust: Field observations and theoretical applications in the Coso-China lake region, Eastern margin of the Sierra Nevada microplate, southeastern California. International Geology Review 50 (3), 218–244.

Tikoff, B., Teyssier, C., 1994. Strain modeling of displacement-field partitioning in transpressional orogens. Journal of Structural Geology 16 (11), 1575–1588.

Tikoff, B., Wojtal, S. F., 1999. Displacement control of geologic structures. Journal of Structural Geology 21 (8-9), 959–967.

Tran, N. H., 2007. Fracture orientation characterization: Minimizing statistical modelling errors. Computational Statistics and Data Analysis 51 (6), 3187–3196.

Trinks, I., Clegg, P., McCaffrey, K., Jones, R. R., Hobbs, R., Holdsworth, R. E., Holliman, N., Imber, J., Waggott, S., Wilson, R. W., 2005. Mapping and analyzing virtual outcrops. Visual Geosciences 10, 1319.

Tron, V., Brun, J. P., 1991. Experiments on oblique rifting in brittle ductile systems. Tectonophysics 188 (1-2), 71–84.

Tucker, M., 2001. Sedimetary Petrology. Blackwell Scientific Publications, pp. 53–55.

Twiss, R. J., Moores, E. M., 2007. Structural geology. W. H. Freeman, New York.

Underhill, J. R., Woodcock, N. H., 1987. Faulting mechanisms in high-porosity sandstones; New Red Sandstone, Arran, Scotland. In: Jones, M. E., Preston, R. M. F. (Eds.), Deformation of Sediments and Sedimentary Rocks. Vol. 29. Geological Society Special Publication, London, pp. 91–105.

Van-der Zee, W., Wibberley, C. A. J., Urai, J. L., 2008. The influence of layering and pre-existing joints on the development of internal structure in normal fault zones: the lodeve basin, france. In: Wibberley, C. A. J., Kurz, W., Imber, J., Holdsworth, R. E., Collettini, C. (Eds.), The internal structure of fault zones. Vol. 299. Geological Society, London, pp. 57–74.

Vermilye, J. M., Scholz, C. H., 1998. The process zone: A microstructural view of fault growth. Journal of Geophysical Research 103, 12223–12237.

Versey, H. C., 1938. The petrography of the permian rocks in the southern part of the Vale of Eden. Quarterly Journal of the Geological Society, London xcv, 275–298.

Waggot, S., Clegg, P., Jones, R., 2005. Combining terrestrial laser scanning, RTK GPS and 3D visualization: application of optical 3D measurement in geological exploration. In: Proceedings of the 7th Conference on 3-D Optical Measurement Techniques.

Watson, G. S., 1983. Statistical methods based on the center of mass of the sample. In: Watson, G. S. (Ed.), Statistics on Shperes. John Wiley & Sons, New York, pp. 135–165.

Wilson, J. E., Chester, J. S., Chester, F. M., 2003. Microfracture analysis of fault growth and wear processes, Punchbowl fault, San Andreas System, California. Journal of Structural Geology 25 (11), 1855–1873.

Wilson, R. W., McCaffrey, K. J. W., Holdsworth, R. E., Imber, J., Jones, R. R., Welbon, A. I. F., Roberts, D., 2006. Complex fault patterns, transtension and structural segmentation of the Lofoten Ridge, Norwegian margin: Using digital mapping to link onshore and offshore geology. Tectonics 25 (4), TC4018.

Withjack, M. O., Jamison, W. R., 1986. Deformation produced by oblique rifting. Tectonophysics 126 (2-4), 99–124.

Wojtal, S., 1989. Measuring displacement gradients and strains in faulted rocks. Journal of Structural Geology 11 (6), 669–678.

Woodcock, N. H., Naylor, M. A., 1983. Randomness testing in 3-dimensional orientation data. Journal of Structural Geology 5 (5), 539–548.

Ye, S., Rabiller, P., 2000. A new tool for electro-facies analysis: multi-resolution graph-based clustering. In: SPWLA 41st Annual Logging Symposium.

Yielding, G., Needham, T., Jones, H., 1996. Sampling of fault populations using sub-surface data: A review. Journal of Structural Geology 18 (2-3), 135–146.

Zadeh, L. A., 1979. Fuzzy sets and information granularity. In: Gupta, M., Ragade, R., Yager, R. (Eds.), Advances in Fuzzy Set Theory and Applications. North-Holland Publishing Co., Amsterdam, pp. 3–18.